
A Dynamical Mass Map of the Fornax Cluster

Avinash Chaturvedi



München 2023

A Dynamical Mass Map of the Fornax Cluster

Dissertation

an der Fakultät für Physik
der Ludwig-Maximilians-Universität
München

vorgelegt von

Avinash Chaturvedi

geboren in Varanasi, Indien

München, den 02.02.2023

Erstgutachter: Prof. Dr. Andreas Burkert

Zweitgutachter: Prof. Dr. Daniel Gruen

ESO Betreuer: Dr. Michael Hilker

Tag der mündlichen Prüfung: 9 March, 2023

Zusammenfassung

Galaxienhaufen sind die größten gravitativ gebundenen Objekte im Universum. Sie bieten die Möglichkeit, die Verteilung der baryonischen und dunklen Materie auf einer großen physikalischen Skala zu untersuchen. Der Fornax-Galaxienhaufen ist einer der nächsten und dichtesten Galaxienhaufen. Frühere photometrische Untersuchungen des Fornax-Galaxienhaufens haben das Vorhandensein stellarer und zeitenbedingter Strukturen im Kern und in den Intra-Cluster-Regionen gezeigt. Untersuchungen der Kugelsternhaufenpopulationen (GCs) in Fornax haben eine Überdichte von GCs aufgewiesen, die mehrere zentrale Haufengalaxien miteinander verbindet. GCs sind helle und kompakte Quellen, die als diskrete kinematische Tracer verwendet werden können, um die stellare Population und die Massenverteilung in den Außenbezirken der Galaxien zu untersuchen, wo die Feldsterne zu schwach sind, um direkt beobachtet zu werden. Ziel dieser Arbeit ist es, den Massenaufbau des Fornax-Galaxienhaufens mit Hilfe seiner GC-Systeme zu untersuchen.

Das Verständnis des Ursprungs und des kinematischen Verhaltens der GCs innerhalb von Fornax ist entscheidend, um den Massenaufbau des Galaxienhaufens zu verstehen. Arbeiten zur dynamischen Massenmodellierung von Galaxienhaufen haben gezeigt, dass die Vernachlässigung von Substrukturen, die durch Akkretions- und Fusionsereignisse entstehen, Auswirkungen auf die Massenschätzung von Haufen haben kann. Der Fornax-Haufen bietet eine hervorragende Gelegenheit, die Rolle der Substrukturen bei der Massenmodellierung zu untersuchen. In dieser Arbeit habe ich die spektroskopischen Daten des Visible Multi-Object Spectrograph am Very Large Telescope (VLT/VIMOS) aus der spektroskopischen Durchmusterung des Fornax-Haufens am VLT (FVSS) verwendet, die einen Quadratgrad um die zentrale massereiche Galaxie NGC 1399 abdeckt.

Ich habe VIMOS-FVSS-Daten zur kinematischen Charakterisierung der photometrisch entdeckten GC Kandidaten verwendet. Mit einer sorgfältigen Analyse dieser Daten detektiere ich insgesamt 777 GCs, was fast einer Verdoppelung der bereits entdeckten GCs entspricht, wobei ich denselben Datensatz wie zuvor verwendet habe. In Kombination mit früheren Radialgeschwindigkeitsmessungen von GCs in Fornax aus der Literatur stelle ich die umfangreichste spektroskopische GC-Stichprobe von 2341 Objekten in dieser Umgebung zusammen. Ich habe herausgefunden, dass rote (metallreiche) GCs meist um Hauptgalaxien herum konzentriert sind, während blaue (metallarme) GCs kinematisch unregelmäßig sind und weit über die Kernregion des Haufens verteilt sind. Ich finde Belege dafür, dass die Substrukturen von Fornax und die Regionen innerhalb des Haufens hauptsächlich von blauen GCs dominiert werden.

Um die baryonische und dunkle Materie der zentralen Galaxie des Fornax-Haufens, NGC 1399, zu verstehen, habe ich die kompilierten Radialgeschwindigkeiten der GCs verwendet, um die Massenmodellierung von NGC 1399 bis zu fünf effektiven Radien durchzuführen. Unter Verwendung der sphärischen Jeans-Modellierung habe ich die Dispersions-Kurtosis-Technik angewandt, um das Massenprofil von NGC 1399 und die orbitale Anisotropie der GCs zu erhalten. Unabhängig von den DM-Haloprofilen, die für die Modellierung verwendet werden, stelle ich fest, dass die Intra-Cluster-GCs eine leichte radiale Anisotropie aufweisen, insbesondere bei blauen, metallarmen GCs.

Außerdem habe ich das Intra-Cluster-Medium (ICM) von Fornax-ähnlichen Halos aus theoretischer Sicht untersucht. Ich nutze die kosmologische Simulation TNG50 in Synergie mit einer laufenden MeerKAT-Radiodurchmusterung des Fornax-Haufens (MFS), um die Verteilung von kaltem Gas im ICM Fornax-ähnlicher Haufen zu verstehen. Unter Anwendung derselben Beobach-

tungskriterien wie die MFS stelle ich fest, dass TNG50-Halos bei $z \sim 0$ eine große Menge an HI-Gas innerhalb des Haufens aufweisen. Ich sage voraus, dass die MFS eine HI Verteilung beobachten wird, der einen Flächenanteil von 10% bei einem Virialradius und bis zu 5% für den Intra-Cluster-HI abdeckt.

Im Rahmen dieser Arbeit habe ich den Massenaufbau des Fornax-Haufens untersucht und etwas über sein IC-Medium gelernt. Die Ergebnisse dieser Arbeit veranschaulichen die Bedeutung der GCs für das Verständnis der Entstehungsgeschichte des Fornax-Haufens und legen die Grundlage dafür, dass Intra-Cluster GCs bei der Massenmodellierung unbedingt berücksichtigt werden müssen. Darüber hinaus bietet die Voraussage einer großen Menge kalten Gases in den Fornax-ähnlichen Halos in den TNG50 Simulationen ein spannendes Szenario, das mit zukünftigen Ergebnissen aus der MFS getestet werden kann.

Abstract

Galaxy clusters are the largest gravitationally bound objects in the Universe. They provide the opportunity to explore the baryonic and dark matter distribution on a large physical scale. The Fornax galaxy cluster is one of the densest galaxy clusters in the nearby Universe. Previous photometric studies of Fornax have revealed the presence of stellar and tidal streams within the core and intra-cluster regions. Studies of globular clusters (GC) populations in Fornax have shown an overdensity of GCs connecting several central cluster galaxies. GCs are bright and compact sources that can be used as discrete kinematic tracers to study the stellar population and mass distribution of the galaxies' outskirts, where field stars are too faint to be directly observed. The goal of this thesis is to explore the mass assembly of the Fornax galaxy cluster using its GC systems.

A crucial piece of information to understand the mass assembly of the Fornax cluster is to comprehend the origin and kinematic behaviour of the intra-cluster GCs. Dynamical mass-modelling of galaxy clusters has shown that ignoring the presence of substructures which are generated by accretion and merger events could impact the mass estimates of clusters. The Fornax cluster provides an excellent opportunity to explore the role of substructures in mass-modelling. In this thesis, I have used the spectroscopic data from the Visible Multi-Object Spectrograph at Very Large Telescope (VLT/VIMOS) from the Fornax cluster VLT spectroscopic survey (FVSS), covering one square degree around the central massive galaxy NGC 1399.

I used VIMOS-FVSS data to kinematically characterize the photometrically discovered GC candidates. With a careful analysis of this data, I confirm a total of 777 GCs, almost doubling previously detected GCs, using the same dataset as was used before. Combined with previous literature radial velocity measurements of GCs in Fornax, I compile the most extensive spectroscopic GC sample of 2341 objects in this environment. I found that red (metal-rich) GCs are mostly concentrated around major galaxies, while blue (metal-poor) GCs are kinematically irregular and are widely spread throughout the core region of the cluster. I find evidence that Fornax substructures and intra-cluster regions are dominated mostly by blue GCs.

To understand the baryonic and dark matter of the central galaxy of the Fornax cluster, NGC 1399, I used the compiled GCs radial velocities to perform the mass-modelling of NGC 1399 out to 5 effective radii. Using spherical Jeans modelling, I applied the dispersion-kurtosis technique to obtain the mass profile of NGC 1399 and the orbital anisotropy of GCs. I find that both cusp (NFW) and core (Burkert) halos can produce the observed kinematics. Independent of the DM halo profiles used in modelling, I find that intra-cluster GCs have mild radial anisotropy, especially for blue, metal-poor GCs.

Lastly, I studied the intra-cluster medium (ICM) of Fornax-like halos from a theoretical point of view. I utilize the TNG50 cosmological simulation in synergy with an ongoing MeerKAT radio survey of the Fornax cluster (MFS) to understand the distribution of cold gas in the ICM of Fornax-like clusters. I find that TNG50 halos at $z \sim 0$, have an abundant amount of intra-cluster HI gas. I predict that MFS will observe an HI covering fraction of 10% at one virial radius and up to 5% for the intra-cluster HI.

In summary, I have studied the mass assembly of the Fornax cluster and learned about its IC medium. The results from this thesis illustrate the importance of GCs in understanding the assembly

history of the Fornax cluster and lays the foundation for future, more detailed mass-modelling work of intra-cluster GCs. In addition, the prediction of a large amount of cold gas in Fornax-like halos in the TNG50 simulations provides an exciting scenario to be tested with future results from the MFS.

*To my teachers, family, friends
and
in loving memory of my father*

Contents

Acronyms	V
List of Figures	VII
List of Tables	XI
1. Introduction	1
1.1. Λ CDM in nutshell	2
1.1.1. Structure formation in the Λ CDM framework	3
1.1.2. Formation and evolution of galaxies	4
1.2. Galaxy clusters	5
1.2.1. Observational imprints of the hierarchical growth	7
1.2.2. Mass-modelling	8
1.2.3. Jeans Modelling	9
1.2.4. Role of cluster environment in galaxy evolution	10
1.2.5. Circum-galactic medium	11
1.3. Importance of nearby galaxy clusters	12
1.3.1. Role of substructures	12
1.3.2. Intra-cluster medium of nearby galaxy clusters	13
1.3.3. Globular Clusters as tracers of galaxy mass-assembly	14
1.3.4. Atomic hydrogen as tracer of the cluster environment	15
1.4. Fornax galaxy cluster	16
1.4.1. GCs system of the Fornax cluster	17
1.4.2. Mass-modelling of the Fornax cluster	18
1.4.3. ICM of Fornax cluster-like halo in cosmological simulations	20
1.5. Motivation behind this thesis	20
1.6. This thesis	20
2. Kinematical characterisation of globular clusters in the Fornax galaxy cluster	23
2.1. Introduction	23
2.2. Observations and data reduction	24
2.2.1. Photometry and globular cluster selection	25
2.2.2. Observations	25
2.2.3. Data reduction	25

2.3.	Analysis	27
2.3.1.	Radial velocity measurements	27
2.3.2.	Selecting Fornax cluster members	31
2.4.	Results	32
2.4.1.	Duplicate measurements	33
2.4.2.	Comparison with previous measurements	33
2.4.3.	Photometric properties	35
2.4.4.	Radial velocity map	37
2.5.	Discussion	39
2.5.1.	Colours, phase space, and spatial distribution	39
2.5.2.	Velocity dispersion profile	40
2.5.3.	Globular clusters and planetary nebulae	44
2.5.4.	Intracluster GC kinematics	45
2.6.	Conclusions	52
3.	Mass-modelling of the BCG NGC 1399	55
3.1.	Introduction	55
3.2.	Data	57
3.2.1.	GCs sample for dynamical modelling	57
3.2.2.	Globular clusters (GCs) surface density	60
3.2.3.	GCs kinematics	61
3.2.4.	GCs rotation	64
3.3.	Dynamical modelling	65
3.3.1.	Jeans modelling	65
3.3.2.	Gravitational potential	66
3.3.3.	Maximum likelihood analysis	67
3.4.	Results	68
3.4.1.	Fit to the kinematic data	70
3.5.	Discussion	73
3.5.1.	Mass profile	73
3.5.2.	Comparison with simulation studies	77
3.5.3.	GCs orbital distribution	78
3.6.	Summary and Conclusions	80
4.	Distribution of atomic hydrogen in TNG50 Fornax-like galaxy clusters	81
4.1.	Introduction	81
4.2.	Simulation and Methodology	83
4.2.1.	The TNG simulations	83
4.2.2.	Fornax-like Halo selection	84
4.2.3.	Atomic HI content	84
4.2.4.	HI column density	85
4.2.5.	Halo HI covering fraction	86
4.3.	Results	86
4.3.1.	HI covering fraction profiles	90

4.3.2.	Intra-cluster HI covering fraction	91
4.3.3.	HI covering fraction in velocity space	92
4.4.	Discussion	92
4.4.1.	Comparison to other cosmological simulations	92
4.4.2.	Detection of HI clouds in the Intra-cluster region through observational work	94
4.4.3.	Possible Origin Scenario	95
4.5.	Summary and Conclusion	95
5.	Summary and conclusions	97
6.	Outlook	101
6.1.	Substructures in nearby galaxy clusters	102
6.2.	Dynamical mass-modeling to infer the luminous and DM distributions	103
6.3.	Role of cluster environment on galaxy evolution	103
A.	Appendix of Chapter 2	105
A.1.	Test regarding pPXF parameter choices	105
A.2.	Example of a GC portfolio	108
A.3.	Catalogue of VIMOS dataset GCs	109
	References	111
	Acknowledgments	121

Acronyms

Λ CDM	Λ Cold Dark Matter.
ACSFCS	ACS Fornax Cluster Survey.
ACSVCS	ACS Virgo Cluster Survey.
CBE	collisionless Boltzmann equation.
CGM	circum-galactic medium.
CMB	cosmic microwave background.
DF	distribution function.
DM	dark matter.
ESO	European Southern Observatory.
ETGs	early-type galaxies.
FDS	Fornax Deep Survey.
FVSS	Fornax cluster VLT Spectroscopic Survey.
GCs	globular clusters.
HST	<i>Hubble Space Telescope</i> .
ICGCs	intra-cluster globular clusters.
ICL	intra-cluster light.
ICM	intra-cluster medium.
IFS	integral-field spectroscopy.
LOSVD	line-of-sight velocity distribution.
LTGs	late-type galaxies.
MFS	MeerKAT Fornax survey.
MW	Milky Way.
NFW	Navarro-Frenk-White.
NGFS	Next Generation Fornax Survey.
NGVS	Next Generation Virgo Survey.
PNe	planetary nebulae.
VIMOS	Visible Multi-object Spectrograph.
VLT	Very Large Telescope.
VST	VLT Survey Telescope.

List of Figures

1.1.	Illustration showing hierarchical merging of galaxies	3
1.2.	Image of galaxy cluster Abell 1689	6
1.3.	Image showing the extended halo of a simulated low surface brightness galaxy and NGC 3619	7
1.4.	Presence of ICL in the Virgo cluster core	8
1.5.	Illustration of the cosmic baryon cycle in the circum-galactic medium	11
1.6.	Observed color bimodality in GCs	14
1.7.	HI distribution at different physical scales	16
1.8.	Image showing the core region of the Fornax galaxy cluster	17
1.9.	Image showing the stellar streams between NGC1399 and NGC1387 in the Fornax cluster	17
1.10.	GCs surface density maps within the Fornax cluster	18
1.11.	MFS pointings over the Fornax cluster	19
2.1.	Layout of the VIMOS observations over the central square degree of the Fornax cluster	26
2.2.	Example of reduced VIMOS spectra showing the calcium triplet lines	27
2.3.	Example of pPXF fits to GC spectra with $S/N \sim 25$ and zoom-in view of the absorption features	29
2.4.	Example of pPXF fits to GC spectra with $S/N \sim 6$ and zoom-in view of the absorption features	30
2.5.	Signal-to-noise ratio vs. g -magnitude for the three classes of objects	32
2.6.	GCs Radial velocity comparison of duplicate measurements	33
2.7.	Radial velocity comparison of GCs with with the GC sample of Schuberth et al. (2010) and of Pota et al. (2018) as a function of g magnitude	34
2.8.	Radial velocity comparison with previous measurements	35
2.9.	Histogram and colour bimodality of the GCs in $g - i$ colour distribution	36
2.10.	Distribution of GCs (red dots) and UCDs (yellow dots) in the colour-colour and colour-magnitude diagram	36
2.11.	Radial velocity map of GCs within 1.5 square degrees of the Fornax cluster	37
2.12.	Rotational velocity of all, red and blue GCs within 30 arcminutes	38
2.13.	Phase-space diagrams of radial velocity vs. cluster-centric distance	39

2.14. Velocity dispersion profiles in the Fornax cluster core region as a function of projected distance from NGC 1399	41
2.15. Selection of potential ICGCs around NGC 1399 and NGC 1374	42
2.16. Radial velocity histograms of the full sample and the intra-cluster GCs	43
2.17. Azimuthal distribution of ICGCs selected outside $4r_{\text{eff}}$ radii around major galaxies	45
2.18. Radial velocity and $g - i$ colour histograms of the GCs in the intra-cluster regions	48
2.19. Distribution of ICGCs selected with a phase-space cut	49
2.20. Globular clusters with confirmed radial velocities (coloured dots) plotted over the surface density map of photometric GC candidates from the FDS (Cantiello et al., 2020)	50
3.1. Radial velocity map of GCs of NGC 1399 and the IC sample within 1.5 square degrees of the Fornax cluster	58
3.2. LOS velocities of our GC sample vs. cluster-centric distance	59
3.3. GCs radial surface density profiles around NGC 1399	60
3.4. Velocity dispersion and kurtosis profiles of the <i>inner</i> sample	62
3.5. Velocity dispersion and kurtosis profiles of the <i>full</i> sample	63
3.6. Rotational amplitude and velocity scatter of GCs.	64
3.7. Posterior distributions of the parameters from the two-component Jeans modelling using the Burkert halo	70
3.8. Posterior distributions of the parameters from the two-component Jeans modelling using the NFW halo	71
3.9. Velocity dispersion and kurtosis profiles of the <i>inner</i> sample, used for the mass-modelling	72
3.10. Posterior distributions of the parameters from the two-component Jeans modelling using the Burkert halo for the <i>full</i> sample	73
3.11. Posterior distributions of the parameters from the two-component Jeans modelling using the NFW halo for the <i>full</i> sample	74
3.12. Velocity dispersion and kurtosis profiles of the <i>full</i> sample, used for the mass-modelling	75
3.13. Enclosed mass profile of NGC 1399	76
3.14. Virial mass and concentration parameter relation	77
3.15. Velocity anisotropy distribution of GCs	79
4.1. HI distribution in the TNG50 halo 6 at redshift $z=0$, colour-coded with the HI column density	85
4.2. HI distribution in Fornax-like halos and in their IC regions	87
4.3. HI covering fraction profiles of Fornax-like halos	88
4.4. HI covering fraction profiles of intra-cluster region of Fornax-like halos	89
4.5. Distribution of HI in TNG50 halo 6 at redshift $z=0$ in the velocity map	90
4.6. Halo and intra-cluster cumulative HI covering fractions at $1 R_{\text{vir}}$ for three projected axes	91

4.7.	HI cumulative covering fraction profiles of Fornax-like halos in the velocity space	93
4.8.	Number of satellites as a function of intra-cluster HI mass	94
6.1.	Images of Hydra I and Antlia clusters	101
6.2.	Approved future FVSS observations of Fornax cluster	102
6.3.	Image of NGC 1427A galaxy	104
A.1.	Effect of initial radial velocity guesses on the resulting radial velocity measurements.	105
A.2.	Choosing pPXF polynomials	106
A.3.	Effect of higher order polynomials on radial velocity measurements.	107
A.4.	Example of a GC portfolio	108

List of Tables

2.1. Matched number of GCs from this study to previous studies	34
2.2. Bivariate Gaussian parameters using GMM	36
2.3. 2D KS test and properties of the ICGCs.	46
3.1. Best fit parameters of the Sersic profile for the GCs surface density profile .	61
3.2. Best fit parameter of the two-component joint modelling	69
4.1. TNG50 halos similar to the Fornax galaxy cluster	84
A.1. Excerpt of our VIMOS GCs catalogue.	109

1 | Introduction

Our curiosity to understand nature and its laws is fundamental in developing and driving scientific growth. Astronomy is one of the oldest sciences and is directly associated with the mystery of nature and the cosmos. Our current knowledge about the Universe is developed within the framework of the cosmological models describing the Universe as homogenous and isotropic in nature. Observationally supported by the overall homogenous distribution of galaxies and the isotropic presence of cosmic microwave radiation, these cosmological models are very successful in describing galaxy formation and evolution.

The standard cosmological model consists of three main components: matter, radiation and dark energy. The matter consists of baryonic particles that make up the visible Universe and the unknown nature of the non-baryonic cold-dark matter. Radiation consists of relativistic particles such as photons or high redshift neutrinos. Dark energy is a component which has the property of producing the accelerated expansion of the Universe.

The current observable structure in the Universe is believed to be generated from the initial inhomogeneity through quantum fluctuations in the early Universe. These fluctuations grow more prominent with time and structures merge leading to the formation of galaxies and large-scale structures such as galaxy clusters. This kind of formation scenario is known as the hierarchical structure formation and is well supported by observational studies. Galaxy clusters are the largest gravitationally bound systems in the Universe. Studying their assembly provides valuable insight into various aspects of astronomy, such as galaxy evolution and formation, gravitational structure formation, and intergalactic medium physics.

Nearby galaxy clusters offer an excellent opportunity to study them in great detail with ground-based observatories. In this thesis, I have studied the mass assembly of the nearby Fornax galaxy cluster using its globular clusters (GCs) as discrete kinematical tracers. I have explored the nature of intra-cluster globular clusters (ICGCs) in the Fornax cluster and have investigated their effect on mass modelling. For this work, I have used the observations obtained with the Visible Multi-object Spectrograph (VIMOS) instrument at the Very Large Telescope (VLT) of the European Southern Observatory (ESO).

To study the galaxy clusters from a theoretical point of view, I have studied the distribution of atomic hydrogen in the circum-galactic medium of galaxies in Fornax-like clusters utilising the latest TNG50 cosmological simulation. With this work, I predict the atomic HI covering fraction expected to be observed by the current MeerKAT Fornax survey (MFS).

In the following, I provide a brief overview of structure formation in the Λ Cold Dark Matter

1. Introduction

(Λ CDM) cosmological model, introduce galaxy clusters and the role of the environment in galaxy evolution and formation. I discuss the key science questions and scientific motivation related to the thesis in section 1.5 and present the thesis structure in section 1.6.

1.1 Λ CDM in nutshell

The two most significant observational evidences for the current cosmological models are the expansion of the Universe observed by Hubble and the detection of cosmic microwave radiation by Penzias and Wilson in 1965. In 1921, Edwin Hubble made a remarkable and important discovery showing that the recessional velocities of galaxies are linearly related to their distances. Initially predicted by George Gamow as the remnant of the primordial Universe, cosmic microwave background (CMB) radiation was detected in 1965. These two discoveries were significant in supporting the idea of an expanding and primordial hot and dense Universe known as the hot big-bang model and were the basis of the standard cosmological model.

Although the standard cosmological model was on the path to success, it had some issues, such as explaining the curvature of the Universe and, if the Universe was really isotropic and homogenous, how could we see the current large-scale structures? How could the CMB spectrum from two different directions have very similar temperatures? These issues were resolved by incorporating the idea that the Universe expanded rapidly on an exponential scale during the very early phase. This scenario was proposed by Alan Guth in 1981 and was termed as cosmic inflation (Guth, 1981).

Studying the velocities of galaxies in the Coma cluster in 1933, Fritz Zwicky provided the first hint of dark matter (DM) in the Universe (Zwicky, 1933). Later, significant work from Einasto, Ostriker and Peebles (Ostriker et al., 1974) showed that the Milky way would require an enormous halo to describe the velocities of its satellite galaxies. Studies of the rotational velocities of spiral galaxies with the 21 cm emission line of neutral hydrogen line also supported the idea of extended massive halos of DM in disc galaxies to explain their flat rotational velocity in the outer parts (Rubin & Ford, 1970; Rubin et al., 1978, 1980). Around the same time, a theoretical approach to galaxy formation and evolution was proposed by White & Rees (1978), suggesting that cool gas condenses in the gravitational potential of the merged DM halos forming the galaxies.

The detected anisotropies in the CMB also indicated that the initial perturbation of baryonic matter in the density field would not have been enough to form the cosmic structures. To explain the origin of large-scale structures, it required some non-baryonic matter with a more significant perturbation. This non-baryonic matter was suggested to consist of DM particles. Among the various proposed DM particles, such as warm or cold DM, the idea of cold DM is currently favoured in explaining the structure formation.

Together, these observations resulted in the emergence of the Λ CDM cosmological model, which is based on the mathematical framework of Einstein's General Relativity. The Λ CDM describes the Universe as spatially flat with around $\sim 95\%$ per cent content of the Universe

is DM and dark energy and the remaining $\sim 5\%$ baryonic matter that makes up the visible Universe. In the Λ CDM paradigm, Λ represents the cosmological constant and is associated with the negative pressure in a vacuum, and under general relativity, this leads to dark energy. The nature of DM and dark energy is unknown and is currently one of the biggest challenges in modern cosmology. However, the success of Λ CDM in explaining the observed cosmic structures and properties of galaxies has made it a reference cosmological model.

1.1.1 Structure formation in the Λ CDM framework

In the Λ CDM structure formation scenario, massive structures grow by the hierarchical merging of a smaller systems. Described within the context of the inflationary model, the quantum processes produced perturbations in the density field of the Universe and these initial perturbations grew larger due to gravitational instability leading to the formation of large-scale structures. Simply we can understand structure growth by understanding density perturbation's evolution. Considering a dimensionless parameter $\delta(r, t)$ called density contrast, which gives the difference between the mean density $\bar{\rho}(t)$ of the Universe and density at some point r (and at time t) and is expressed as:

$$\delta(r, t) = \frac{\rho(r, t) - \bar{\rho}(t)}{\bar{\rho}(t)} \quad (1.1)$$

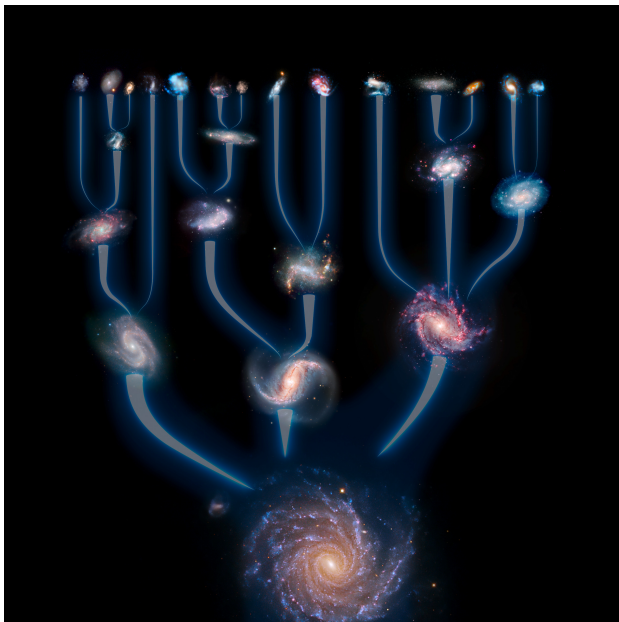


Figure 1.1.: Illustration showing hierarchical merging of galaxies in the Λ CDM framework (credit: ESO).

Assuming that fluctuations occur via gravitational instability and DM is the dominant component, we can consider the DM and baryons as a single fluid. Now imagine a different region in the Universe, and its density can be expressed as:

$$\rho(r, t) = [1 + \delta(r, t)]\bar{\rho}(r, t) \quad (1.2)$$

Due to self-gravity, this region will expand at a slower rate than the Universe's expansion rate. The evolution can be described within the linear regime if $\delta(r, t) \ll 1$. If, for another region, the initial density is sufficiently larger, then after some time, $t \ll t_i$, the density will be non-linear such that the system will collapse due its gravity and form a virialized system. The halo-mass function, a quantity describing the mass distribution of DM halos in the Universe, follows this argumentation in form of the Press-Schechter formalism (Press & Schechter, 1974).

The smaller systems virialize first with the accretion of diffuse baryonic matter, and

1. Introduction

merging these smaller systems leads to massive DM halos. Figure 1.1, depicts an illustration of the hierarchical merging showing the assembly of galaxies inside DM halos throughout cosmic time. The merging of halos with similar mass is known as a major merger and the merger of a massive halo with a smaller halo as a minor merger. The baryonic material settles into hydrostatic equilibrium within the potential well of the dark matter halo.

Besides the theoretical work, our knowledge and understanding of the DM halo structure are based on cosmological simulations. Using N-body DM only simulations [Navarro et al. \(1996, 1997\)](#) found that the radial density profile of DM halos can be fitted with the same shape profile, known as the Navarro-Frenk-White (NFW) profile :

$$\rho_{NFW}(r) = \frac{\rho_s}{\left(\frac{r}{r_s}\right) \left(1 + \frac{r}{r_s}\right)^2} \quad (1.3)$$

where, ρ_s and r_s are the characteristic density and radius. The physical origin of this near-universal profile is not well understood. [Syer & White \(1998\)](#) have suggested that the NFW profile arises as a natural consequence of the hierarchical merging. The inner slope of the NFW profile can be generalised, considering ρ scales as r^γ where, if γ is 1, it produces a cuspy profile and if $\gamma \leq 0$ produces a cored profile.

Observational studies of low mass systems, such as dwarf and ultra-faint galaxies, suggest that the DM density is constant in the inner region of the galaxies, having a cored profile similar to the Burkert profile ([Burkert, 1995](#)). This indicates that the inclusion of baryonic physics can change the nature of the DM profile, affecting the inner slope of the profile. [Dekel et al. \(2003\)](#) suggested that when the smaller DM halos are disrupted while merging or infalling, they could change their DM profile's inner slope, producing a cored nature of the profile.

Current cosmological simulations have been foundational in support of the Λ CDM model. Starting with the simple DM N-body simulations ([Press & Schechter, 1974](#); [Davis et al., 1985](#)), modern cosmological simulations include various particles and solve the coupled evolution of DM, gas, stars and black holes ([Nelson et al., 2019](#)). Large-volume cosmological models, for example, Illustris ([Vogelsberger et al., 2014](#); [Genel et al., 2014](#)), Magneticum ([Dolag et al., 2016](#)), EAGLE ([Schaye et al., 2015](#)) have been successful in producing results mostly consistent with observations and the large-scale structure of the Universe.

1.1.2 Formation and evolution of galaxies

Galaxies are the building blocks of the large-scale structure and can be defined as gravitationally bound systems of stars, gas, dust and a large amount of DM. During the seventeenth century, galaxies were first observed and detected as diffuse and fuzzy nebulae by C. Huygens and were later catalogued by C. Messier. With the advent of photographic plates and larger telescopes, Edwin Hubble, in 1925, detected variable stars in these nebulae and measured their distance, which established their extragalactic nature. Later, Hubble classified galaxies' shapes, producing the famous tuning fork diagram ([Hubble, 1926](#)). The Hubble classification

of galaxies was based on their visual morphology.

Broadly, galaxies can be classified into two primary classes: early-type galaxies (ETGs) and late-type galaxies (LTGs). The ETGs are composed of ellipticals and lenticular shaped galaxies, and LTGs consist of spirals and irregular galaxies. ETGs are among the most luminous objects in the Universe and have a smooth distribution of stars. They lack spiral arms and have little or no star-formation activity. In contrast to spiral galaxies, which are dominated by the ordered motion of stars, the kinematic structure of ETGs is dominated by the presence of random motions. LTGs consist of galaxies which are actively forming their stellar component. They are represented by the presence of stellar disks, spiral arms, bars and bulges. They contain cold gas which is related to their star formation activity.

Thanks to integral-field spectroscopy (IFS), we know that ETGs can have complex kinematical patterns, like decoupled kinematic components and rotating disks (for details see Cappellari, 2016). IFS surveys such as SAURON (Bacon et al., 2001; de Zeeuw et al., 2002), ATLAS3D Cappellari et al. (2011) significantly improved the classification of ETGs based on their kinematic patterns in two primary classes: regular and non-regular rotators (Krajnović et al., 2011). In the Λ CDM framework, their growth is postulated to consist of two stages, first in-situ with an intense burst of star formation and then ex-situ with the accretion or merger phase (Oser et al., 2010). In the ex-situ phase, the assembly occurs in a hierarchical way through merging of smaller DM halos which lead to the formation of a massive DM halo (Cooper et al., 2013; Pillepich et al., 2015)

1.2 Galaxy clusters

Many galaxies are located in larger structures such as groups and clusters. Groups usually are gravitationally bound, contain ~ 50 galaxies within a characteristic scale of ~ 1 Mpc and a velocity dispersion of ~ 500 km s $^{-1}$. Our own Milky Way (MW) is a part of a small group of galaxies called the Local Group. The Local Group consists of two main spiral galaxies: MW and Andromeda (M31), and many lower mass dwarf galaxies. The proximity of galaxies in the Local Group allows us to perform a detailed study of the interaction between its galaxies. Thanks to the Gaia space mission (Gaia Collaboration et al., 2016, 2018), our knowledge about the streams and substructures associated with the MW formation history has expanded rapidly (see for details Helmi, 2020).

In the case of aggregations of a few hundreds to a thousand galaxies, the system is classified as a galaxy cluster. Galaxy clusters are the largest gravitationally bound systems, whose assembly is driven by early mergers of massive galaxies embedded in big dark matter (DM) halos and sequential accretion of galaxy groups. Galaxy clusters are virialized objects having a virial mass of $10^{14-15} M_{\odot}$ and radii of a few megaparsecs. Commonly, galaxy clusters are classified based on the spatial distribution of their galaxies. A cluster showing a spherical symmetry is classified as a regular cluster, such as the Coma cluster. An irregular cluster shows the presence of substructures, such as the nearby Virgo cluster.

Galaxy clusters are essential probes for cosmological studies, as their spatial distribution

1. Introduction

and abundance give a direct hint about the initial condition and gravitational laws (Allen et al., 2011). In addition, individually, they act as ideal laboratories where we can see the interaction between galaxies and probe the role of clusters' environment on the evolution of galaxies. Therefore, understanding the formation and mass assembly of galaxy clusters is crucial to develop our understanding about galaxy evolution and formation.

Multi-wavelength studies of galaxy clusters have shown that they are composed of various components, including the luminous stars of galaxies, faint intra-cluster light, and hot intra-cluster medium. Figure 1.2 shows a color-composite image of the galaxy cluster Abell 1689. The mass in galaxy clusters is dominated by DM, about 80% of the total mass, and the remaining $\sim 20\%$ is baryonic matter (mainly in the form of hot gas). Stars represent around 1-5% of the total mass (Bykov et al., 2015). The intra-cluster medium in a galaxy cluster is filled with diffuse plasma, which is not associated with any individual galaxy. However, it shows a strong linear relation with the stellar mass, suggesting a co-evolving nature of the two components (Kravtsov & Borgani, 2012).

Nearby galaxy clusters like Fornax ($D \sim 20$ Mpc, Blakeslee et al., 2009), Virgo ($D \sim 16.5$ Mpc, Mei et al., 2007), as well as others such as Centaurus and Perseus provide a unique chance to study galaxy evolution and formation in a high-density environment in great detail. Especially the Fornax and Virgo clusters have been studied with multiple photometric and spectroscopic surveys. Photometric surveys with the Advanced Camera for Surveys at the *Hubble Space Telescope* (HST), such as the ACS Virgo Cluster Survey (ACSVCS) and the ACS Fornax Cluster Survey (ACSFCS) (Côté et al., 2004; Jordán et al., 2007) have been pioneers in exploring both clusters at high spatial resolution. The ACSVCS and ACSFCS focused on characterizing the global properties of the early-type galaxies and their surface brightness profiles. These surveys also produced globular cluster catalogues (Jordán et al., 2004, 2007, 2009), discussing the fundamental properties, for example, colour-bimodality (Peng et al., 2006), GCs luminosity function (Jordán et al., 2007), and their formation efficiency (Peng et al., 2008).

Other important photometric surveys focused on the Virgo and Fornax clusters are the Next Generation Virgo Survey (NGVS), the Next Generation Fornax Survey (NGFS) and the Fornax Deep Survey (FDS). The NGVS survey is a Canada-France Hawaii Telescope (CFHT) large program. It is an optical multi-band deep photometric program dedicated to study the baryonic structures in the Virgo cluster within its virial radius. The NGFS is also a multi-band photometric survey performed with the Dark Energy Camera mounted at the 4

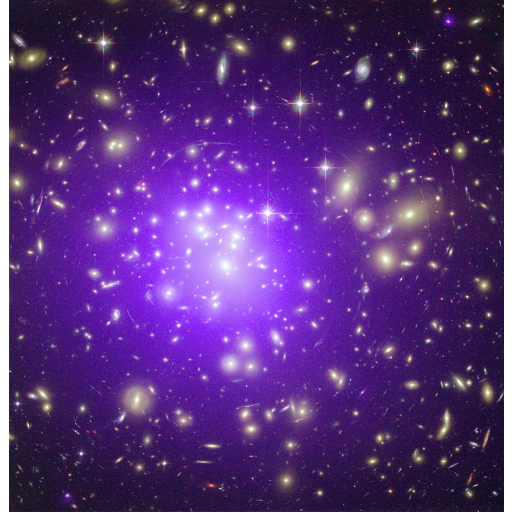


Figure 1.2.: Composite image of the galaxy cluster Abell 1689. The pink haze shows the X-ray emission observed with the Chandra X-ray Observatory and optical band observed with Hubble Space Telescope shows the galaxies (adopted from Kravtsov & Borgani 2012).

m Blanco telescope at Cerro Tololo Interamerican Observatory (CTIO) to study the Fornax cluster environment (Muñoz et al., 2015; Eigenthaler et al., 2018). In chapter 3, I present a photometric and spectroscopic survey related to the Fornax cluster, which is the basis of my thesis. In the following section, I present the observational imprints of hierarchical growth. Then I describe the Jeans dynamical modelling approach through which we can learn about the mass distribution of galaxy clusters. I also briefly discuss the role of cluster environment in galaxy evolution.

1.2.1 Observational imprints of the hierarchical growth

Since the assembly of galaxy clusters in the Λ CDM framework is driven by early mergers of massive galaxies embedded in big DM halos, we expect to see the signatures of accretion and mergers in galaxy clusters. Various physical processes act on infalling cluster galaxies, like ram pressure stripping (RPS), tidal disturbances, and harassment. These processes should leave visible imprints in the galaxies halos and in the cluster environment.

N-body and cosmological hydrodynamical simulation based on Λ CDM also predict that observable features are results of the galaxy interactions and merger events (Bullock & Johnston, 2005; Conroy et al., 2007; Mancillas et al., 2019; Remus & Forbes, 2022; Marini et al., 2022). Figure 1.3 shows an example of these features, where the left panel displays morphological features such as tidal tails, streams and shells in a simulated low surface brightness galaxy (Mancillas et al., 2019) and the right panel shows similar features observed in the elliptical galaxy NGC 3619 (Bílek et al., 2020).

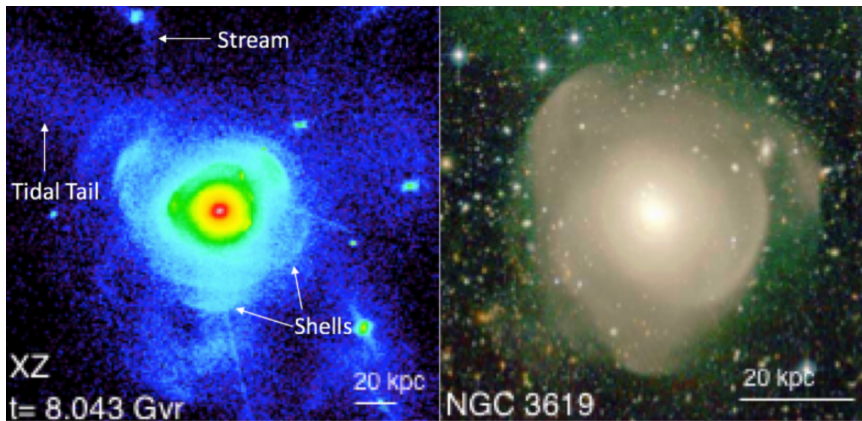


Figure 1.3.: **Left:** Extended halo of a simulated low surface brightness galaxy showing different morphological features (adopted from Mancillas et al., 2019). **Right:** NGC 1319, an observed low surface brightness galaxy having similar features as the simulated galaxy (adopted from Bílek et al., 2020).

1. Introduction

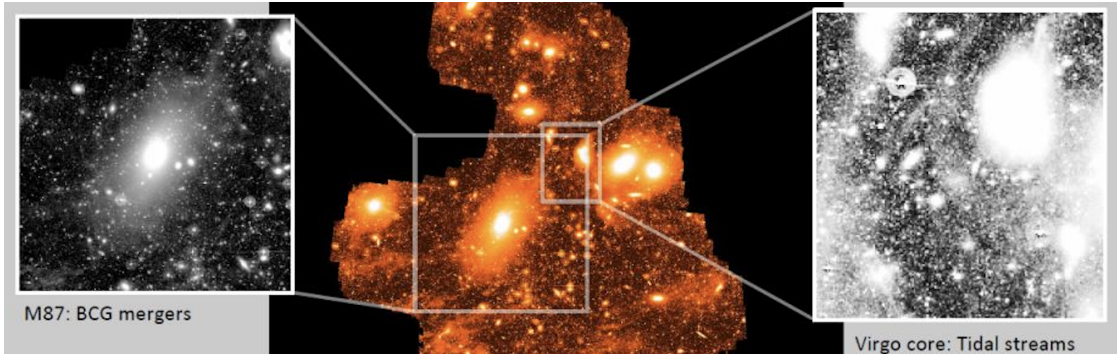


Figure 1.4.: Diffuse and faint ICL in the Virgo cluster core (adopted from [Mihos et al., 2005](#)).

Deep observations of nearby galaxy clusters have also confirmed the detection of faint and extended light known as the intra-cluster light (ICL) ([Montes & Trujillo, 2019](#); [Montes, 2022](#)). The ICL is a diffuse and faint baryonic component in galaxy clusters, which is not bound to any individual galaxy but to the cluster potential. ICL is believed to be generated by a combination of different processes happening in the cluster environment, so its challenging to identify the exact mechanism; however, it is clearly related to the dynamical history of the cluster. Figure 1.4 shows a deep wide-field image of the Virgo cluster and the extended halo around M87.

The physical scale of the ICL is similar to that of the DM halo distribution, so it is believed that it can be used as a tracer of the gravitational potential of galaxy clusters ([Montes & Trujillo, 2019](#); [Montes, 2022](#)). In future, deep photometric observations of a large sample of galaxy clusters could be used to properly quantify the role of ICL in determining the DM distribution.

1.2.2 Mass-modelling

Determining the total mass of galaxy clusters allows us to investigate their fundamental properties, such as the distribution of the baryonic and dark matter content, the nature of the DM halo profile, constraining the cosmological parameters and testing the structure formation scenario. We can learn about the total mass content of the galaxy clusters through various methods such as the Sunayev-Zeldovic effect from X-ray observations ([Zeldovich & Sunyaev, 1969](#)), gravitational lensing and projected phase space distribution of the cluster galaxies, or other dynamical tracers (see for details [Pratt et al., 2019](#)).

In the context of my work, I have used the projected line of sight velocity of GCs as discrete kinematical tracers for measuring the Fornax cluster mass profile. Here I provide the concept behind and a general overview of the Jeans modelling (for details see [Binney & Tremaine, 2008](#); [Mo et al., 2010](#)) and briefly summarize two other methods used for studying the dynamics of the gravitational potential system.

1.2.3 Jeans Modelling

Assuming that the galaxies are in a steady state and have a geometrical shape (either spherical, axis-symmetric or triaxial), their dynamics can be fully described by a six-dimensional distribution function (DF). The DF, $f(\mathbf{x}, \mathbf{v}, t)$, describes the number density of particles in phase space coordinates and time (bold characters denote the vector quantities). In the case of galaxies, the particles represent stars, while in the case of galaxy clusters, they are cluster member galaxies or other discrete kinematical tracers within the cluster environment.

Any dynamical system with a timescale larger than the relaxation time can be considered a collisionless system in which the constituent particles move under the influence of the gravitational field generated by the smooth mass distribution. As long as the stars are collisionless and are neither created nor destroyed, the flow in phase space must be conserved and is expressed as conservation of mass in terms of the continuity equation:

$$\frac{\partial \rho}{\partial t} + \nabla(\rho \mathbf{v}) = 0 \quad (1.4)$$

Here ρ is the density and \mathbf{v} is the velocity of the fluid in the phase space. Owing to the large relaxation time, galaxies can be considered collisionless systems. This allows the use of the collisionless Boltzmann equation (CBE), which is analogous to the continuity equation and describes the evolution of the DF in a given gravitational potential system as:

$$\frac{\partial f}{\partial t} + \mathbf{v} \nabla f - \nabla \phi \frac{\partial f}{\partial \mathbf{v}} = 0 \quad (1.5)$$

In the above equation, the gravitational potential is related to the total density through the Poisson equation :

$$\nabla^2 \phi = 4\pi G \rho \quad (1.6)$$

The CBE implies that the phase space density around a particle remains constant. Using velocity moments and the CBE, we can derive the Jeans equation which relates the observable quantities like velocity dispersion and mean stellar velocity to the gravitational potential of the galaxy. Assuming a spherical symmetry and non-rotating system, the Jeans equation can be written as:

$$\frac{d}{dr}(j\sigma_r^2) + \frac{2\beta}{r}j\sigma_r^2 = -j\frac{d\phi}{dr} \quad (1.7)$$

Here j is the tracer 3D number density, σ_r is the radial velocity dispersion, and ϕ is the gravitational potential. In equation 3.5, β is the tracer anisotropy:

$$\beta = 1 - \frac{\sigma_t^2}{\sigma_r^2} \quad (1.8)$$

Here $\sigma_t = \sigma_\phi = \sigma_\theta$ for a spherical symmetry.

1. Introduction

In the Jeans equation, the resulting mass profile and anisotropy is linked through a single equation (equ. 3.5). This produces the mass-anisotropy degeneracy (Mamon & Łokas, 2005). Traditionally, the approach is to consider different orbital distributions like radial, tangential or isotropic and solve equation 3.5 to obtain the projected velocity dispersion. The fourth moment of the line-of-sight velocity distribution (LOSVD) of kinematic tracers, kurtosis, contains information about the orbital distribution of the tracers. Solving the Jeans equation for the 4th moment of velocity can reduce and control the mass-anisotropy degeneracy. This procedure has been thoroughly applied and well tested for massive galaxies (see for details Napolitano et al., 2009, 2010, 2011, 2014).

In addition to the combined velocity dispersion and kurtosis analysis, the combination of different kinematical tracers is also a very powerful method to reduce or break the mass-anisotropy degeneracy. Distinct kinematical tracers in a given potential should result in a common mass profile, and this allows to obtain a constraint on their orbital anisotropies (Łokas & Mamon, 2003).

Other more general and advanced modelling methods are ‘made to measure’ N-body models (Syer & Tremaine, 1996) and ‘made to measure’ methods (Blaña Díaz et al., 2018), which are based on numerically solving the CBE for a given set of particles. Another important method for studying a dynamical system is Schwarzschild orbit-superposition modelling. In the orbit based modelling, a large orbit library is computed which covers the phase space structure of the potential (corresponding to the deprojected luminosity) and is fitted to the observed luminosity and kinematics. Although computationally challenging, the orbit based modelling has been pioneer in obtaining the supermassive black holes masses at the center of galaxies (Thomas et al., 2005; Cappellari, 2016; Mehrgan et al., 2019).

1.2.4 Role of cluster environment in galaxy evolution

Current observational studies have established that the galaxy cluster environment plays a significant role in galaxy evolution (for details see Boselli & Gavazzi, 2006, 2014). A direct observational evidence of structural and morphological transformation of galaxies in galaxy clusters is the increase in the population of red, HI deficient, massive galaxies with increasing environmental density in the cluster center (Oemler, 1974; Dressler, 1980). This is known as the density-morphology relation and is mainly governed by the cluster environment.

Among various processes, the effect of the cluster environment on galaxies can be broadly classified into two classes. The first consists of the interaction with the cluster’s gravitational potential, leading to tidal stripping and galaxy harassment, and the second consists of the interaction with the intra-cluster medium (ICM), resulting in the stripping of the gas content of a galaxy, known as ram pressure stripping (Gunn & Gott, 1972). These interaction phenomena most likely act together on a galaxy and affect its star formation rate, stellar, and gas content. To properly comprehend galaxy evolution in clusters, identifying and disentangling the dominant mechanism affecting the evolution is crucial. Usually, a combined approach of observations and simulations has been employed to understand the environmental effects on the evolution of cluster galaxies (Tonnesen et al., 2007; Yun et al.,

2019; Poggianti et al., 2017).

1.2.5 Circum-galactic medium

The impact of the cluster environment on galaxy evolution is strongly interlinked with the gaseous halo surrounding the galaxy known as the circum-galactic medium (CGM). As a result of hierarchical formation, a substantial amount of baryonic matter is expected to reside around the massive DM halo. In the current baryon cycling paradigm, the gas in the CGM plays a significant role in the evolution and transformation of galaxies. The CGM is the main venue where cosmological gas accretion and feedback occur, and these processes regulates star formation and quenching in galaxies.

Loosely, we can separate the gas within and around a halo into three regimes: first, the gas associated directly with the galaxy, known as the interstellar medium (ISM); second, gas located in between the ISM and the virial radius of the DM halo, defined as the CGM; and third, the inter-galactic medium, which is everything outside the virial radius. Figure 1.5 shows a cartoon illustration of the cosmic baryon cycle in the CGM.

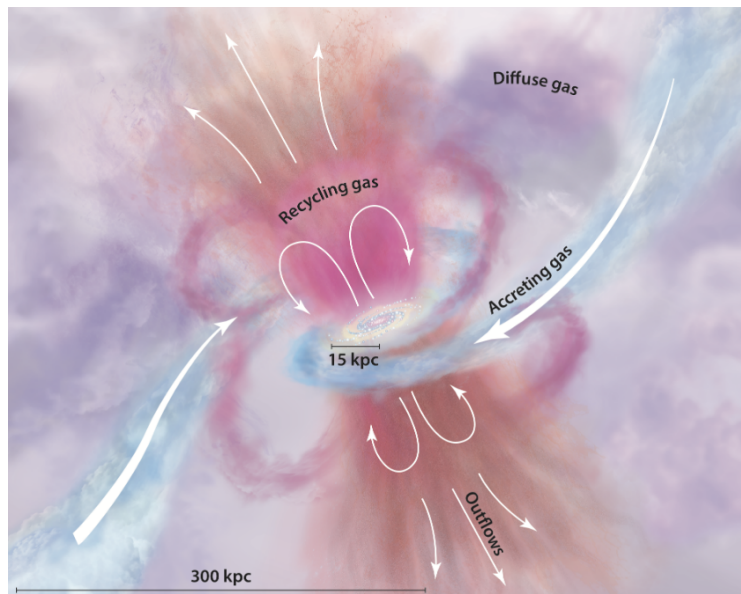


Figure 1.5.: Illustration of the cosmic baryon cycle in the CGM. The centre disk of the galaxy is fed by the accretion from the filamentary structure shown in blue colour. Pink and light orange colours depict the outflows and recycling gas, and purple surrounding indicates the diffuse gaseous halo (adopted from Tumlinson et al. 2017).

Cold gas in the CGM provides the fuel needed for star formation in galaxies. The CGM contains information about gas accretion and feedback driven by stellar and active-galactic nuclei outflows, which regulate the growth of galaxies. Most of the ejected gas remains bound to the CGM and falls back to the galaxy, enriching the metal content of the ISM. These processes lead to the development of the CGM as a multiphase and complex gaseous medium

1. Introduction

([Tumlinson et al., 2017](#)). These physical processes make the CGM essential to develop a comprehensive picture of galaxy evolution.

1.3 Importance of nearby galaxy clusters

So far, I have discussed the structure formation scenario within the Λ CMD framework, highlighting that galaxy clusters are essential systems in the Universe. Studying their mass assembly provides valuable insight into various aspects of astrophysics, such as galaxy evolution and formation, gravitational structure formation, and intergalactic medium physics. Deep photometric studies have confirmed the detection of intra-cluster light (ICL) and other discrete tracers, such as GCs and planetary nebulae (PNe). These structures are the remnants of past merging and accretion events in the cluster environment according to cosmological simulations.

Due to the low surface brightness of the outer halos of galaxies, kinematical details from integrated light at large radii are mostly inaccessible with current spectrographs. However, discrete tracers like GCs and PNe act as bright and compact kinematic tracers, which are observable to tens of effective radii of the massive central cluster galaxies. They play a significant role in learning about the galaxies' halos kinematics ([Longobardi et al., 2015, 2018a](#); [Hartke et al., 2018](#); [Dolfi et al., 2021](#)). They also are valuable kinematic tracers for understanding the dynamics of galaxy and their mass assembly. The detection of GCs in the intra-cluster regions allows exploring their effect on the dynamical mass modelling of a cluster as a whole.

Nearby galaxy clusters, such as Fornax and Virgo, provide an excellent opportunity to study their mass assembly using GCs as kinematical tracers. There are some interesting issues related to nearby galaxy clusters, such as the role of substructures in their mass assembly process. Another important and less explored topic is about the CGM of the central massive galaxies in nearby galaxy clusters. What are the physical characteristics of their CGM, such as cold gas content and its distribution in the cluster environment? I briefly mention these two issues in the following subsections and then discuss possible avenues to answer those questions.

1.3.1 Role of substructures

While the ICL is too faint for obtaining any spectroscopic and kinematic analysis, GCs associated with the ICL are bright and numerous. GCs are one of the most powerful tracers of the kinematic signatures of ongoing merging and accretion between the cluster's sub-systems ([Longobardi et al., 2015](#)). Section 1.3.3 presents in detail the observed properties of GCs and their role in tracing the mass assembly of galaxy clusters.

Substructures in galaxy clusters have a substantial impact on the dynamical mass estimates of clusters, and ignoring them in the mass modelling leads to erroneous cosmological inferences ([Old et al., 2017](#); [Tucker et al., 2020](#)). For example, studying the Hydra I cluster

stellar and GCs kinematics, [Hilker et al. \(2018\)](#) have reported that small-scale variations in kinematic parameters due to substructures can produce a notable change in the mass-modelling and over-estimate the DM halo mass of the central galaxy by a factor of four. Therefore, the identification and dynamical modelling of substructures in the outer halos of interacting galaxies in clusters is essential to understand their contribution to the overall cluster assembly and mass budget.

1.3.2 Intra-cluster medium of nearby galaxy clusters

Understanding the physical processes in the ICM is crucial for building a comprehensive picture of galaxy evolution. Various environmental processes, such as ram pressure stripping and tidal interactions, are mutually interlinked in developing a complex and multi-phase gaseous halo around the galaxies in the cluster environment. We consider all baryons between the halo's central galaxy interstellar medium and its virial radius as the intra-cluster medium ICM ([Tumlinson et al., 2017](#)).

For the low mass, star-forming galaxies, it is expected that its gaseous halo (CGM) can host an abundant amount of cold gas, that may be acquired as fuel for future star formation. In the case of the massive galaxies halos, there seems to be a lack of a cold gas reservoir, resulting in their quiescent nature, not showing any recent star formation activity ([Gauthier & Chen, 2011](#)). However, current observational ([Chen et al., 2018](#); [Berg et al., 2019](#); [Zahedy et al., 2019](#)) and simulation studies ([Rahmati et al., 2015](#); [van de Voort et al., 2019](#); [Davé et al., 2020](#); [Nelson et al., 2020](#)) suggest that at intermediate redshift ($0.3 \leq z \leq 0.8$), the CGM of the massive halos also contains a significant amount of cold gas. For example, [Chen et al. \(2018\)](#); [Zahedy et al. \(2019\)](#) studied the CGM of luminous red galaxies (LRG) at redshift $z \sim 0.21-0.55$ and found that they host high column density of cold gas tracers like HI and MgII. Other similar studies point toward the same conclusion that LRGs host an abundant amount of cold gas ([Zhu et al., 2014](#); [Lan & Mo, 2018](#); [Anand et al., 2021, 2022](#)).

In contrast to intermediate redshifts, investigation of ICM of the local Universe ($z \sim 0$) is limited to a few studies. Nonetheless, using the HI 21 cm emission line, radio observations have observed the abundant existence of cold neutral atomic gas around massive elliptical galaxies ([Serra et al., 2012, 2013a,b](#); [Young et al., 2014](#)). However, these observations are limited to within tens of kpc of the targeted galaxies and are not sensitive to low column densities, and therefore do not provide a comprehensive picture of the ICM. Observations of the nearby system from the MeerKAT, a new radio interferometer and a precursor of the square kilometre array (SKA) mid-frequency telescope ([Jonas & the MeerKAT Team, 2018](#)) provide an opportunity to probe the ICM of the massive halos in the local Universe. In Section 1.4.3, I briefly discuss the upcoming observations of MeerKAT of the Fornax galaxy cluster and the utilisation of the illustris TNG50 cosmological simulation to learn about the distribution of cold gas in the nearby massive halos.

1.3.3 Globular Clusters as tracers of galaxy mass-assembly

GCs are massive, compact, and mostly old star clusters that are found in almost all major types of galaxies (e.g. [Brodie & Strader, 2006](#)). The mean mass of GCs in the MW is $2 \times 10^5 M_{\odot}$, and they have typical half-light radii (radius containing half of the light of the cluster) of <10 pc. This high concentration of mass within a small radius makes GCs very dense and luminous stellar objects (V band absolute magnitude ~ 7.5 mag).

Observations of GC systems of massive galaxies have shown that GCs exist in two major subpopulations: red (metal-rich) GCs, and blue (metal-poor) GCs ([Kundu & Whitmore, 2001](#); [Peng et al., 2006](#)). This bimodal trend of GCs was first proposed by [Ashman & Zepf \(1992\)](#) for the galaxies NGC 4472 and NGC 5128, and later by [Ostrov et al. \(1993\)](#) for NGC 1399, the central galaxy of the Fornax cluster. Subsequently, using the Wide Field and Planetary Camera 2 of the Hubble Space Telescope, several studies confirmed the bimodality of GCs. Figure 1.6 shows the bimodal $g-i$ color histogram of GCs in NGC 1399.

The red GCs are found to have radial number density profiles similar to the integrated light of the central spheroids of their host galaxies, while blue GCs are spatially more extended into the intergalactic and intra-cluster regions and trace the metal-poor component of the stellar halos ([Schuberth et al., 2010](#); [Hilker et al., 2015](#); [Cantiello et al., 2018](#); [Pota et al., 2018](#)). The colour bimodality of GCs is believed to be mainly associated with their bimodal metallicity distribution, although the relation between colour and metallicity is not entirely linear ([Cantiello et al., 2014](#); [Fahrion et al., 2020b](#)).

These two GC subpopulations also show different kinematical characteristics. In most cases, the red GCs follow the stellar population kinematics of their parent galaxies, whereas blue GCs show a more erratic and complex kinematic behaviour ([Schuberth et al., 2010](#); [Cocato et al., 2013](#); [Napolitano et al., 2014](#); [Cantiello et al., 2018](#); [Pota et al., 2018](#)). The colour bi-modality and distinct kinematical behaviour have been explained as the result of a two-stage formation scenario for massive galaxies ([Ashman & Zepf, 1992](#); [Kundu & Whitmore, 2001](#); [Peng et al., 2006](#)). Cosmological simulations suggest that massive early-type galaxies grow and evolve in these two stages: first, rapidly with a high star formation rate and early compact mergers (in situ), and later through the continuous accretion of smaller systems that build up the extended halo populations.

The red metal-rich GCs are thought to have formed during the in situ star formation process, whereas the blue metal-poor GCs are added to the system through the accretion of

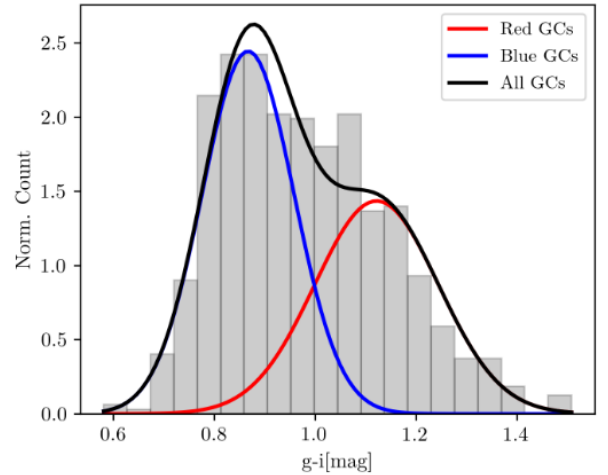


Figure 1.6.: Observed color bimodality in the GCs of NGC 1399 (adopted from [Chaturvedi et al. 2022](#))

1.3. Importance of nearby galaxy clusters

low-mass objects, such as dwarf galaxies (Forbes et al., 1997; Côté et al., 1998; Hilker et al., 1999a; Kravtsov & Gnedin, 2005; Tonini, 2013; Forbes & Remus, 2018). Various studies of GC populations in galaxy clusters revealed that so-called intra-cluster GCs (ICGCs) exist that are not bound to any individual galaxy (Williams et al., 2007; Bergond et al., 2007; Bassino et al., 2006; Schuberth et al., 2008; Peng et al., 2011; Alamo-Martínez et al., 2013). The ICGCs might represent the first GCs formed in a cluster potential or could be tidally released GCs from multiple galaxy interactions (White, 1987; West et al., 1995; Yahagi & Bekki, 2005; Madrid et al., 2018; Harris et al., 2020). Although their formation mechanism is still debated (Ramos-Almendares et al., 2018), their kinematics add additional constraints on the accretion and assembly history of their parent galaxy cluster.

1.3.4 Atomic hydrogen as tracer of the cluster environment

A simple and promising tool to explore the environment's role in galaxy evolution and CGM properties is to study the atomic hydrogen HI gas distribution in galaxies. HI is loosely bound to the galaxies on different physical scales and is susceptible to environmental processes. Using the HI 21 cm emission line, radio observations have demonstrated the abundant existence of cold neutral atomic gas around massive elliptical galaxies (Serra et al., 2012, 2013a; Young et al., 2014; Serra et al., 2013b).

HI is an excellent tracer of the different physical processes affecting the galaxies since it is influenced by both intra-cluster medium and gravitational potential (Boselli & Gavazzi, 2006). HI is associated with galaxies on different physical scales ranging from local ISM (~ 30 -50 kpc), CGM (~ 300 kpc) and inter-galactic medium (>300 kpc). Figure 1.7 shows an example of the HI distribution at different physical scales. The left panel shows the HI contour (at ISM scale) of the low mass galaxy NGC 1427A in the Fornax cluster extending to a scale of tens of kpc. The middle panel shows HI clouds at CGM-scale (green colour) associated with NGC 1316, the central galaxy of the Fornax A group, extending to ~ 100 kpc. The right panel shows HI clouds (blue colour) at the IGM scale associated with the group of four galaxies HCG44.

1. Introduction

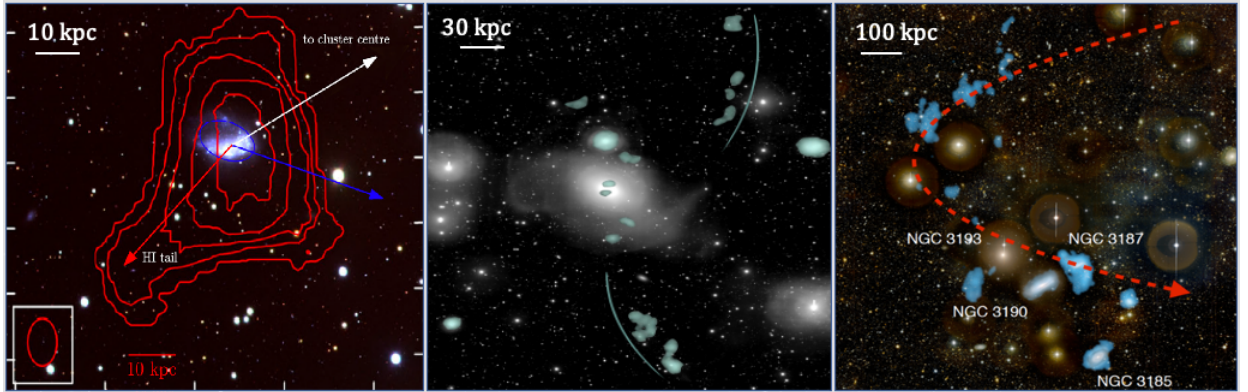


Figure 1.7.: Examples of HI distributions at different physical scales. **Left:** At ISM level, HI distribution around the low mass galaxy NGC 1427A. **Middle:** At CGM scale, HI clouds (green colour) around NGC 1316, the central massive galaxy of a Fornax cluster subgroup. **Right:** At IGM scale, HI clouds (blue colour) around the galaxy group HCG44. The plots are adopted from left to right from [Lee-Waddell et al. \(2018a\)](#); [Serra et al. \(2019, 2013a\)](#), respectively.

This kind of association of HI to the galaxies makes it a critical probe to learn about the environmental impact and to study the CGM. However, a quantified and detailed study of the role of environmental impact on galaxies' HI content is still missing for a galaxy cluster. Also, we need detailed and low column density HI surveys of galaxy clusters for a direct comparison with the outcome of hydrodynamical simulations.

1.4 Fornax galaxy cluster

The Fornax cluster is a very interesting and dynamically evolving environment. It is the most massive galaxy overdensity within 20 Mpc after the Virgo cluster, and therefore is an ideal target to study the effect of the environment on the structure and assembly of galaxies of any type in detail ([Iodice et al., 2016, 2019](#)). Due to its proximity, Fornax provides a unique opportunity to map its complex kinematics from the core out to half of its virial radius ($R_{\text{vir}} \sim 0.7$ Mpc) using GCs as kinematic tracers. This allows us to connect the large-scale kinematics of the major galaxies down to the scale of dwarf galaxies, which constitute the majority of kinematic sub-structures and build a detailed mass model of the cluster.

Thanks to the MeerKAT Fornax Survey (MFS, [Serra et al. 2016](#)), a HI and radio continuum survey of the Fornax galaxy cluster, it is now possible to study the HI gas distribution with a high sensitivity reaching down to a limit of $\sim 10^{18\sim 19}$ cm^{-2} at a resolution of $\sim 1\text{-}10$ kpc. With MFS, the ICM of the nearby Fornax cluster can be studied in detail and can be used to test high-resolution cosmological simulations. MFS, combined with the latest Illustris TNG50 cosmological simulations, provide a unique opportunity to study the ICM of nearby massive halos using radio and simulation studies.

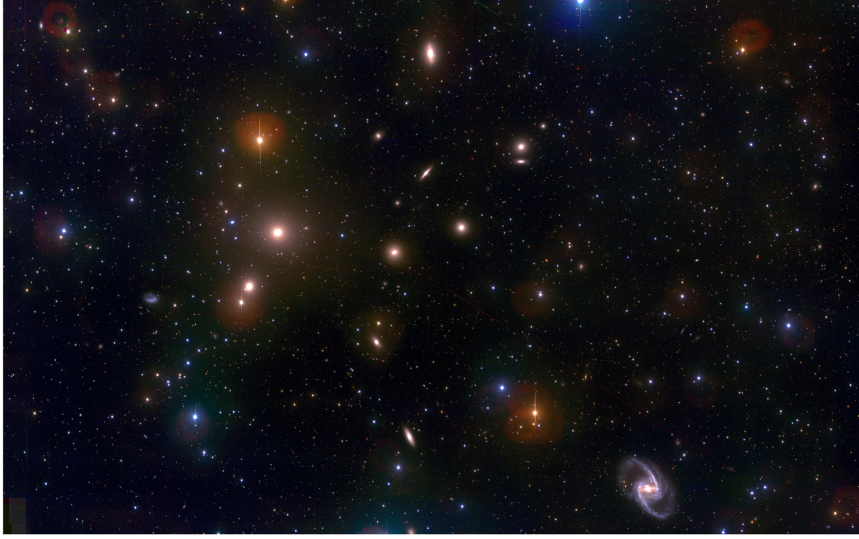


Figure 1.8.: A colour composite image (u , g and i bands) of the Fornax galaxy cluster showing its major galaxies. The central galaxy NGC 1399 is the brightest object on the left side of the image. North is up, and east is on the left. (credit: ESO)

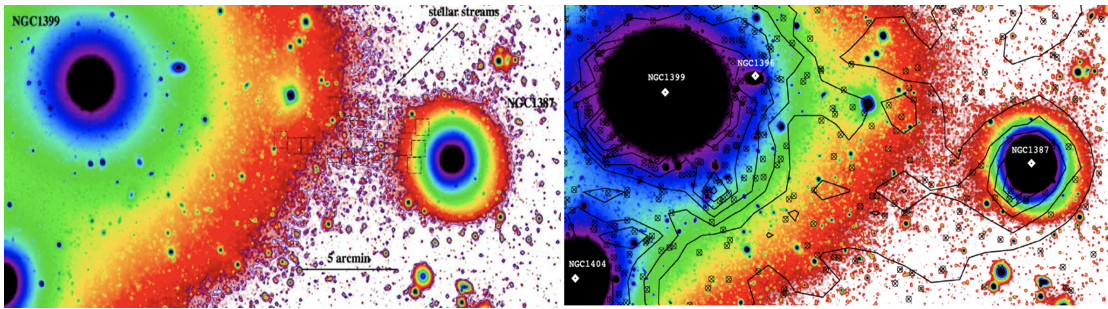


Figure 1.9.: **Left:** Enlarged g band image of the core region of NGC 1399 showing the presence of stellar streams along the western side (left side of the image) of NGC 1399 and its neighbouring galaxy NGC 1387 (adopted from Iodice et al., 2016). **Right:** GCs density contours overlotted on the left image (adopted from D’Abrusco et al., 2016).

1.4.1 GCs system of the Fornax cluster

In the past decades, the GC system of the Fornax cluster has been photometrically examined in great detail. Various imaging surveys such as the ACSFCS with the HST (Jordán et al., 2007, also see Puzia et al. 2014), the NGFS (Muñoz et al., 2015), and the Fornax Deep Survey (FDS) with the Very Large Survey Telescope (VST) (Iodice et al., 2016) have added a wealth of information about galaxies and GCs in the Fornax cluster. Photometric studies from D’Abrusco et al. (2016) and Iodice et al. (2019) have revealed that despite the regular appearance of the Fornax cluster, its assembly is still ongoing, as evidenced by the presence of stellar and GC tidal streams. Figure 1.9 (left panel) shows the presence of stellar streams along the western side of NGC 1399 and its neighbouring galaxy NGC 1387, and the right panel shows the GCs density contours overlotted to the left image.

1. Introduction

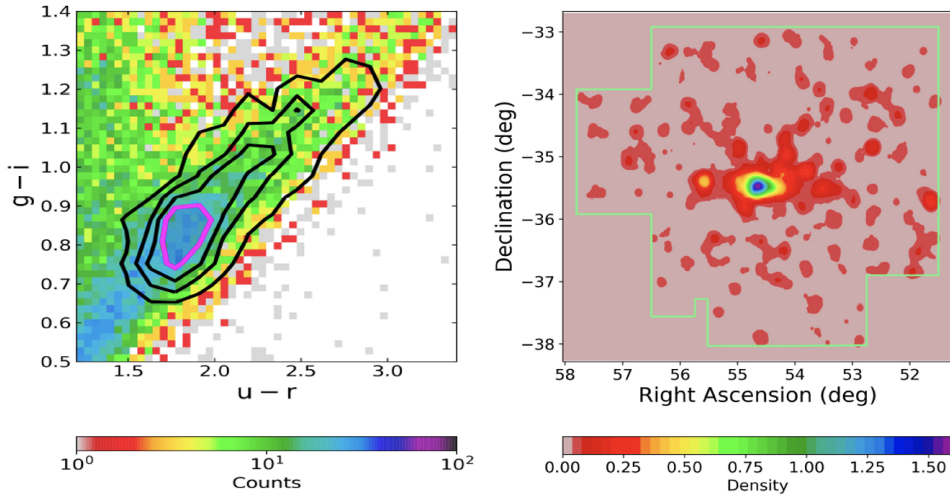


Figure 1.10.: Colour distribution and surface density map of GCs in the Fornax cluster. **Left:** GCs selection in a colour-colour plot. The pink contour indicates the selection based on the tightest constraint in the colour-colour values, and the black contours denote selections with relaxed values. **Right:** Spatial density map of GCs belonging to the pink contour of the colour-colour plot.

Most recently, using the FDS with the VLT Survey Telescope (VST) [Cantiello et al. \(2020\)](#) have produced the largest photometric catalogue of compact and slightly extended objects in the Fornax cluster over an area of ~ 27 square degrees. Figure 1.10 shows the surface density map of GC candidates from the FDS. The pink contour in the left panel shows the GC selection based on tight constraints in the colour-colour plot, and the right panel shows the spatial distribution of GC candidates lying within the pink contour. [Cantiello et al. \(2020\)](#) confirmed the previously detected extended spatial overdensity of GCs along the east-west side of NGC 1399 ([Schuberth et al., 2008](#); [D’Abrusco et al., 2016](#)).

Due to its proximity, Fornax provides a unique opportunity to map its complex kinematics from the core out to at least ~ 350 kpc using GCs as kinematic tracers. Based on the radial velocities of GCs and PNe, the Fornax Cluster VLT Spectroscopic Survey (FVSS) has obtained an extended velocity dispersion profile of the central galaxy out to 200 kpc ([Pota et al., 2018](#); [Spiniello et al., 2018](#)). This has allowed us to connect the large-scale kinematics of the major galaxies to the small-scale stellar halo kinematics of the central galaxy NGC 1399.

1.4.2 Mass-modelling of the Fornax cluster

The earliest approach to dynamically model the Fornax central galaxy NGC 1399 was made by [Kissler-Patig et al. \(1999\)](#), [Saglia et al. \(2000\)](#), and [Napolitano et al. \(2002\)](#). Later, major and crucial work was presented by [Schuberth et al. \(2010\)](#), who used 700 GCs within 80 kpc of the Fornax cluster as dynamical tracers to place constraints on the properties of the central DM halo.

An important missing piece of information to comprehend the complete mass assembly of Fornax is to understand the origin and kinematical behaviour of its intra-cluster population

and the disturbed outer halos of interacting cluster galaxies. Therefore, the identification and proper kinematical description of dynamically cold substructures and outer halos of interacting galaxies in the cluster are essential for understanding how these structures formed, and the cluster galaxies assembled and evolved. These substructures have to be taken into account in the mass modelling.

Using a novel cold structure finder algorithm, [Gatto et al. \(2020\)](#) made the first attempt to search for cold kinematical substructures in Fornax based on the GC and PNe data of [Pota et al. \(2018\)](#) and [Spiniello et al. \(2018\)](#). This has revealed at least a dozen candidate streams in the combined kinematical information of the PNe and GCs dataset of the Fornax cluster VLT Spectroscopic Survey (FVSS) ([Napolitano et al., 2021](#)). These substructures can then be subtracted from the underlying discrete radial velocity field in the Fornax core for unbiased dynamical models. Since the work of [Schuberth et al. \(2010\)](#) about ten years ago, a major dynamical study of the Fornax cluster is still lacking, and so far, no disturbed halo features of central cluster galaxies and no intra-cluster substructures were taken into account in a thorough dynamical model of the Fornax cluster core.

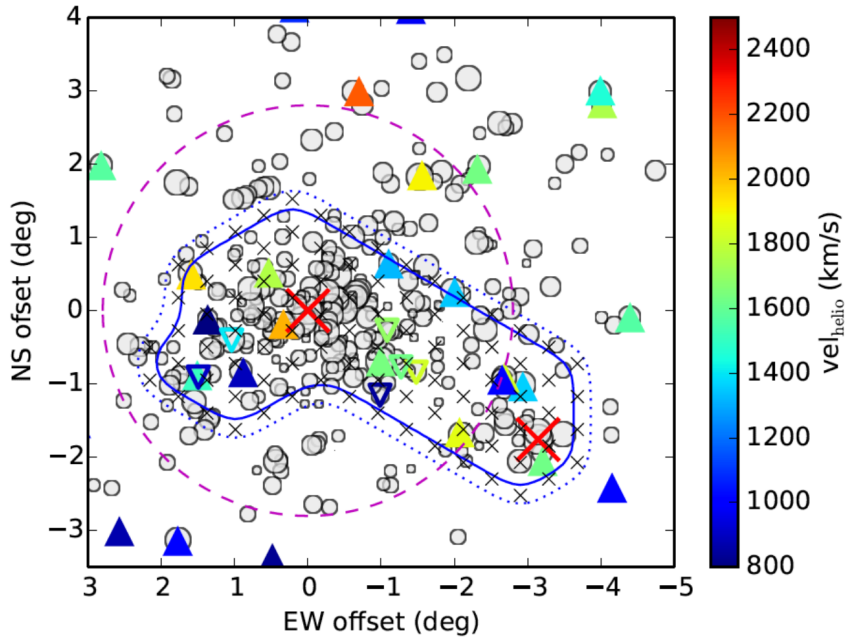


Figure 1.11.: MFS pointings over the Fornax cluster (adopted from [Serra et al. 2019](#)). The black cross denotes the 86 pointings over a region of 11.8 deg^2 marked as a blue contour. The open grey circle indicates the member galaxies of the Fornax cluster, and the triangle marks the galaxies detected in the HI survey. The two red crosses mark the cluster central galaxy NGC1399 and nearby subgroup NGC1316.

1. Introduction

1.4.3 ICM of Fornax cluster-like halo in cosmological simulations

The dense and dynamic environment of the Fornax cluster also provides a chance to explore the ICM at low redshift in great detail. With a HI column density sensitivity down to 10^{18-19} cm^{-2} and a spatial resolution of kpc scale, the MFS is dedicated to study the effect of the cluster environment on the HI distribution within Fornax. MFS is one of the extensive survey Projects of the MeerKAT telescope and will detect HI in the Fornax intra-cluster region. Figure 1.11 MFS shows layout. MFS is designed to observe the Fornax cluster over a region of $\sim 12 \text{ deg}^2$ of the Fornax cluster. It is an ongoing survey covering a wide range of Fornax environmental densities. The recent availability of high-resolution TNG50 cosmological simulations provides an unprecedented opportunity to predict the upcoming MFS survey results and test the simulations against the MFS observations in order to learn about the CGM properties of member galaxies in Fornax cluster-like halos and its overall ICM.

1.5 Motivation behind this thesis

As discussed in the previous section, the Fornax cluster is a very interesting and important system and provides an excellent opportunity to study its mass assembly using its GCs system. The upcoming MeerKAT Fornax Survey and high-resolution TNG50 cosmological simulations also provide a chance to learn about the ICM of massive systems at low redshift. Here I list the key questions that my thesis addresses in the context of Fornax cluster GC populations, its mass modelling and the nature of its intra-cluster medium:

- *How are the red (metal-rich) and blue (metal-poor) GC subpopulations distributed in the phase space of the Fornax galaxy cluster?*
- *What is the nature of the intra-cluster GCs in Fornax? Could we provide any kinematical characterisation of the photometrically discovered ICGCs?*
- *What could be the possible effect of including ICGCs in the dynamical mass modelling of the Fornax galaxy cluster?*
- *What is the orbital distribution of the ICGCs?*
- *How is the cold atomic HI gas distributed in the Fornax galaxy cluster environment? How much cold gas is present in the IC medium?*

1.6 This thesis

My thesis' primary goal is to understand the mass assembly of the Fornax cluster by performing a mass-modelling of the cluster using its GCs as discrete kinematic tracers. Using multi-object VIMOS spectroscopic data observed within the FVSS, I have kinematically characterised the GCs of the Fornax cluster. I have performed the mass modelling of the

Fornax cluster and have investigated the role of sub-structures and IC GCs on the baryonic and dark matter distribution of the Fornax cluster. Lastly, I have studied the distribution of the cold gas in Fornax-like halos in the TNG50 cosmological simulations and have predicted the expected HI covering fraction for the upcoming MFS survey. This thesis is structured as follows:

- **Chapter 2:** This chapter briefly introduces the FVSS and details the data reduction, techniques and methods for deriving the radial velocities of GCs from VIMOS observations. Combined with previous literature velocity measurements, I compile the most extensive GCs radial velocity catalogue of the Fornax cluster. Lastly, comparison with the photometric catalogue and characterization of IC GCs are presented. The content of this chapter was an original published paper in [Chaturvedi et al. \(2022\)](#).
- **Chapter 3:** In this chapter, I use the radial velocity catalogue produced in chapter 2 to perform the mass-modelling work of the central galaxy of the Fornax cluster. Using the spherical Jeans modelling, I perform a two-component dispersion-kurtosis analysis to obtain the mass profile of NGC 1399 out to 200 kpc. I discuss the effect of including the IC GCs in the mass modelling and the orbital constraints on the GCs obtained from the mass-modelling work. The content of this chapter is based on *Chaturvedi et. al 2023, in prep, A&A*, which will be submitted soon.
- **Chapter 4:** In this chapter, I have studied the CGM of Fornax cluster-like halos. In particular, I present the distribution of atomic hydrogen in galaxy clusters similar to the Fornax cluster utilizing the TNG50 simulations and using observational criteria similar to MFS. This chapter's goal is to predict the HI covering fraction expected for the MFS. I also discuss the presence of HI clouds in the IC region observed in the simulated galaxy clusters in the TNG50. The content of this chapter is based on *Chaturvedi et. al 2023, in prep, ApJ*, which will be submitted soon.
- **Chapter 5:** In this chapter, I present the thesis' primary results and conclude on the mass assembly of the Fornax cluster.
- **Chapter 6:** Lastly, an outlook of future research is presented. I discuss upcoming observational data within the FVSS framework, intending to further understand the origin of the IC GCs.

2 | Kinematical characterisation of globular clusters in the Fornax galaxy cluster

The Fornax cluster provides an unparalleled opportunity for investigating the formation and evolution of early-type galaxies in a dense environment in detail. Several photometric studies of the Fornax cluster have shown evidence of the substructures and intra-cluster globular clusters (GCs). In this chapter, I aim at kinematically characterising photometrically detected GCs candidates in the core of the cluster. We used spectroscopic data from the Visible Multi Object Spectrograph at Very Large Telescope (VLT/VIMOS) from the FVSS survey in the Fornax cluster, covering one square degree around the central massive galaxy NGC 1399. The content of this chapter is based on [Chaturvedi et al. \(2022\)](#), published in *Astronomy & Astrophysics*, 657, A93.

2.1 Introduction

Low surface brightness of the outer halos of galaxies, prevents from getting kinematical details from integrated light at large radii. Discrete tracers such as globular clusters and planetary nebulae (PNe) play a significant role in learning about the halos kinematics. These are bright sources that are easily detectable in the outskirts of galaxies ([Dolfi et al., 2021](#); [Longobardi et al., 2015, 2018a](#); [Hartke et al., 2018](#)). PNe represent a post-main-sequence evolutionary stage of stars and are mainly associated with the stellar populations and integrated light of the galaxies ([Douglas et al., 2007](#); [Coccatto et al., 2009](#); [Spiniello et al., 2018](#)). Globular clusters (GCs), on the other hand, are massive, compact, and mostly old star clusters that are found in almost all major types of galaxies (e.g. [Brodie & Strader, 2006](#)).

Observations have shown that GCs exist in two major subpopulations: red (metal-rich) GCs, and blue (metal-poor) GCs. The red GCs are found to have radial number density profiles similar to the integrated light of their host galaxies, while blue GCs are spatially more extended into the intergalactic and intra-cluster regions and trace the metal-poor component of the stellar halos ([Schuberth et al., 2010](#); [Hilker et al., 2015](#); [Cantiello et al., 2018](#); [Pota et al., 2018](#)). These two subpopulations of GCs also show different kinematical characteristics. Properties like colour bi-modality and distinct kinematical behaviour make

2. Kinematical characterisation of globular clusters in the Fornax galaxy cluster

them privileged discrete tracers for the dynamical study of individual galaxies, as well as of the mass assembly of galaxy clusters.

Recent advancements in discrete dynamical modelling such as Jeans dispersion-kurtosis, incorporating high-velocity moments (Napolitano et al., 2014), and chemodynamical modelling methods (Zhu et al., 2016a) allow the unification of several physical properties of discrete tracers at once, such as their positions, velocities, and also colours and metallicities. This has brought a significant improvement and produced better constraints on the mass modelling and orbital anisotropy of the tracers (Watkins et al., 2013; Zhu et al., 2016b,a). Recently, Li et al. (2020) used GC kinematics to study the mass distribution and kinematics of the giant elliptical galaxy M87 in the centre of the Virgo cluster based on 894 discrete tracers. The M87 GC system (GCS) and the core of the Virgo cluster are a well-explored environment in this respect.

In the past decade, the GC system of the Fornax cluster has been photometrically examined in great detail (Jordán et al., 2007; Puzia et al., 2014; Muñoz et al., 2015). Photometric studies from D’Abrusco et al. (2016), and Iodice et al. (2019) have detected the presence of stellar and GC tidal streams. Most recently, Cantiello et al. (2020) have produced the largest photometric catalogue of compact and slightly extended objects in the Fornax cluster over an area of ~ 27 square degrees. Based on the radial velocities of GCs and PNe, the Fornax Cluster VLT Spectroscopic Survey (FVSS) has obtained an extended velocity dispersion profile of the central galaxy out to 200 kpc (Pota et al., 2018; Spiniello et al., 2018). This has allowed us to connect the large-scale kinematics of the major galaxies to the small-scale stellar halo kinematics of the central galaxy NGC 1399.

The low recovery fraction of the GC radial velocity measurements from the earlier FVSS results (Pota et al., 2018) and the improvement of the VIMOS ESO pipeline motivated us to reanalyse the VLT/VIMOS data of the Fornax Cluster. Here in this chapter, I present the radial velocity catalogue of GCs in an area of more than two square degrees, corresponding to 250 kpc of galactocentric radius.

This chapter is organised as follows: In Section 2.2 we describe the observations and data reduction. The radial velocity measurements are presented in section 2.3 and the results in section 2.4. In Section 2.5 we discuss the results and present the photometric and spatial distribution of our GC catalogue. Section 2.6 summarises our results and presents the scope of future work. In Appendices A.1 and A.2 we describe some tests we performed for the radial velocity analysis and an object portfolio used for visual inspection. In Appendix A.3 we show an excerpt of the VIMOS data GC catalogue from this study. The full catalogue is available online. Throughout the paper, we adopt a distance to NGC 1399 of $D \sim 19.95$ Mpc (Tonry et al., 2001), which corresponds to a scale of 5.8 kpc per arcmin.

2.2 Observations and data reduction

This work examines the detection and kinematical characterisation of GCs in the Fornax cluster core within one square degree. We have reanalysed Fornax cluster VLT/VIMOS

spectroscopic data taken in 2014 and 2015 under the ESO program 094.B-0687 (PI: M. Capaccioli). For a detailed description of observations preparation and target selection, we refer to Pota et al. (2018). Here we briefly summarise the observation details and present the new data reduction.

2.2.1 Photometry and globular cluster selection

The Fornax Deep Survey (FDS, Iodice et al., 2016) and Next Generation Fornax Survey (NGFS, Muñoz et al., 2015) formed the photometric data base for selecting GC candidates for the VIMOS/VLT spectroscopic survey. The FDS deep multiband (u , g , r and i) imaging data from OmegaCAM cover an area of ~ 30 square degrees out to the virial radius of the Fornax cluster. NGFS is an optical and near-infrared imaging survey and covers nearly the same area as the FDS survey.

Globular cluster candidates for spectroscopic observations were selected based on dereddened g - and i -band magnitudes from the FDS and preliminary VISTA/VIRCAM photometry in the K_s band from the NGFS. Additionally, wide-field Washington photometry (Dirsch et al., 2004; Bassino et al., 2006) was used to construct the $C - i$ versus $i - K_s$ diagram to select the bona fide GCs. Hubble Space Telescope/ACS photometry was used to find additional GCs in the central regions of NGC 1399 (Puzia et al., 2014). Finally, with a magnitude restriction of $17.0 < i < 23.0$ mag, a total of 4340 unique spectroscopic targets were selected. This selection on purpose also includes some background galaxies and compact sources outside the selection criteria whenever there was space for additional VIMOS slits.

2.2.2 Observations

The spectroscopic observations for this study were carried out with the Visible Multi Object Spectrograph (VIMOS, LeFevre et al., 2003) at the VLT and were acquired in ESO Period 94 between October 2014 and January 2015. A total of 25 VIMOS pointings were defined to cover the central square degree of the Fornax cluster. Figure 2.1, shows the layout of the observations, adopted from Pota et al. (2018). Each pointing consists of four quadrants of 7×8 arcmin². The MR grism was used together with filter GG475, which allows a multiplexing of two in spectral direction with a spectral coverage of 4750-10000 Å at resolution with a full width at half maximum (FWHM) of 12 Å. Three exposures of 30 minutes each were taken for each pointing.

2.2.3 Data reduction

The data reduction was performed with the VIMOS pipeline version 3.3.0 incorporated in the ESO Reflex workflow (Freudling et al., 2013). The reduction follows the steps described in Pota et al. (2018). The dataset of each VIMOS pointing consisted of biases, flat fields, scientific spectral images, and arc lamp spectra. The older version of the VIMOS pipeline, used for the analysis performed in Pota et al. (2018), did not correct for flexure-induced

2. Kinematical characterisation of globular clusters in the Fornax galaxy cluster

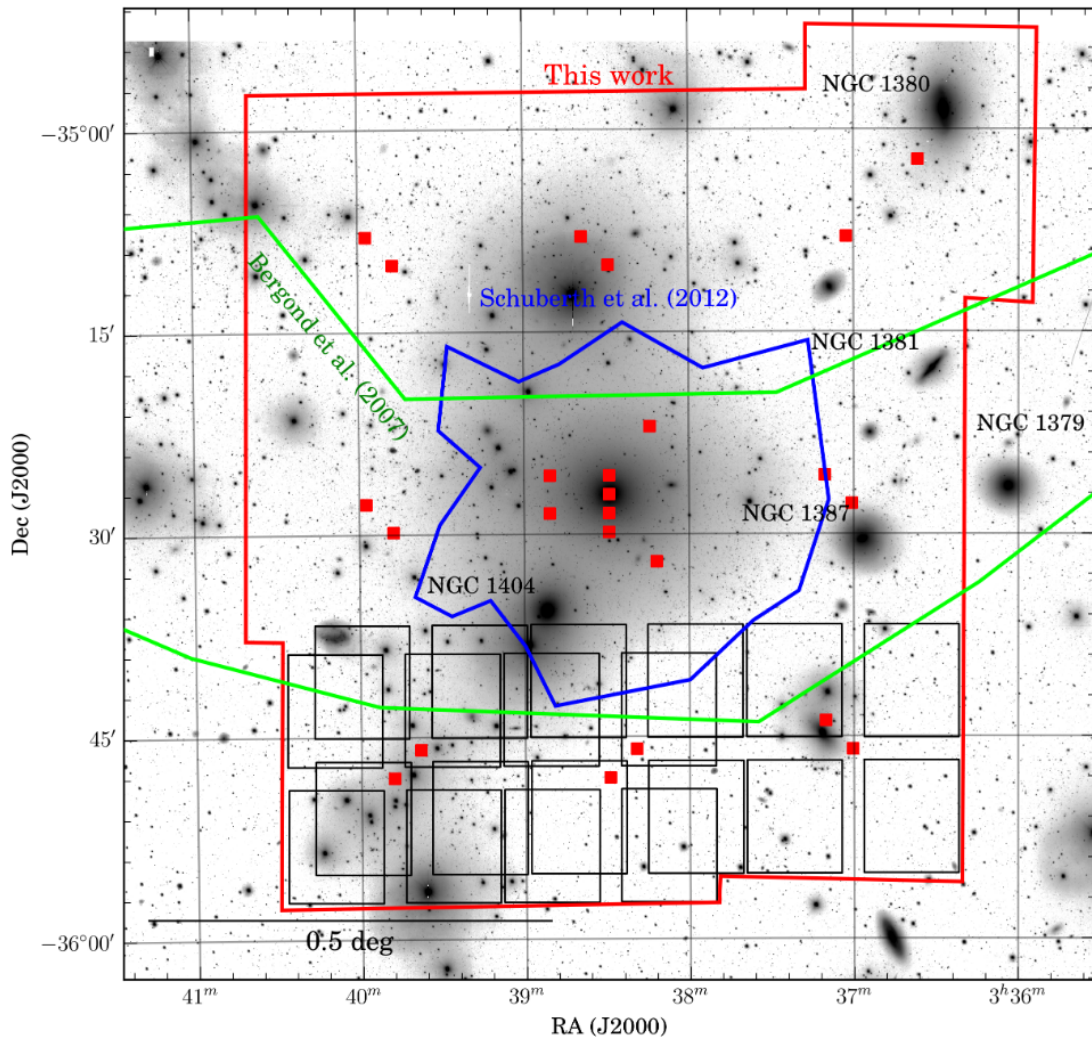


Figure 2.1.: The red box shows the coverage of the VIMOS observations (in total 25 pointings), plotted over the VST/OmegaCAM pointing in the g band. Regions marked in green and blue show the studies of Bergond et. al 2007 and Schuberth et. al 2010, respectively. Black squares within the red box show the VIMOS masks covering a field of $4 \times (7 \times 8 \text{ arcmin}^2)$.

wavelength shifts in multiple science exposure before their combination. This caused an incorrect absolute wavelength calibration and line broadening in the stacked spectra. [Pota et al. \(2018\)](#) manually corrected for this limitation by applying the median wavelength shift of the second science exposure to the final stacked spectra. On the other hand, the improved pipeline version we used for our work takes care of wavelength shifts before stacking the individual spectra and prevents the line broadening effects. We confirmed this by reducing the individual exposures of a few VIMOS pointings and compared them with the final stacked reduced spectra.

In Figure 2.2 we show the CaT region of the reduced individual spectra and the stacked one for one example case. Red, green, and blue show the three single exposures. The final stacked spectrum is shown in black. We repeated this test for several masks of different pointings, and no significant broadening was noted. We verified this quantitatively by fitting a Gaussian to the CaT line at 8842 \AA to the stacked and individual exposures of spectra with different signal-to-noise ratios (S/Ns). The scatter among the mean positions of the CaT at 8842 \AA line was found to be within the 10% spaxel resolution limit of 2.58 \AA for the used VIMOS grism. In order to obtain the final wavelength calibration, we provided our own skyline catalogue to calculate the residual shifts from the sky emission lines and corrected for them.

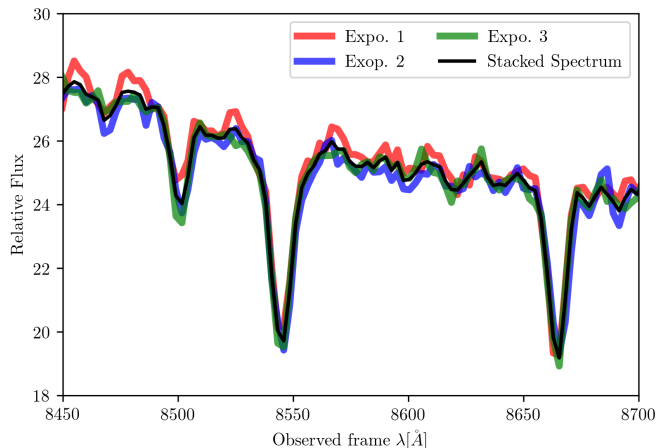


Figure 2.2.: Individual and stacked reduced spectra for one example target. Red, green, and blue show the spectra for the three individual exposures. In black we show the final stacked spectrum. No broadening is observed.

2.3 Analysis

In this section, we describe our analysis of the VIMOS data to obtain the line-of-sight (LOS) velocities from the spectra. We discuss our method for disentangling the GCs from background and foreground objects.

2.3.1 Radial velocity measurements

The radial velocity measurements of GCs were calculated using the python-implemented penalised-PiXel fitting (pPXF) method of [Cappellari & Emsellem \(2004\)](#) and [Cappellari \(2017\)](#). pPXF is a full-spectrum fitting technique that generates a model spectrum by convolving a set of weighted stellar templates to the parametric LOS velocity distribution

2. Kinematical characterisation of globular clusters in the Fornax galaxy cluster

(LSOVD), modelled as a Gauss-Hermite series. The intrinsic velocity dispersion of GCs (usually $\sim 20 \text{ km s}^{-1}$) is well below the spectral resolution of the VIMOS grism we used ($\sim 88 \text{ km s}^{-1}$). Our initial test of deriving the radial velocities shows that the velocity dispersion we obtained is always lower than 20 km s^{-1} (i.e. in most cases, pPXF gives a value of zero if the velocity dispersion is not resolved), which is an expected value for most of the GCs. We derived the mean velocity from pPXF and used the velocity dispersion value as a limiting criterion to select GCs.

For the stellar templates, we used the single stellar population spectra from the extended medium-resolution INT Library of Empirical spectra (E-MILES [Vazdekis et al. 2010, 2016](#)), covering a wavelength range of 1680 to 50000 Å. We preferred this stellar library because it provides us flexibility in obtaining the stellar spectrum on a grid of ages ranging from 8 to 14 Gyr and metallicities in the range $-2.27 < [M/H] < +0.04$ dex. We used an MW-like double power law (bimodal) initial mass function with a mass slope of 1.30. With these settings, we obtained a set of 84 stellar templates from the E-MILES library at a spectral resolution of 2.51 Å. We convolved the stellar library with a Gaussian filter of standard deviation $\sigma = 12 \text{ Å}$ to bring it to the same resolution as the VIMOS spectra.

For the spectral fitting, we used a wavelength region of 4800-8800 Å. This wavelength region covers the major absorption line features, such as H β (4862 Å), Mg β (5176 Å), NaD (5895 Å), H α (6564 Å), and CaT lines (at 8498, 8548, 8662 Å). We masked several regions to avoid residual sky lines or telluric lines.

pPXF requires starting values of the velocity moment parameter; in our case, its radial velocity and velocity dispersion. pPXF uses the given redshift of an object to make this initial guess (see [Cappellari 2017](#)). For the velocity dispersion, we chose a value of 0 km/s, which is expected for a GC (i.e. its internal velocity dispersion is not resolved). For the Fornax cluster redshift, the initial radial velocity was chosen to be $\sim 1375 \text{ km s}^{-1}$, which is close to the radial velocity of Fornax central galaxy NGC 1399, which is 1425 km s^{-1} (taken from [Graham et al. 1998](#)). However, pPXF does not produce a meaningful fit with this guess in the case of foreground stars or background galaxies. Moreover, GC in the outer halo of NGC 1399 or in the intra-cluster regions of the Fornax cluster can have radial velocities different from the initial guess by about $\pm 500 \text{ km s}^{-1}$. Therefore it is crucial to test how the pPXF initial velocity guess can affect the resulting radial velocities, especially for GCs lying in the intra-cluster regions. To determine this, we measured the radial velocities of different GCs belonging to the intra-cluster regions as a function of different initial velocity guesses, as shown in figure A.1. We found that the change in the resulting radial velocities is within 5%, and this variation is within the measured velocity error. This shows that the initial guess of pPXF does not affect our radial velocity measurements. We present this test in detail in Appendix A.1.

pPXF allows the use of additive and multiplicative Legendre polynomials to adjust the continuum shape in the spectral calibration. As a first guess, we used a third and fifth order for additive and multiplicative polynomials, respectively. However, when we obtained a radial velocity consistent with the Fornax cluster but a velocity dispersion higher than 20 km s^{-1} , we varied the polynomials such that we were able to obtain a velocity dispersion lower than

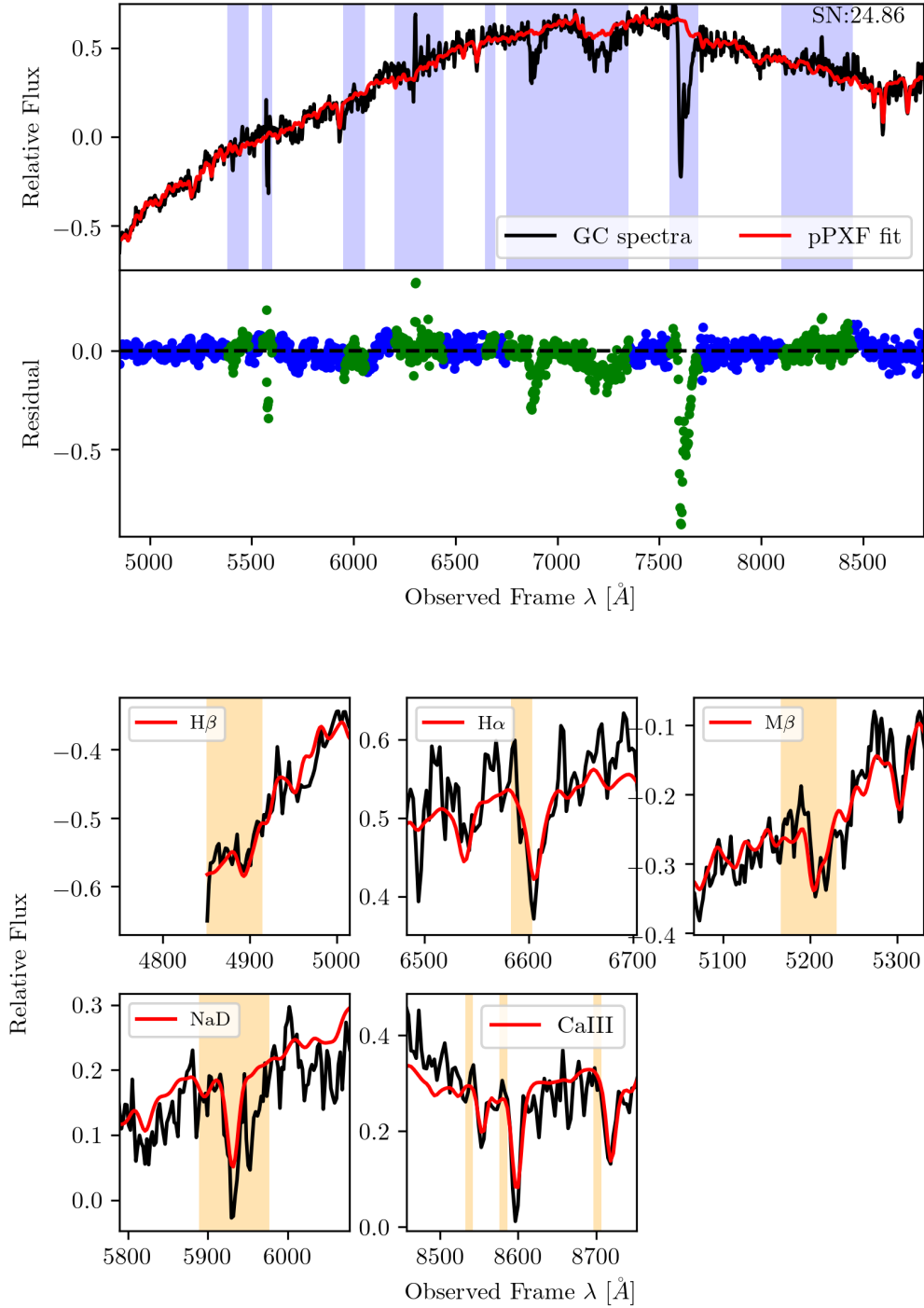


Figure 2.3.: Examples of pPXF fits to two GC spectra with different S/Ns. In the top left panel, red and black show the pPXF fit and a GC spectrum with $S/N \sim 25$. Masked regions are shown as blue bands. Blue and green dots in the lower subpanel show the residuals for unmasked and masked regions, respectively. The top right panel shows a zoom-in view for the absorption features of $H\beta$, $Mg\beta$, NaD , $H\alpha$, and the CaT lines. Orange bands in the subpanels show the expected position of absorption features at the Fornax cluster redshift.

2. Kinematical characterisation of globular clusters in the Fornax galaxy cluster

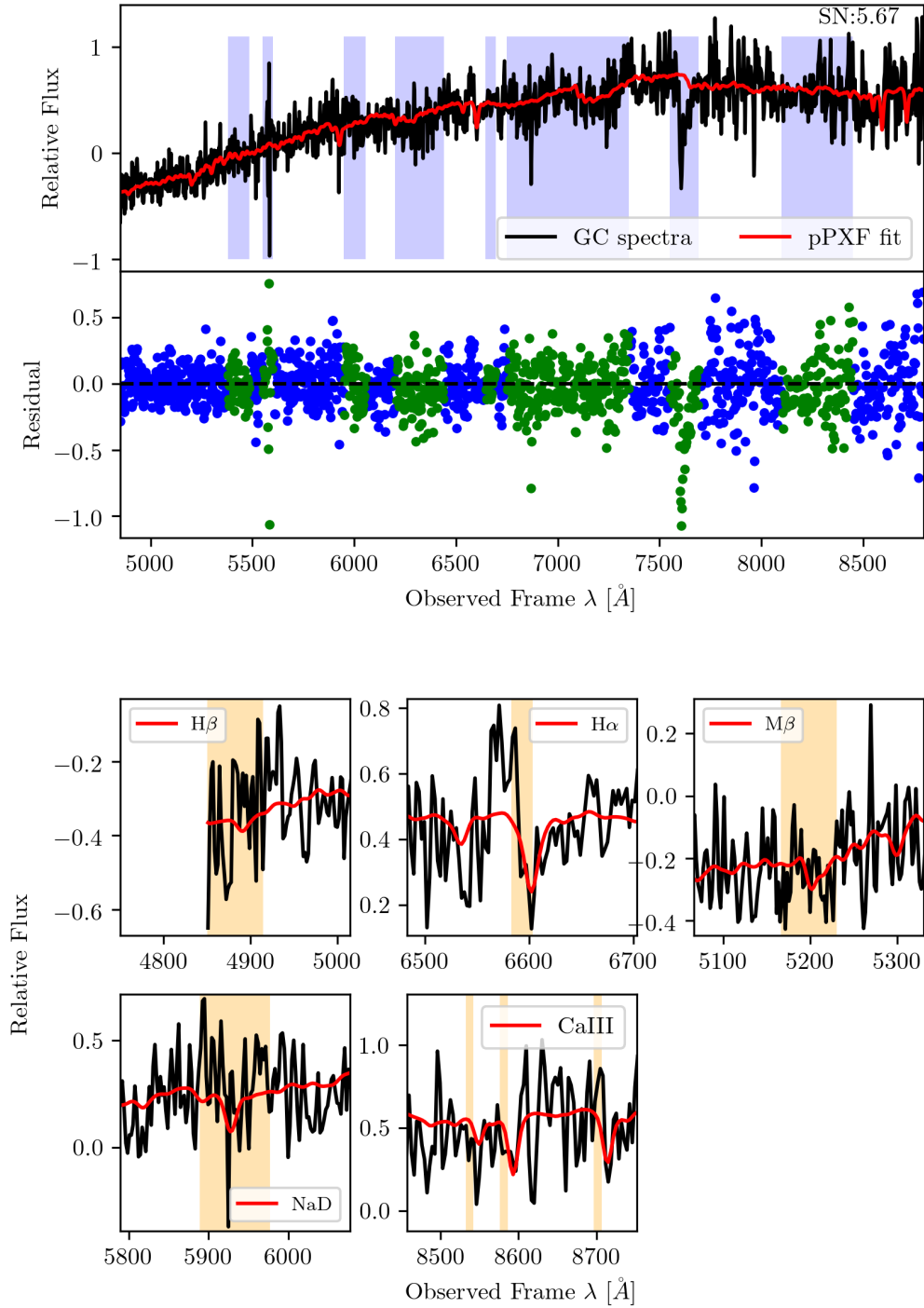


Figure 2.4.: Same as figure 2.4, but for a GCs spectrum with S/N ~ 6 .

20 km s^{-1} . We performed a quantitative analysis to determine how varying polynomials in pPXF can affect the derived mean velocities and dispersions. We performed a test as follows: We defined a grid of additive and multiplicative polynomials in the range from 0 to 6. For each pair of polynomials, we derived the mean velocity and dispersion. First, we ensured that the velocity dispersion was lower than 20 km s^{-1} and the variation in the mean velocity did not exceed 5% for different pairs of polynomials. Based on these two conditions, we selected the most suitable value of these polynomials. We also verified the effect of higher-order polynomials on the derived radial velocity and that of not using multiplicative polynomials. We found that in all cases, there are only subtle variations in the derived radial velocities; they are all consistent within 5%. We present more details of these tests of varying the order of polynomials in Appendix A.1.

Figure 2.4 shows examples of pPXF fits for two GC spectra with different S/Ns. Masked regions are shown in the upper left panels as blue bands, and residuals from the masked regions are plotted in green in the panels below. The right panels show zoomed-in views of individual absorption line features of the GC spectra. Uncertainties on the mean velocity were estimated through Monte Carlo (MC) realisations of the GC spectrum. For each pPXF model fit, we generated 100 realisations of spectra by adding Gaussian noise equivalent to the root mean square (RMS) of the residuals of the best fit. pPXF also returns the weights of template stars that were used to obtain the best fit. To save computational time, we used only template stars with non-zero weights (around ~ 7 -10) to perform the MC realisations.

2.3.2 Selecting Fornax cluster members

Our VIMOS dataset is contaminated by foreground stars and background galaxies. To distinguish Fornax cluster GCs from the contaminants, we used the expected radial velocity range of $450 < v < 2500 \text{ km s}^{-1}$ from Schubert et al. (2010) for objects belonging to the Fornax cluster.

We developed a two-step test to separate the GCs from the background galaxies and stars: First, we searched for emission lines in all spectra. In the case of multiple strong emission lines in a spectrum, we classified that object as a background galaxy. Second, the remaining spectra were fitted with an initial velocity guess of zero, and if pPXF returned a velocity lower than 450 km s^{-1} , we classified the object as a star. All the remaining spectra were fitted as mentioned in section 2.3.1. In this way, we rejected most of the contaminants at the very beginning, before deriving final radial velocity measurements.

To select the final bonafide GCs, we visually inspected the pPXF results for all remaining spectra. To do this, we created a portfolio of each object with its 1D spectrum, pPXF fit with zoomed-in views of major absorption features such as $\text{H}\beta$, $\text{Mg}\beta$, NaD , $\text{H}\alpha$, and CaT lines and a 2D image of the source, with attributes such as the S/N and radial velocity. One example of such a portfolio is shown in Appendix A.2. Based on these portfolios, we further classified the objects into three quality classes: Class A objects, for which all the above-mentioned absorption features are clearly visible. Class B objects that clearly show CaT and $\text{H}\alpha$ absorption features, but MgB and $\text{H}\beta$ are rarely recognisable. Class C objects,

2. Kinematical characterisation of globular clusters in the Fornax galaxy cluster

for which Fornax cluster radial velocities can be obtained, but hardly any absorption features are visible, although their colours are consistent with being GCs.

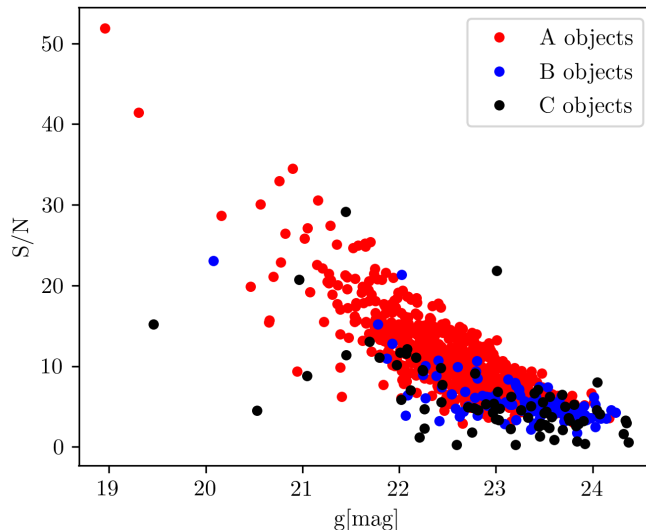


Figure 2.5.: Signal-to-noise ratio vs. g-magnitude for the three classes of objects, as shown in the legend.

Figure 2.5 shows the S/N versus g-magnitude plot for A, B, and C class objects in red, blue and black, respectively. As expected, almost all the class A and B objects have $S/N > 3$, whereas class C objects are mostly fainter and have a lower S/N on average. Only a few C class objects have $S/N > 10$, but their absorption features were contaminated by sky lines. We only considered class A and B objects for our kinematic analysis, but we included the class C objects in our catalogue. As the last step, we applied the heliocentric correction to all the bona fide selected GC radial velocities based on the header information of their observation date.

2.4 Results

A total of 4574 slits were defined in the 25 VIMOS pointings. About 2400 of them were allocated to GC candidates and compact objects, ~ 800 slits to background galaxies, and ~ 1000 slits to stars (Pota et al., 2018). In our analysis, the Esoreflex pipeline extracted 5131 spectra from the VIMOS data (some slits contained more than one object), and our radial velocity analysis resulted in detecting about 920 possible Fornax cluster GCs. For the remaining spectra, about 1000 are classified as background galaxies, and approximately 700 objects revealed velocities of foreground stars. About 2500 spectra were of poor spectral quality. They either had extremely low S/N or were affected by strong residual telluric and skyline features.

We analysed the possible GC spectra in detail. After visual inspection of the pPXF fits (section 3.3), we classified 839 spectra as class A and B objects, and 77 were classified as

class C objects. After accounting for duplicate objects, we obtained 777 unique GC radial velocity measurements for class A and B objects.

In appendix A.3 we present an excerpt of our VIMOS GCs catalogue, including all A, B, and C class objects. Despite the radial velocity, the catalogue contains its error and S/N of the spectrum and also the photometric information in the u , g , r , and i bands from the FDS (Cantiello et al., 2020). The full catalogue is available online. In the following subsections, we present our results, which are based on the new GC catalogue.

2.4.1 Duplicate measurements

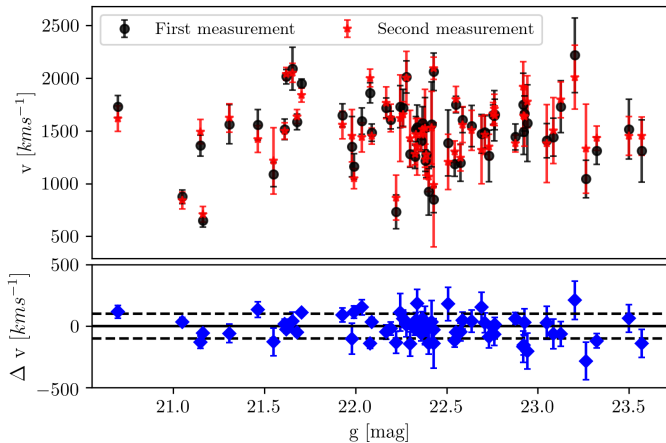


Figure 2.6.: Velocity comparison of duplicate measurements. Red stars and black dots show the radial velocity from two different measurements of the same object as a function of g magnitude. The bottom panel shows the velocity difference between the two measurements. The solid and dashed lines are drawn at $\Delta v = 0$ and $\pm 100 \text{ km s}^{-1}$, respectively.

We used the radial velocity measurements of the same objects that were observed in different VIMOS masks as a measure to verify the robustness of the derived radial velocities and as an estimate for the errors. In figure 2.6 we show the radial velocity measurements and their differences for 62 duplicate targets as a function of g magnitude. The root mean square of the velocity difference is 104 km s^{-1} , and the median offset is -11 km s^{-1} . When an object has a velocity difference of more than 3σ of the corresponding uncertainty on the individual measurements, we take the velocity of the higher S/N spectrum; otherwise, we take the error-weighted average velocity of two spectra.

2.4.2 Comparison with previous measurements

Several previous studies have probed the GC systems in the Fornax cluster. Schubert et al. (2010) presented a catalogue of 700 GCs from observations with VLT-FORS2 and Gemini-GMOS. Bergond et al. (2007) measured the kinematics of 61 GCs in the intra-cluster space of the cluster based on FLAMES observations. Other studies (e.g. Firth et al., 2007; Chilingarian et al., 2011) have targeted and analysed the most massive compact stellar objects around NGC 1399. These literature velocity measurements of GCs provide us another way to verify and confirm the reliability of our derived radial velocity analysis.

Comparing our sample with Pota et al. (2018), we obtained a match for 369 objects. Out

2. Kinematical characterisation of globular clusters in the Fornax galaxy cluster

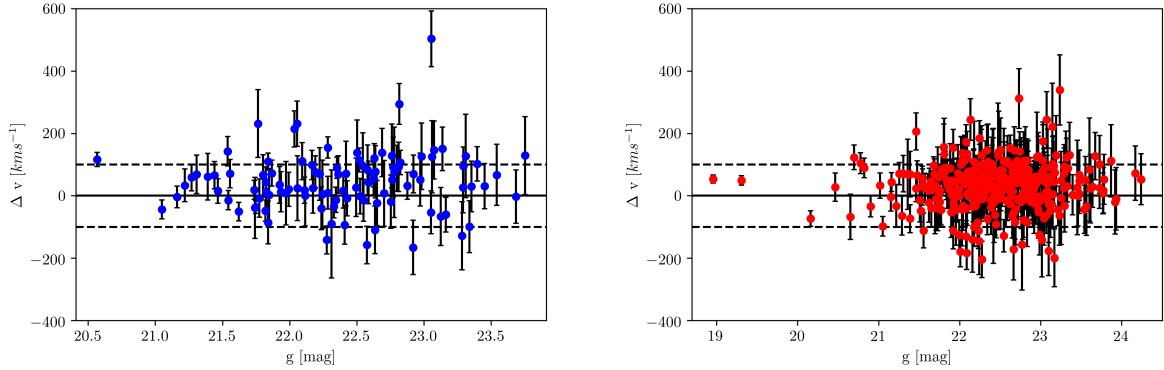


Figure 2.7.: Velocity measurement comparison with the GC sample of [Schubert et al. \(2010\)](#) (left panel, blue dots) and that of [Pota et al. \(2018\)](#) (right panel, red dots) as a function of g magnitude. The solid and dashed lines are drawn at $\Delta v = 0$ and $\pm 100 \text{ km s}^{-1}$, respectively.

Table 2.1.: Matched number of objects from this study to previous studies, rms scatter and median offset of the comparison (our work–previous work).

Previous Study	Matches	RMS (km s^{-1})	Median offset (km s^{-1})
Pota et al. (2018)	369	72	32
Schubert et al. (2010)	104	80	43
Mieske et al. (2002)	13	102	-38
Drinkwater et al. (2000)	10	171	9
Hilker et al. (2007)	1	38	38
Kissler-Patig et al. (1999)	10	125	-69
Mieske et al. (2008)	5	38	-3
Bergond et al. (2007)	18	59	21
Firth et al. (2007)	11	68	33
Hilker & Puzia (priv.comm.)	20	84	36
Chilingarian et al. (2011)	4	34	2

of these, 22 objects were found to have a velocity difference of more than 3σ . Excluding the outliers, the RMS of the velocity difference is 72 km s^{-1} and the median offset 32 km s^{-1} . Here, the median offset is defined as the median of the velocity difference distribution between our GC radial velocities minus the matched literature GC velocities.

With the GC sample of [Schubert et al. \(2010\)](#), we obtained a match for 103 objects, of which only 5 were found to have a velocity difference of more than 3σ . Excluding these 5 outliers, we obtain an RMS of 80 km s^{-1} and median offset of 43 km s^{-1} . We visually inspected all the outliers in both samples and found that our fits to the spectra look very reliable. We therefore neglected the previous measurements of [Pota et al. \(2018\)](#) and [Schubert et al. \(2010\)](#) for the outliers. In figure 2.7 we show the velocity differences to both samples.

Finally, we compared our velocity catalogue with all other available literature studies. Table 2.1 summarises the number of matched objects with our velocity catalogue objects. Figure 2.8 shows the velocity comparison between velocities measured in this work and from

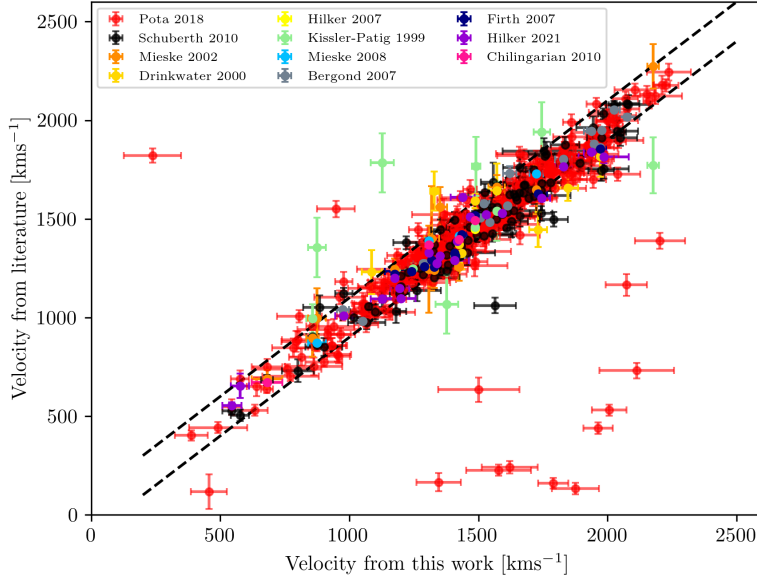


Figure 2.8.: Radial velocity comparison with previous measurements. The two dashed lines are drawn at $\pm 100 \text{ km s}^{-1}$.

the previously available catalogues. We speculate that the measured mean velocity offsets between our and literature datasets might just be due to systematics in the zero points of the wavelength calibration, as it is common in multi-slit spectroscopy. All offsets are minor and within the overall velocity scatter, and we therefore did not attempt to correct for them.

2.4.3 Photometric properties

To obtain the photometric properties of our GC sample, we matched it with the photometric *ugri* and *gri* catalogues presented by Cantiello et al. (2020). We obtained a photometric match for 700 and 770 objects with the *ugri* and *gri* catalogues, respectively. To separate our GC sample into blue and red GCs, we followed the procedure used by Angora et al. (2019) and Cantiello et al. (2020), namely Gaussian mixture modelling (GMM) implemented through the python library *sklearn* (Pedregosa et al., 2012). We fitted a bimodal Gaussian distribution to the GC populations in the $u - r$ and $g - i$ colour-colour diagrams.

Figure 2.9 shows the projected distributions of the bivariate Gaussian (and their components for blue and red GCs) on the $g - i$ and $u - r$ colour axes. A linear fit between the intersection of blue and red Gaussians for $g - i$ and $u - r$ was used to divide the GCs into the respective samples. Table 2.2 shows the results of our GMM. Out of 770 objects, our sample has 56% blue and 44% red GCs, as judged from the photometrically complete *gri* sample.

2. Kinematical characterisation of globular clusters in the Fornax galaxy cluster

Table 2.2.: Bivariate Gaussian parameters using GMM.

	Blue		Red	
Parameter	$g - i$	$u - r$	$g - i$	$u - r$
μ	0.876	1.872	1.104	2.427
σ	0.009	0.034	0.016	0.074

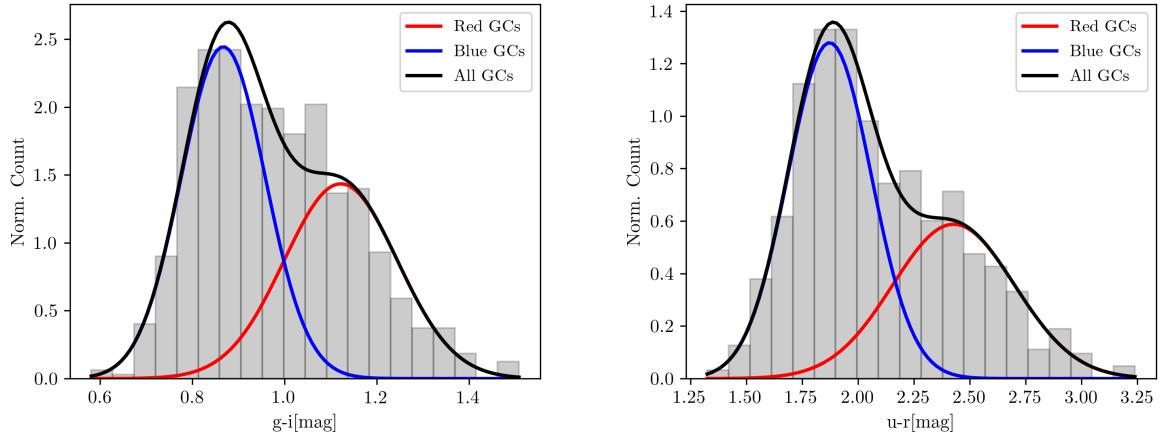


Figure 2.9.: Results of GMM. Left panel: Histogram and colour bimodality of the GCs in $g - i$ colour distribution. Blue and red Gaussian curves are obtained from the GMM and represent the blue and red GC populations. Right panel: Same as left panel, but for the $u - r$ colour distribution.

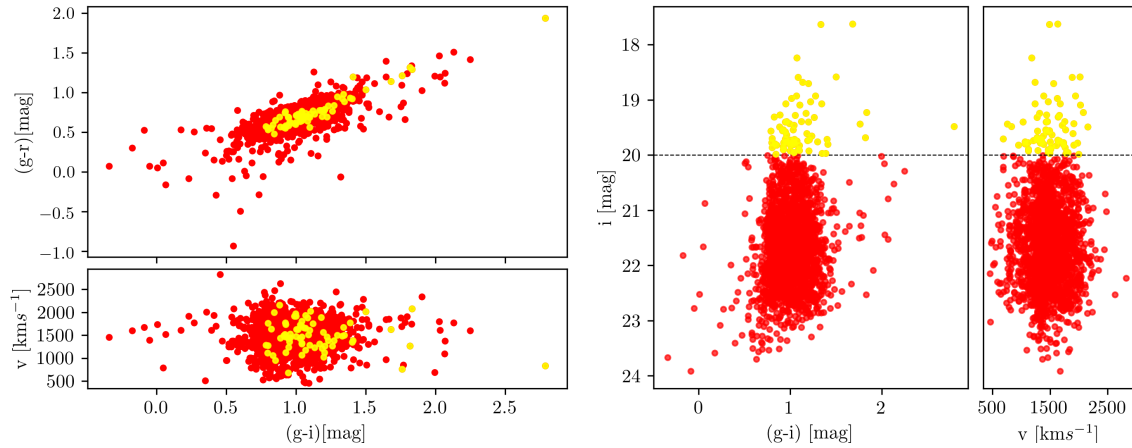


Figure 2.10.: Distribution of GCs (red dots) and UCDs (yellow dots) in the colour-colour and colour-magnitude diagram. Left panel: Distribution of GCs in the $(g - r)$ vs $(g - i)$ space. The lower subplot shows the radial velocity as a function of $(g - i)$ colour. Right panel: Same as right panel, but in i mag vs. $(g - i)$ space.

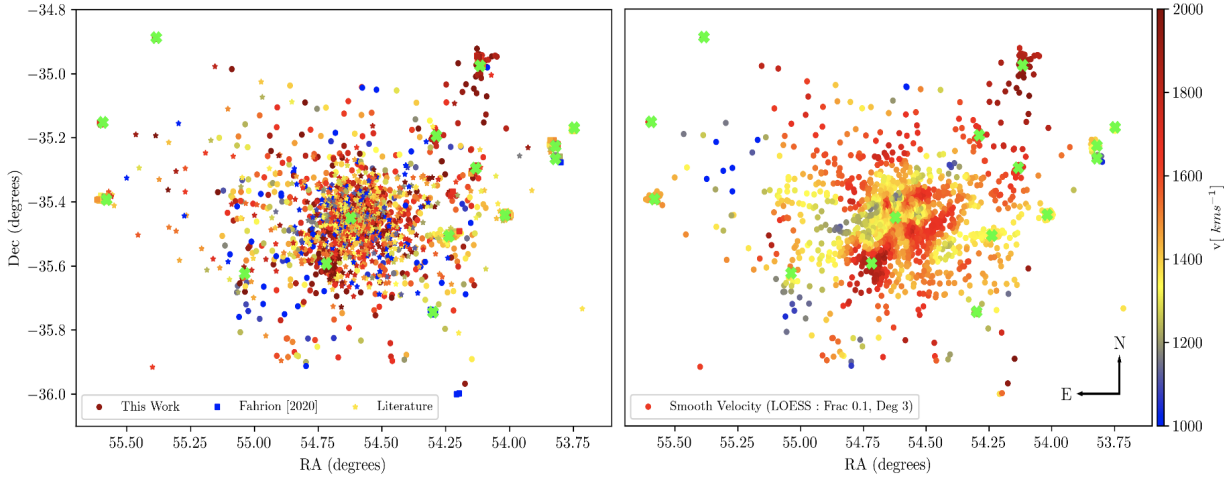


Figure 2.11.: Radial velocity map of GCs within 1.5 square degrees of the Fornax cluster. Major galaxies are shown with green crosses. Left panel: GCs from this work are shown as dots. Squares and stars show GCs from [Fabrion et al. \(2020a\)](#) and previous literature measurements, respectively. Right panel: Smooth velocity map using the LOESS technique. The smoothing parameters are given in the legend of the plot.

2.4.4 Radial velocity map

Combining our radial velocity measurements with previous literature measurements and the recent catalogue presented by [Fabrion et al. \(2020a\)](#) brings the total number of confirmed GCs in the Fornax cluster to 2341 objects. The catalogue of [Fabrion et al. \(2020a\)](#) is based on integral-field observations of the Fornax3D project (F3D, [Sarzi et al. 2018](#)) and provides the GC velocities in the inner regions of 32 Fornax cluster galaxies, many of them located in the cluster outskirts, and thus not shown in figure 2.11, which displays the radial velocity of GCs from our sample within 1.5 square degrees.

The combined sample of GCs provides a representative probe of the whole GC system in the core of Fornax. The GC distribution in the innermost one square degree around NGC 1399 is very uniform and geometrically complete. It amounts to more than 50% of our total GC sample. To better visualize and identify patterns in the velocity distribution, we smoothed the radial velocity with the locally weighted regression method LOESS ([Cleveland & Devlin, 1988](#)). We implemented it with the python version developed by [Cappellari et al. \(2013\)](#). LOESS tries to estimate the mean pattern by averaging the data into smaller bins. Normally, a linear or quadratic order polynomial is used in the LOESS technique. In our sample, some of the GCs in the phase-space distribution were utterly isolated. Using a lower-order polynomial could cause over-smoothing of distinct kinematic features. To prevent this, we used a third-order polynomial and a low value of the smoothing factor of 0.1 ([Cleveland, 1979](#); [Cleveland & Devlin, 1988](#)). The LOESS-smoothed radial velocity map is shown in the right panel of figure 2.11.

To search for any rotational signature in the GC system, we modelled the GC kinematics with a simple model that describes the rotational amplitude and velocity dispersion, similar to [Fabrion et al. \(2020a\)](#) (see their section 4.2.1). To have a homogeneous phase-space

2. Kinematical characterisation of globular clusters in the Fornax galaxy cluster

distribution of GCs, we considered GCs within 30 arcminutes from the central galaxy NGC 1399. In figure 2.12 we show the rotational amplitude and measured velocity dispersion for the full sample as well as red and blue GCs. We find a low rotational velocity of lower than 30 km s^{-1} for the full sample and the blue GCs. Red GCs show a significant rotational velocity of 60 km s^{-1} with a rotation axis of $\text{PA}=70^\circ$ (measured north over east). The rotation axis for the entire sample is close to the axis of red GCs and is certainly dominated by them.

In figure 2.20 we show the rotation axis (black line) of the red GCs. For the red GCs, the ratio of V_{rot}/σ is 0.22, meaning a low but significant rotational signature, similar to that of other massive galaxies. Only a few studies have examined the kinematics of the stellar body of NGC 1399; for example, [Saglia et al. \(2000\)](#) used longslit observations to obtain the stellar kinematics out to $1.6'$ of NGC 1399, giving a value of stellar $V_{rot}/\sigma \sim 0.11$. This low rotation measure is consistent with the almost round shape of NGC 1399 ($\varepsilon = 0.1$), characterising this galaxy as a slow rotator. The central stellar kinematics of NGC 1399 cannot

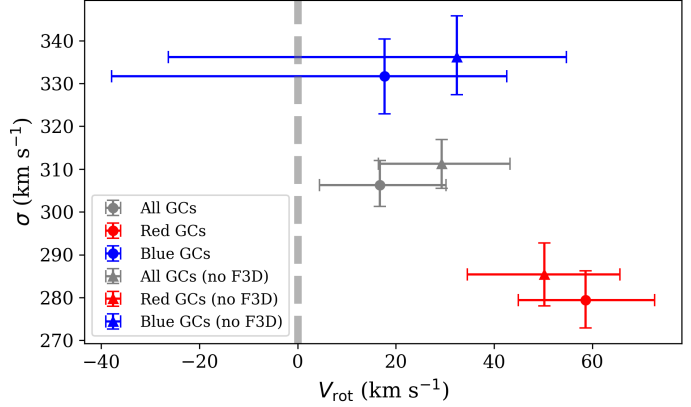


Figure 2.12.: Rotational velocity of all, red and blue GCs within 30 arcminutes. We modelled the full sample as well as a restricted sample, excluding the F3D GCs from [Fahrion et al. \(2020a\)](#) as most F3D GCs are bound to their respective host galaxies.

be straightforwardly compared to the outer GC kinematics and rotation. They most probably reflect the formation of the central stellar spheroid through violent relaxation of early mergers. The photometric PA of the major axis of NGC 1399 is $\sim 112^\circ$ degrees (within $1'$) and varies between 90 - 110° at outer radii (up to $20'$) ([Iodice et al., 2016](#)), which is more or less consistent with the east-west elongation of the extended GC system. More measurements of the outer stellar kinematics around NGC 1399 are needed to understand whether the GCs and stellar halo components are kinematically coupled or decoupled.

Previously, [Schuberth et al. \(2010\)](#) studied the rotation of GCs around NGC 1399 and found a rotation amplitude of $61 \pm 35 \text{ km/s}$ for the red GCs and 110 - 126 km/s for the blue GCs. In contrast to [Schuberth et al. \(2010\)](#), we did not find a strong rotational signature for the blue GCs. This might be due to our large and uniform sample of GCs, whereas the [Schuberth et al. \(2010\)](#) sample was limited to 10 arcminutes and was geometrically not complete.

We also note different patches of low- ($<1000 \text{ km s}^{-1}$) and high-velocity regions ($>1700 \text{ km s}^{-1}$), elongated in east to west and north-east to south-west structures. We discuss the correlations between the photometric and kinematical properties of the GCs in the subsequent discussion section.

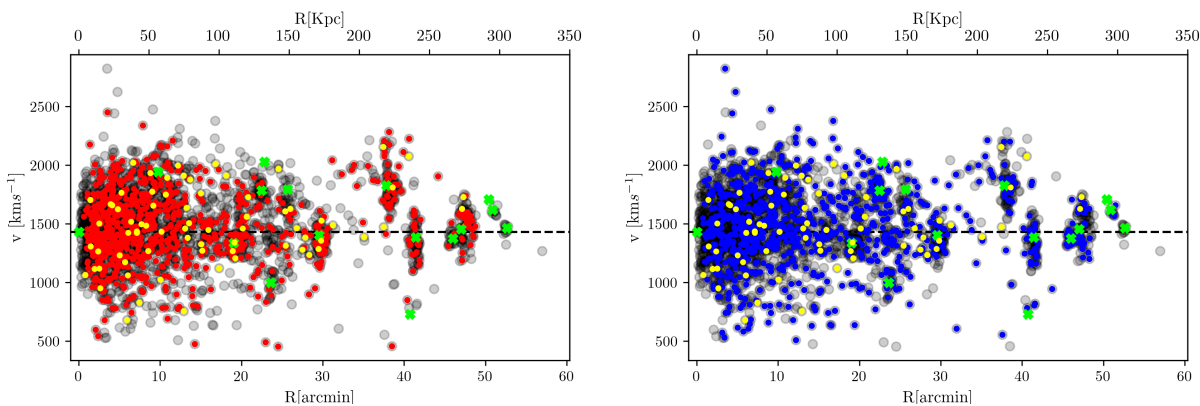


Figure 2.13.: Phase-space diagrams of radial velocity vs. cluster-centric distance. In both panels the grey dots show the full sample, the green crosses major galaxies within 300 kpc, and the dashed horizontal lines mark the systemic velocity of NGC 1399. Left panel: Velocity distribution for red GCs. Right panel: Same for blue GCs. Yellow dots indicate UCDs, and the green crosses mark the major galaxies of the Fornax cluster.

2.5 Discussion

In this section, we connect the photometrically discovered intra-cluster GCs with the full sample of 2341 confirmed GCs and study their phase-space distribution and radial velocity dispersion profile.

2.5.1 Colours, phase space, and spatial distribution

We studied the properties of red and blue GCs separately. To divide the entire sample of 2341 GCs into red and blue subpopulations, we used the $g-i$ colour distribution because the shallower u -band photometry does not exist for all GCs. We adopted a value of $g-i = 0.978$, obtained from the GMM (fig. 2.9, left panel), to separate the two subpopulations. The brightest compact objects of our catalogue are a mix of genuine massive globular clusters and stripped nuclei, called ultra-compact dwarf galaxies (UCDs) in the literature (Hilker et al., 1999b; Drinkwater et al., 2000, 2003). To select UCDs, we used a magnitude cut of $m_i < 20$ mag (Mieske et al., 2002) and found a total of 72 UCDs. In figure 2.10 we show the distribution of GCs and UCDs in the magnitude, colour ($g-i$ and $g-r$), and velocity spaces.

These plots show that the UCDs are redder than the GCs on average. This confirms the blue tilt of bright GCs and UCDs that was already found in photometric samples of rich GC systems (e.g. Dirsch et al., 2003; Mieske et al., 2010; Fensch et al., 2014). Some very blue and very red GCs exist, with $(g-i) < 0.6$ and $(g-i) > 1.6$, respectively. While the blue GCs might be explained by young to intermediate ages, the very red colours point to either very metal-rich populations, dust obscuration, or blends in the photometry. Future investigations are needed to clarify their nature.

In figure 2.13 we show the radial velocity of red (left panel) and blue (right panel) GCs

2. Kinematical characterisation of globular clusters in the Fornax galaxy cluster

as a function of the cluster-centric distance. Major galaxies around NGC 1399 are shown as green crosses. We observe that most of the red GCs are centrally concentrated on the systematic velocities of these galaxies (taken from [Iodice et al., 2019](#)). Within 50 kpc from NGC 1399, red GCs homogeneously span a range of relative velocities of $\pm 500 \text{ km s}^{-1}$, and farther outside, they follow a wedge-shaped structure to lower relative velocities until 150 kpc. [Schuberth et al. \(2010\)](#) observed the wedge-shaped feature of the red GCs to be confined within 50 kpc (see their Fig. 9, right panel). However, with the current larger sample of GCs, we note that it extends out to larger distances.

The systemic velocities of most major galaxies at cluster-centric distances larger than 160 kpc are similar to that of NGC 1399. An interesting exception at ~ 220 kpc distance is NGC 1380, which has a high systemic velocity of $\sim 1800 \text{ km s}^{-1}$. Red GCs with similarly high velocities are scattered out to ± 50 kpc galactocentric distances in filamentary structures around this galaxy, possibly suggesting a disturbance of its halo. Although most red GCs are concentrated around major galaxies, a noteworthy number of red GCs appears not to be related to any particular galaxy. These are candidates of intra-cluster GCs.

In contrast to red GCs, blue GCs show a more complex and irregular pattern in the phase-space diagram. In particular, between 60-150 kpc, they extend to higher relative velocities and fill the intra-cluster regions between the galaxies. In addition, blue GCs occupy the outer halos of the major galaxies.

Our UCD sample shows a radial velocity distribution between $750\text{-}2500 \text{ km s}^{-1}$, with a mean velocity close to the radial velocity of NGC 1399, with a velocity scatter of 312 km s^{-1} , consistent with the fainter GCs. A few red and blue GCs exist at low radial velocities of $\sim 500 \text{ km s}^{-1}$ at cluster-centric distances between 10-220 kpc. This was reported before for the blue GCs by [Richtler et al. \(2004\)](#). Due to their high relative velocity with respect to the Fornax cluster, exceeding 800 km s^{-1} , they might constitute unbound GCs from galaxy encounters with highly radial orbits in the LOS, or a sheet of foreground intra-space GCs.

2.5.2 Velocity dispersion profile

The large spatial coverage of our sample enables us to measure the velocity dispersion profile of the GCs out to 300 kpc. To do this, we defined circular bins such that each bin had 100 GCs, and measured the velocity dispersion as the standard deviation of radial velocities in that bin. The uncertainty on the velocity dispersion was determined through a bootstrap technique. In each bin, we measured the velocity dispersion 1000 times and took its scatter as the uncertainty. For the total sample, we obtained 23 bins, where the outermost bin has only 41 GCs. We followed the same procedure for red and blue GCs separately. This resulted in 10 and 20 bins, respectively.

In figure 2.14 we show the velocity dispersion profile of our GC sample. The black line indicates the dispersion measurement for the full sample, and the grey band denotes its 1σ uncertainty. Blue and red dots indicate the values for the blue and red GCs. The dashed vertical grey lines show the projected cluster-centric distances of NGC 1404 and other major galaxies. For reference and comparison, we included the velocity dispersion measurements

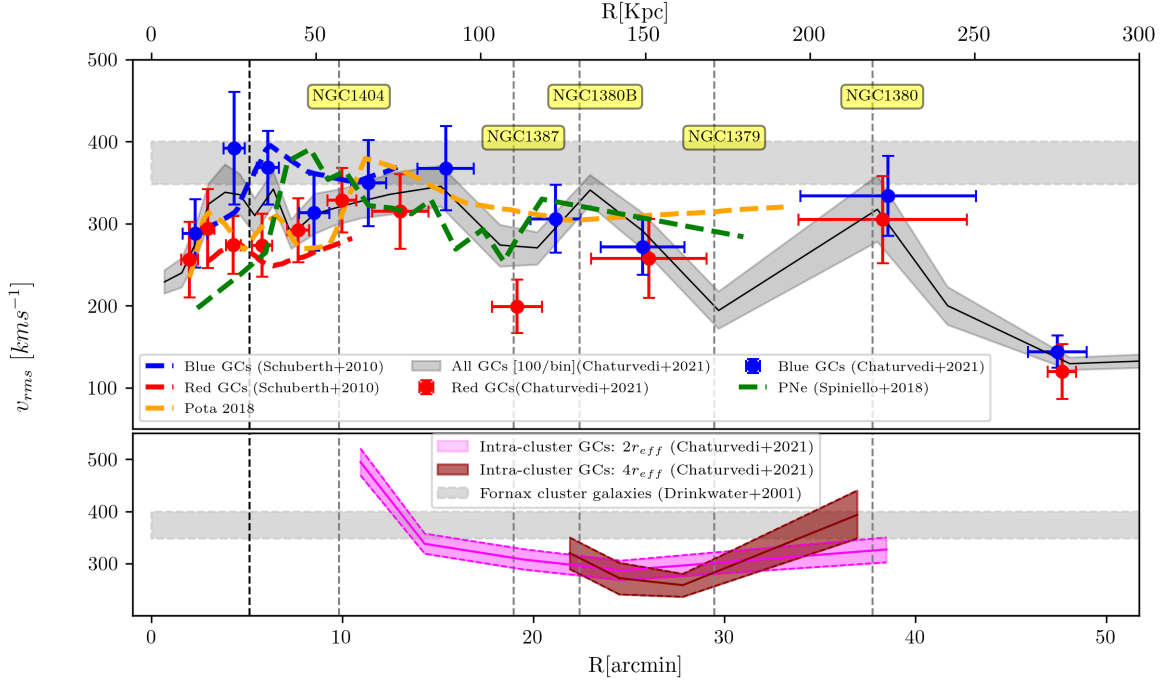


Figure 2.14.: Velocity dispersion profiles in the Fornax cluster core region as a function of projected distance from NGC 1399. Upper panel: Black line denotes the dispersion profile of the complete sample of 2341 GCs. The grey band marks the 1σ uncertainty. Red and blue dots represent the values for the red and blue GCs, with 100 GCs per bin. The dashed blue and red lines represent the dispersion profiles for the GC analysis of the [Schuberth et al. \(2010\)](#) data. The dashed green and orange lines show the PNe and GC dispersion profiles from [Spiniello et al. \(2018\)](#) and [Pota et al. \(2018\)](#), respectively. The horizontal band denotes the velocity dispersion of the Fornax cluster galaxies ([Drinkwater et al., 2000](#)). The dashed vertical black line marks the effective radius of NGC 1399 and the dashed vertical grey lines the projected distances of major galaxies (as labelled) from NGC 1399. Lower panel: Dispersion profile of ICGC candidates with two different selections. The pink line shows ICGCs and outer halo GCs selected farther than $2r_{\text{eff}}$ away from major galaxies, and the light pink band represents the 1σ uncertainty. The dark red line represents ICGCs that were selected outside $4r_{\text{eff}}$ around major galaxies (see text for details), and the lighter red band denotes its 1σ uncertainty.

from previous studies as well, as indicated in the legend and caption.

We also measured the velocity dispersion profile of potential ICGCs within the Fornax core region, shown as a magenta line in the lower panel of figure 2.14, with the light pink band indicating its 1σ uncertainty. The selection of the ICGCs was made by excluding GCs around major galaxies by performing cuts in the phase-space distribution. First, we calculated the scatter in the radial velocities of GCs within two effective radii (r_{eff}) of each galaxy, (taken from [Iodice et al., 2019](#)). We used $\pm 2\sigma$ of this velocity scatter around the galaxy LOS velocity as the lower and upper boundary to select the GCs belonging to each galaxy. The remaining GCs were classified as ICGC candidates, being aware of the fact that this selection might include outer halo GCs that are probably still bound to their parent halos (see below).

2. Kinematical characterisation of globular clusters in the Fornax galaxy cluster

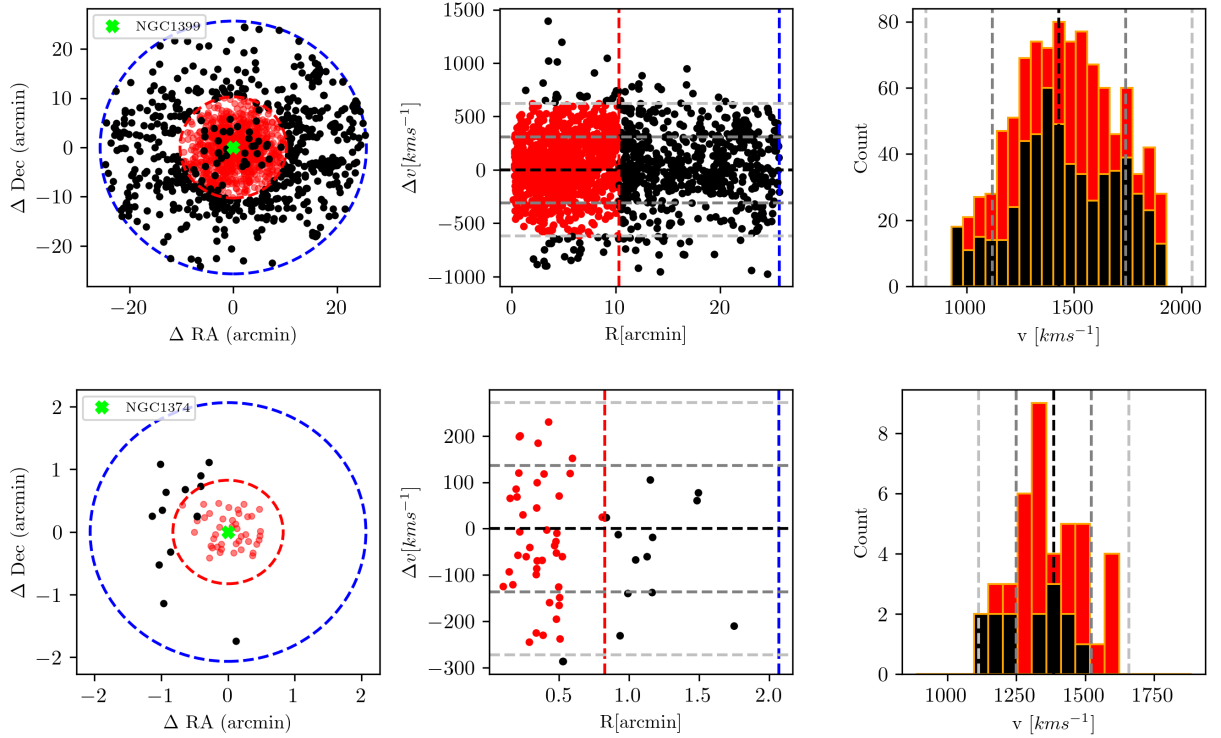


Figure 2.15.: Selection of potential ICGCs around NGC 1399 (first row) and NGC 1374 (second row). Left panel: GC distribution within $5r_{\text{eff}}$ (dashed blue circle). The radius of $2r_{\text{eff}}$ is indicated as a dashed red circle. Middle panel: Distribution of GCs in projected phase space. Red dots show the galactic GCs within $2r_{\text{eff}}$, and black dots show the defined ICGCs. Dashed vertical red and blue lines indicate $2r_{\text{eff}}$ and $5r_{\text{eff}}$, and the grey horizontal lines give the 1 and 2σ scatter of GC velocities within $2r_{\text{eff}}$ around the systemic velocity of NGC 1374. Right panel: Velocity histograms of ICGCs (black) and galactic GCs (red). The dashed black line marks the LOS velocity of NGC 1374, and the dashed grey lines show the 1 and 2σ scatter of GC radial velocities, as also shown in the middle panel.

Figure 2.15 shows examples of the ICGC candidate selection for the central galaxy NGC 1399 and the galaxy NGC 1374. For the central galaxy, we clearly see a fraction of GCs with high relative velocities lying inside $2r_{\text{eff}}$, which are identified as the ICGCs. The true central concentration of ICGCs is difficult to access because they might overlap in radial velocity with GCs of the central galaxy. We note that our ICGC selection criteria only provide a rough separation between GCs bound to individual galaxies and those belonging to an unbound or at least disturbed intra-cluster population. Bound GCs might reach out to larger effective radii, but true ICGCs might also be projected at similar velocities in front or behind a galaxy and thus are hidden from detection. Only a detailed dynamical analysis of the mass profile around each galaxy can provide a cleaner sample of ICGCs. This is beyond the scope of this paper.

According to our selection criteria, 719 GCs, almost 31% of the total sample, are classified as ICGCs. This number is probably an upper limit of true ICGCs due to the above-mentioned limitations of our selection criteria. Moreover, the geometrical incompleteness of GC velocities within $2-4 r_{\text{eff}}$ around the major galaxies plays a role. Whereas the central regions are covered

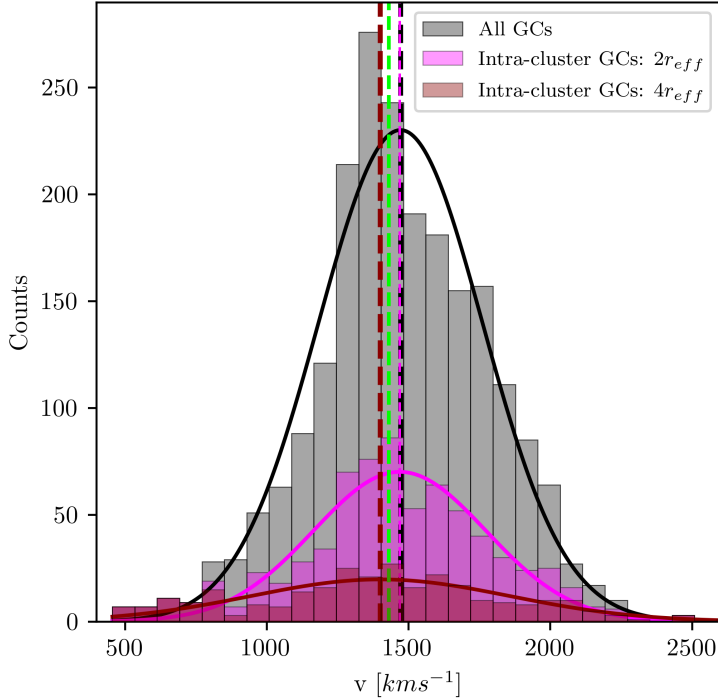


Figure 2.16.: Radial velocity histograms of the full sample and the intra-cluster GCs. The dashed vertical green line indicates the radial velocity of NGC 1399. The dashed vertical black, magenta, and dark red lines indicate the mean velocities of fitted Gaussian to the three sets of GCs.

by MUSE observations and thus the GC counts are complete (Fahrion et al., 2020a) there, the outer halo regions are not fully covered by the VIMOS pointings, as can be seen in the uneven distribution of outer GCs around NGC 1374 (fig. 2.15, left panel).

To produce a cleaner ICGC sample, we performed a similar selection as mentioned above, but with a phase-space cut at $>4r_{\text{eff}}$. This left us with a sample of only 286 ICGCs (12% of the total sample). The velocity dispersion profile of this set of GCs is shown as the dark red band in the lower panel of figure 2.14. Figure 2.16 shows the velocity distribution of the full and ICGC samples. For all three samples, the mean velocity lies close to the radial velocity of NGC 1399. The velocity scatter of the full sample and ICGCs, selected at $2r_{\text{eff}}$, is close to 300 km s^{-1} , whereas ICGCs selected outside $4r_{\text{eff}}$ show a larger velocity scatter of 455 km s^{-1} around a mean velocity of 1400 km s^{-1} .

In the following, we describe the features and irregularities noted in the velocity dispersion profiles, starting from the centre outwards.

1) Between 2 and 5 arcminutes, the dispersion profile takes a steep rise from 220 to 350 km s^{-1} within $1r_{\text{eff}}$ of NGC 1399. Mostly blue GCs contribute to this rise. This is consistent with the rise previously reported by Schubert et al. (2010). Red GCs show a constant velocity dispersion of $\sim 270 \text{ km s}^{-1}$ within $1r_{\text{eff}}$ of NGC 1399, in agreement with

2. Kinematical characterisation of globular clusters in the Fornax galaxy cluster

Schuberth et al. (2010) and Pota et al. (2018).

2) Between 5 and 10 arcminutes, the total dispersion profile flattens around a value of $\sim 300 \text{ km s}^{-1}$. While the dispersion profile of the blue GCs decreases, the profile of the red GCs rises. This rise is caused by the superposition of the GCs of NGC 1404, which has a high systemic velocity of 1944 km s^{-1} . Within these radii limits, Spiniello et al. (2018) have also reported a similar increase in the PNe velocity dispersion profile. The lower velocity dispersion of red GCs from Schuberth et al. (2010) can be explained by the increase in the sample size in our study, which added several GCs with more extreme velocities. For the ICGC velocity dispersion profile, we observe a value of $\sim 500 \text{ km s}^{-1}$ at 8 arcmin. This is artificial and caused by the exclusion of GCs within $2 r_{\text{eff}}$ of NGC 1399. Thus, we are left with GCs with extreme radial velocities, resulting in the high dispersion value.

3) Beyond 10 arcminutes, the dispersion profile remains flat around $\sim 300 \text{ km s}^{-1}$ until 18 arcmin, consistent with the results of Pota et al. (2018). Farther out, the GCs belonging to individual galaxies dominate the velocity dispersion values of all GCs and cause large variations from <200 to $>300 \text{ km s}^{-1}$. After a steep decrease from 500 to 300 km s^{-1} , the velocity dispersion profile of ICGCs behaves more smoothly with nearly constant values around 290 km s^{-1} out to 40 arcmin. This value is relatively consistent with the velocity dispersion of cluster galaxies (Drinkwater et al. (2000)). A similar trend with PNe kinematics has been observed by Spiniello et al. (2018) out to 30 arcmin.

Iodice et al. (2016), using the g -band light distribution around NGC 1399, identified a physical break radius at 10 arcmin, separating the total light profile into a central spheroidal light of NGC 1399 and an outer exponential halo. The constant value and flattening of the ICGC dispersion profile beyond 12 arcmin kinematically confirms this physical break radius.

2.5.3 Globular clusters and planetary nebulae

Spiniello et al. (2018) presented the kinematics of 1452 PNe out to 200 kpc in the Fornax cluster core, spatially extending the results presented in McNeil et al. (2010). Although the velocity dispersion profile of PNe overall follows the kinematics behaviour of the red GCs, slight differences in the profiles can be found. In figure 2.14, the green dashed line shows the velocity dispersion profile of PNe taken from Spiniello et al. (2018). Within 5 arcminutes, the velocity measurements we obtained for the red GCs show a slightly higher value than the PNe (this was true also in Spiniello et al. (2018), but the difference between the velocity dispersion values was smaller). Between 5-10 arcminutes, the PNe show a high dispersion peak value at $\sim 380 \text{ km s}^{-1}$, unlike our red GCs, and better match the value we measured for blue GCs. Between 10-20 arcmin, the velocity dispersion for both PNe and red GCs, decreases, with the red GCs showing a very low value at the projected distance of NGC 1387. Beyond 20 arcmin, the PNe velocity dispersion shows a flat behaviour at $\sim 300 \text{ km s}^{-1}$, slightly above that of blue and red GCs.

In general, the PNe velocity dispersion profile closely follows that of all GCs beyond 10 arcmin, rather than that of red or blue GCs individually. This might suggest that PNe trace the behaviour of both stellar populations, that of galaxies as well as that of intra-cluster

light.

2.5.4 Intracluster GC kinematics

The first photometric wide-field search for GCs in the Fornax cluster by [Bassino et al. \(2006\)](#) reported an ICGC populations based on GC overdensities in regions between the central galaxy NGC 1399 and neighbouring galaxies. Later, [Bergond et al. \(2007\)](#) and [Schuberth et al. \(2008\)](#) kinematically identified and quantified the properties of some ICGCs. Through the FDS survey, [D’Abrusco et al. \(2016\)](#) reported the discovery of an extended GC density distribution in the Fornax core region with several well-defined overdense regions, and [Iodice et al. \(2016\)](#) discovered a faint stellar bridge coinciding with the GC over density between NGC 1399 and NGC 1387, confirming the interaction between these two galaxies.

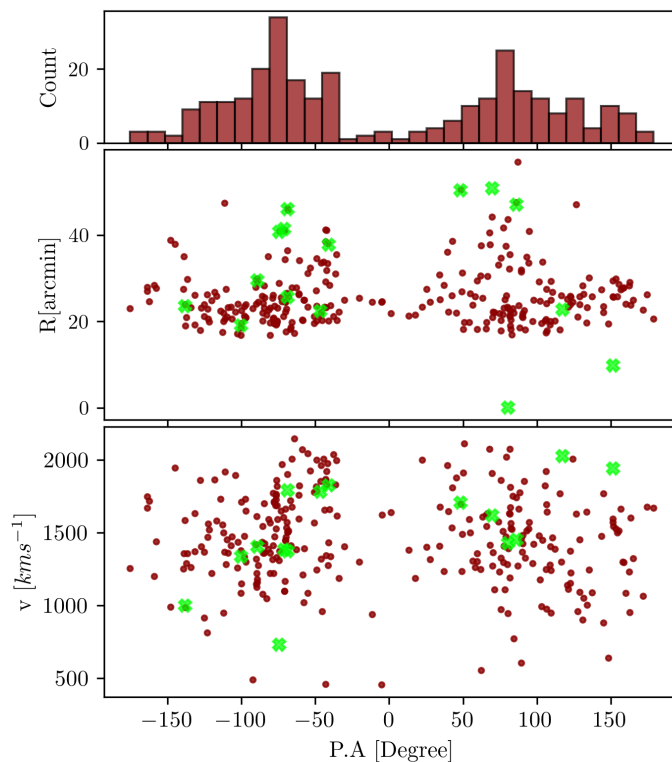


Figure 2.17.: Azimuthal distribution of ICGCs selected outside $4r_{\text{eff}}$ radii around major galaxies (see text for details). Top panel: Histogram of the ICGC position angle (PA), with a bin size of 30° . Middle panel: Cluster-centric distance vs PA. Bottom panel: Radial velocity vs PA. Green crosses indicate major galaxies.

Our extended and spatially homogeneous GC catalogue allows us to study the kinematical properties of the enhanced density regions of GCs in Fornax. In fig. 2.20 we plot our full GC radial velocity sample on top of a smoothed density distribution of photometric GC

2. Kinematical characterisation of globular clusters in the Fornax galaxy cluster

Table 2.3.: 2D KS test and properties of the ICGCs.

Intra-cluster region (1)	p-value (2)	Median velocity [km s ⁻¹] (3)	Velocity scatter [km s ⁻¹] (4)	Blue to red GCs ratio (5)
Reg A	0.37	1419	200	1.17
Reg C	0.72	1559	303	1.92
Reg F	0.84	1477	312	1.56
Reg G	0.66	1352	291	1.51
Stream A	0.48	1375	127	0.87
Stream A 2 nd peak	–	1723	56	–
Stream C	0.20	1384	117	2.03
Stream C 2 nd peak	–	1824	128	–
Stream F	0.98	1452	228	1.15
Stream G	0.54	1362	166	2.08

Notes: Column 3 and 4 show the mean velocity and velocity scatter of GCs within the respective intra-cluster region.

candidates by [Cantiello et al. \(2020\)](#). To create the smoothed density map, we used the non-parametric kernel density estimates based on python-scikit-learn kernel density routine by [Pedregosa et al. \(2011\)](#). From the FDS catalogue, a density of 0.75 GCs/arcmin² is expected within the central region of the Fornax cluster. To include at least some GCs in the density maps and to create the visual impression of the GCs streams, we adopted a Gaussian kernel bandwidth of 0.015 degrees, which is ~ 1 arcmin. The top, middle, and lower panels show the distribution of all, red, and blue GC candidates, respectively.

Confirming the FDS survey findings of [D’Abrusco et al. \(2016\)](#) and [Cantiello et al. \(2020\)](#), we also observe an elongated distribution of confirmed GCs in the east-west direction, centred on NGC 1399. The radial velocity patterns in the smoothed velocity map in fig. 2.11 show that on the west side of NGC 1399, GCs have a relatively higher radial velocity than on the east side. Further on the east side of NGC 1399, in the overdense G and F features, GCs show an extended filamentary spatial distribution.

The azimuthal distribution of ICGCs selected outside $4r_{\text{eff}}$ of major galaxies is shown in figure 2.17. It highlights the east-west elongation of ICGCs around NGC 1399. In the two lower panels of this figure, where the azimuthal distribution is shown as a function of cluster-centric distance and radial velocity, respectively, phase-space features in between galaxies become apparent. A detailed dynamical analysis of these features is beyond the scope of this paper.

We investigated the spatial correlation between the photometric and our radial velocity catalogue. For this, we performed a 2D Kolmogorov-Smirnov (2D-KS) test ([Peacock, 1983](#)) in the four GC overdensity regions named regions A, C, F, and G following the same naming convention as in [D’Abrusco et al. \(2016\)](#). Fig. 2.19 shows the phase-space distribution of the ICGCs selected with a cut of $>2r_{\text{eff}}$ and indicates the rectangular regions around the GC overdensities. For all the regions, we obtain a p-value higher than 0.20 , which means that the spatial distributions of photometrically selected and confirmed GCs are correlated with a significance higher than 3σ . Figure 2.18 shows the radial velocity histograms of ICGCs falling within these four overdense regions. The mean velocities are ~ 1450 km s⁻¹, which is close to the radial velocity of NGC 1399 and the Fornax cluster itself. This suggests that the GCs in these regions are ICGCs that are kinematically affected by the Fornax cluster potential. In table 2.3 we list the p-values obtained from the 2D-KS tests for all regions and the fitted Gaussian mean and velocity scatter. These selected rectangular regions are populated by both red and blue GC populations, but the blue GCs dominate in numbers on average. In contrast to this, GCs within the $2r_{\text{eff}}$ radii of galaxies show a higher fraction of red GCs on average. We list the number ratio of blue to red GCs in table 2.3.

With the small sample size of ICGCs, and given the caveats of the rough ICGC selection criteria mentioned in Sect. 2.5.2, it is hard to speculate about the nature of the GCs in the overdense regions. Figure 2.19 shows quite clearly that our spectroscopic sample provides kinematical information about the visible photometric streams in the overdense regions. Our 2D KS test performed for the selected rectangular regions demonstrates that our spectroscopic sample is statistically coherent with the photometric sample. To obtain an indication about the possible progenitor galaxies of ICGCs and their physical properties, specifically those

2. Kinematical characterisation of globular clusters in the Fornax galaxy cluster

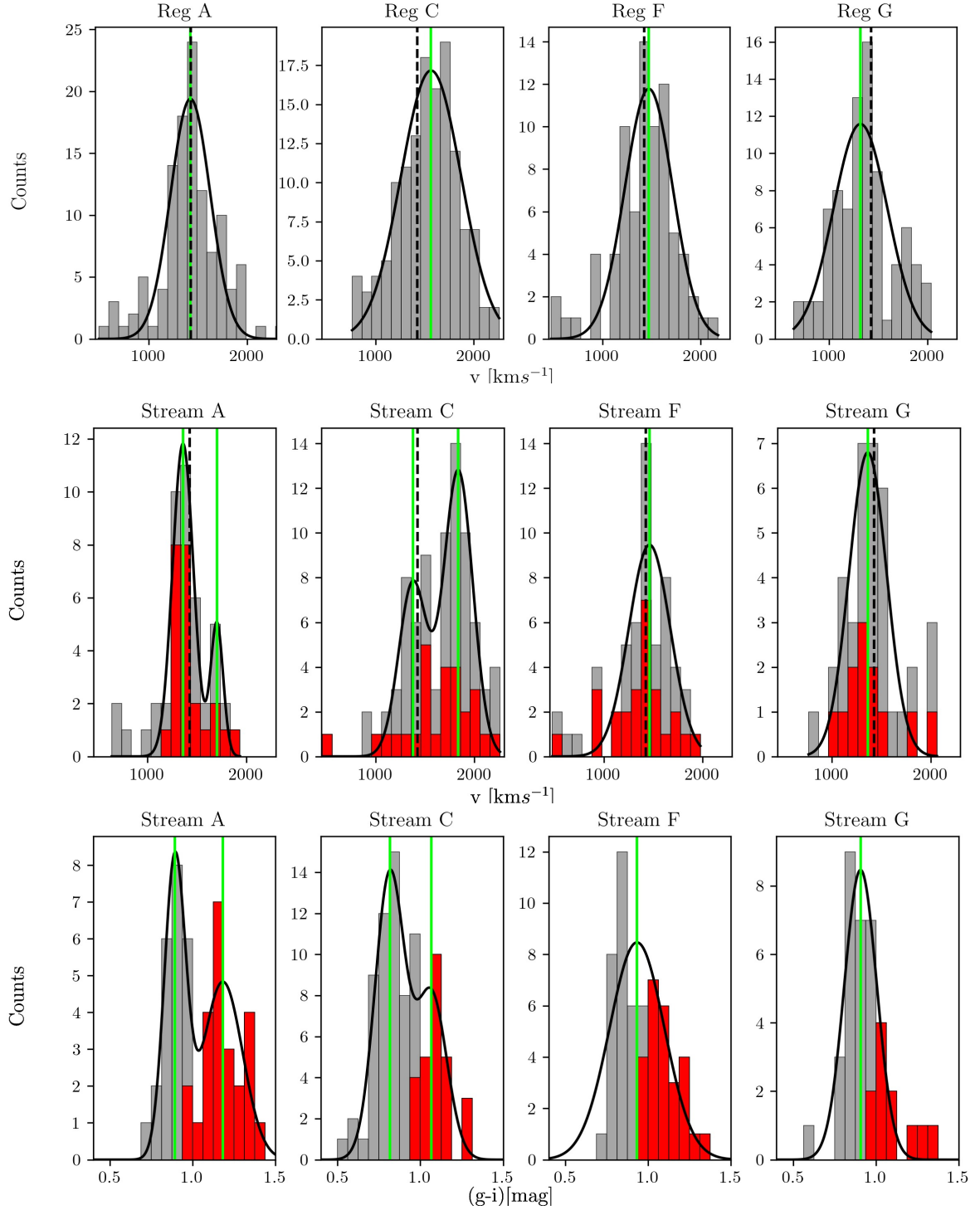


Figure 2.18.: Radial velocity and $g - i$ colour histograms of the intra-cluster regions. Top panel: Radial velocity of GCs lying within the rectangular boxes A, C, F, and G (left to right). Middle panel: Radial velocity of GCs lying within the streams A, C, F, and G (left to right). The radial velocities of the red GCs are marked in red. Bottom panel: $g - i$ colour histogram of GCs lying within the streams A, C, F, and G (left to right). The dashed vertical black line marks the radial velocity of NGC 1399, and the vertical green lines show the peak positions of the fitted Gaussians. For streams A and C, double Gaussians were fitted.

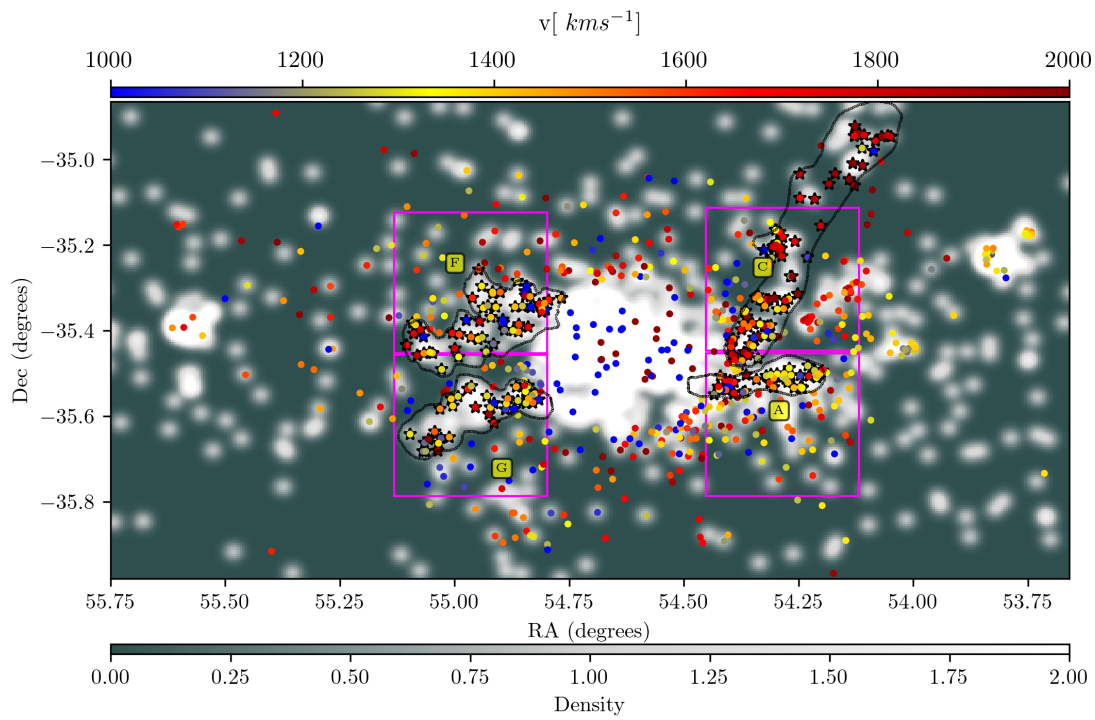


Figure 2.19.: Distribution of ICGCs selected with a phase-space cut at $>2r_{\text{eff}}$. GC overdensity regions are named as in [D’Abrusco et al. \(2016\)](#). The magenta boxes show the regions in which we perform 2D KS tests. Black contours show the visibly selected regions to study the stream properties.

2. Kinematical characterisation of globular clusters in the Fornax galaxy cluster

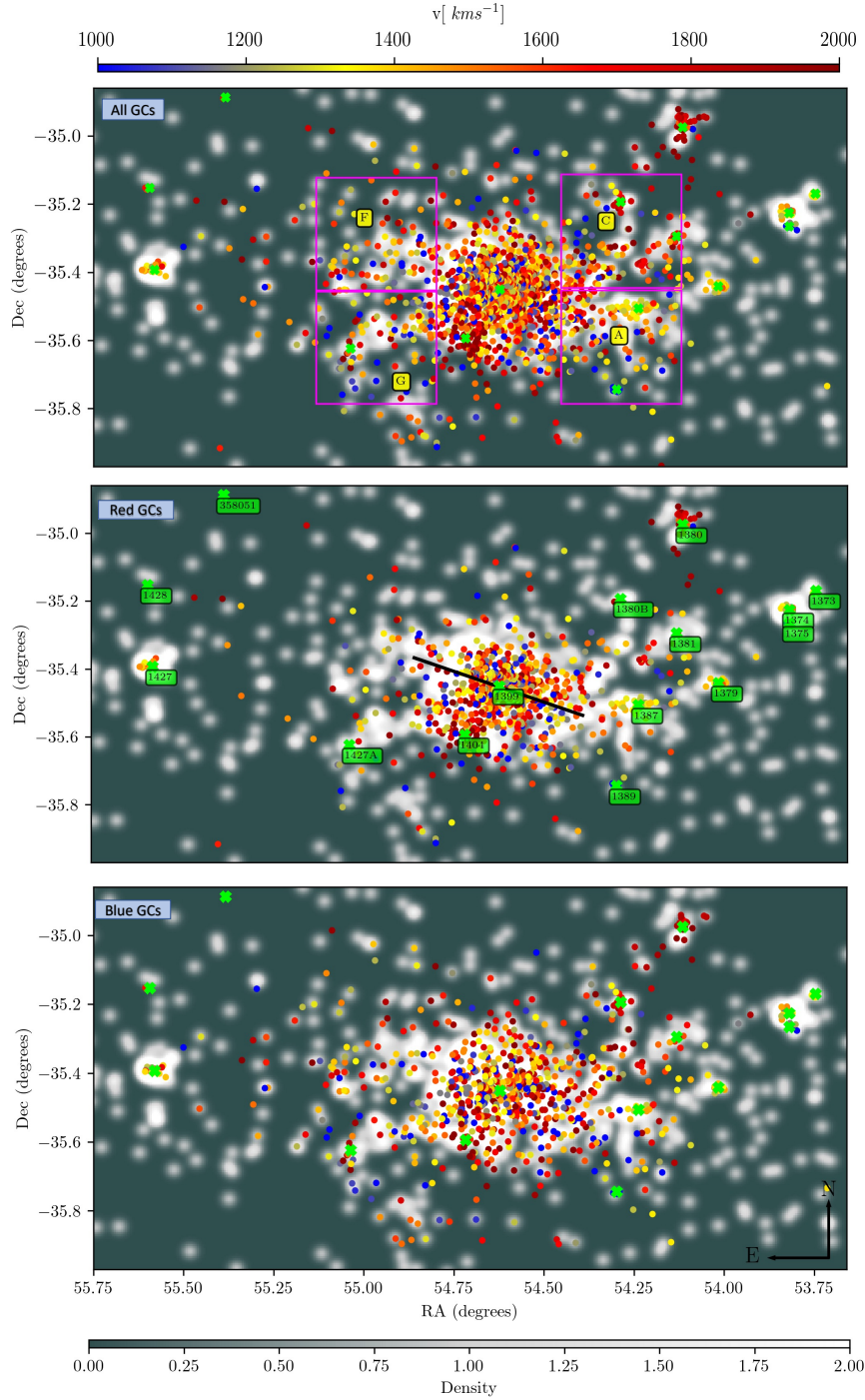


Figure 2.20.: Globular clusters with confirmed radial velocities (coloured dots) plotted over the surface density map of photometric GC candidates from the FDS (Cantiello et al., 2020). Top panel: Full GC radial velocity sample. Middle panel: Radial velocity distribution of red GCs. The black line shows the rotation axis of the red GCs at $\text{PA}=70^\circ$, measured north to east. Major galaxies are labelled in green. Bottom panel: Same for blue GCs. The density scale plotted at the bottom represents the number of GCs from the photometric sample per square arcminute.

that trace the visible streams (marked in figure 2.19 with the black contours), we plot the radial velocity and $g - i$ colour histograms in figure 2.18. We call these streams A, C, F, and G. In the following, we explain the features we detected within these streams.

Stream A is a feature related to the faint stellar bridge reported by [Iodice et al. \(2016\)](#), connecting NGC 1387 and NGC 1399 (region A). In this stream, the GC radial velocity distribution shows two peaks, one close to the radial velocity of the central galaxy NGC 1399 (at 1374 km s^{-1}), and the other at 1723 km s^{-1} . Both peaks show a low-velocity scatter with values of 127 km s^{-1} and 56 km s^{-1} , respectively. The second peak might arise from GCs on the east side of NGC 1387, which is interacting with NGC 1399. These GCs might be tidally stripped off the halo of NGC 1387. In the radial velocity histograms, we mark the contribution of red GCs in red. We note that red GCs mostly contribute to the first radial velocity peak, whereas the blue GCs dominate the second peak. This suggests that tidally stripped GCs, those that are outside the systemic Fornax cluster velocity, are mostly blue. In the $g - i$ colour histogram of stream A (bottom panel of fig. 2.18), we also observe two peaks, suggesting the presence of red as well as blue GCs. Studying the GC colour distributions of early-type galaxies in the Virgo cluster, [Peng et al. \(2006\)](#) have shown that luminous galaxies ($M_B \sim -21 \text{ mag}$) mostly have bimodal GC colour distributions, whereas low-luminosity galaxies ($M_B \sim -16$) have dominant fractions of blue GCs. In stream A, we see a bimodality in the $g - i$ colour histogram with a larger fraction of red GCs. Comparison of this type of bimodality with results of [Peng et al. \(2006\)](#) suggests that GCs in stream A are mostly generated by the interaction of the luminous galaxy NGC 1387 and NGC 1399.

Stream C in the overdense region C consists of a chain of GCs in the vicinity of NGC 1380 and NGC 1380B. [Cantiello et al. \(2020\)](#) pointed out that this GC overdensity could result from the LOS projection of adjacent GC systems. The GCs in the vicinity of NGC 1380 and NGC 1380B (but beyond $2r_{\text{eff}}$ radii) have radial velocities higher than 1700 km s^{-1} , consistent with the systemic velocities of both galaxies. In the GC radial velocity histogram of stream C we also observe two peaks, one close to the radial velocity of NGC 1380, and the other close to the NGC 1399 radial velocity. Similar to stream A, stream C GCs also show a bimodal $g - i$ colour histogram, with a higher fraction of the blue GC population, although the bimodality is not as clear due to the small sample size. In stream C, both radial velocity peaks are dominated by blue GCs with radial velocity scatters of $\sim 110 \text{ km s}^{-1}$. In stream C, both radial velocity peaks are dominated by the blue GCs with radial velocity scatters of around 110 km/s . In stream C, blue GCs are almost twice as abundant than red GCs. As shown in the studies of [Peng et al. \(2006\)](#), an asymmetrical distribution of GCs, with an inclination towards blue GCs, suggests that the GCs in stream C are generated by galaxies in the magnitude range $-20 < M_B < -19 \text{ mag}$.

In stream F, GCs show a radial velocity distribution in between $700\text{-}1800 \text{ km s}^{-1}$ with a mean velocity and scatter of 1452 km s^{-1} and 228 km s^{-1} , respectively. We find an equal fraction of blue to red GCs in stream F.

Stream G harbours GCs in the velocity range $800\text{-}2000 \text{ km s}^{-1}$, with a peak velocity close to the systemic velocity of Fornax and is mostly dominated by the blue GCs. These GCs comprise a kinematically coherent group, and in the $g - i$ colour histogram, we observe a peak

2. Kinematical characterisation of globular clusters in the Fornax galaxy cluster

towards blue GCs, suggesting that the progenitors of GCs in stream G are low-luminosity galaxies (Peng et al., 2006).

We also note that in the south-east of NGC 1404, next to the G feature, some GCs show radial velocities higher than 1700 km s^{-1} , similar to the systemic velocity of NGC 1404. As previously shown by Bekki et al. (2003) and more recently shown through X-ray studies by Su et al. (2017), NGC 1404 suffered from tidal interaction with NGC 1399 in the past few gigayears. Thus, tidally released GCs are expected around NGC 1404, and we now might see the kinematical signature of them for the first time. Detailed dynamical models will be necessary to assess which GCs in the overall phase space distribution might have belonged to NGC 1404 in the past.

Furthermore, we note that GCs around NGC 1427A, on the south-west side of NGC 1399, show a stream-like distribution with a gradual decrease in radial velocity from 1500 km s^{-1} north of 1427A to 1100 km s^{-1} south of the galaxy. This kinematic feature might suggest that NGC 1427A is moving in the south-north direction, losing its GCs during its cruise through the core of the Fornax cluster (e.g. Lee-Waddell et al., 2018b).

Finally, we searched for the spatial distribution and numbers of red and blue GC subpopulations in the overdense regions. Figure 2.20 shows that blue GCs dominate the intra-cluster overdense regions between the Fornax cluster galaxies, whereas red GCs are more concentrated in the galaxies. The dominance of the blue (and thus mostly metal-poor) GCs in the Fornax IC regions and in the visually identified streams suggests that the Fornax IC component results from the accretion of tidally stripped low-mass galaxies. Our results are in accordance with the dominantly blue ICGCs population observed for the Virgo cluster (see Ko et al., 2017; Longobardi et al., 2018b). We list the number ratio of blue to red GCs in each region and the four streams in table 2.3.

2.6 Conclusions

We have reanalysed VLT/VIMOS data of the central one square degree of the Fornax cluster, based on which, we produced radial velocity measurements of 777 GCs that we present in a catalogue. Adding literature data, this provided the largest and spatially most extended compilation of GC radial velocities in the Fornax cluster. This sample was used to kinematically characterise GCs in the core of the cluster. In the following, we highlight the main results of our work.

1) With the improved VIMOS ESO reflex pipeline 3.3.0 and careful analysis of radial velocity measurements with pPXF over the full spectral range, we have doubled the number of GC radial velocity measurements on the same dataset as was previously analysed by Pota et al. (2018). Combined with previously measured values from the literature, we gathered a sample of 2341 GC radial velocities in Fornax.

2) We used the GMM technique to divide the full sample of 2341 GCs into a blue (56%) and a red (44%) GC subpopulation. The phase-space distribution of red GCs shows that most of them are bound to the major cluster galaxies, in particular, the central galaxy

NGC 1399. In contrast, blue GCs are spatially extended and show more irregular kinematics patterns. They occupy the outer haloes of galaxies and the intra-cluster space.

3) Using the radial velocities of GCs, we measured the dispersion profile out to a radius of 300 kpc, covering almost half of the virial radius of the Fornax cluster. Beyond 10 arcmin (~ 58 kpc), the dispersion profile of all GCs flattens. This radius is therefore considered as the break radius separating the potential of NGC 1399 from that of the cluster. This result is strongly confirmed by the dispersion profile of potential ICGCs, which shows a flat behaviour beyond 10 arcmin at a value of 300 ± 50 km s $^{-1}$.

4) The radial velocity map of the full GCs sample kinematically characterises the previously photometrically discovered ICGC population of the Fornax cluster. The different overdense GC regions are marked by streams of higher relative velocity GCs, giving first kinematical evidence of interactions between the central galaxy NGC 1399 and other major galaxies.

5) Finally, we note that mostly blue GCs dominate the intra-cluster regions and trace substructures that connect NGC 1399 to its neighbouring galaxies.

With the goal to study the Fornax cluster mass distribution and assembly history, the GC radial velocity catalogue we present is of unprecedented value for exploring the dynamical structure and evolution of the Fornax cluster and its member galaxies.

3 | Mass-modelling of the BCG NGC 1399

The previous chapter was based on the kinematical characterisation of GCs in the Fornax cluster. We provided the spectroscopic confirmation of the Fornax intra-cluster GCs, showing that Fornax substructures are dominated mainly by the blue (metal-poor) GCs. We produced one of the most extensive radial velocity catalogues of GCs, compiled from the Fornax cluster VLT spectroscopic survey (FVSS) and previous literature velocity measurements. In this chapter, I used this radial velocity catalogue of GCs to perform the mass-modelling of NGC 1399 out to $5 r_{\text{eff}}$. I have investigated the effect of including the intra-cluster GCs that were selected on the basis of spatial segregation and velocity σ -clipping. The content of this chapter is adopted from *Chaturvedi et al. 2023, in prep, A&A*, which will be submitted soon.

3.1 Introduction

Massive early-type galaxies (ETGs) belong to the most luminous and massive systems in the Universe. They usually reside in the centres of galaxy clusters and represent the final stage of galaxy evolution. According to the Λ CDM cosmological structure formation scenario, they are embedded in large dark matter (DM) halos and their growth is proposed to occur in a two-phase scenario. First, an intense burst of star formation forms a central spheroidal component in-situ, and in the second phase the outer parts are assembled ex-situ with the accretion or merger of lower mass galaxies (Oser et al., 2010; van Dokkum & Conroy, 2010).

The entire assembly of the massive DM halo occurs in a hierarchical way through the merging of smaller DM halos (Cooper et al., 2013; Pillepich et al., 2015). The hierarchical formation of ETGs leaves an imprint on their structures and physical properties, leading to the build-up of diffuse stellar light at large scales (Gregg & West, 1998; Montes & Trujillo, 2014; Arnaboldi et al., 2012a; Iodice et al., 2019) and intra-cluster stellar populations such as accreted globular clusters (GCs) in the outskirts of galaxy halos (Harris et al., 2020; Longobardi et al., 2018a; Cantiello et al., 2020; Chaturvedi et al., 2022). This kind of evolution of ETGs makes them essential systems for understanding galaxy evolution and formation at the largest and most massive scales. However, measuring the total mass profile on a large physical scale, particularly of the extended DM halo of ETGs, is pretty challenging. Unlike late-type galaxies, like spirals and dwarf irregulars, ETGs are dominated by old stellar populations. Moreover, the stellar light in the outskirts of the ETGs is very faint, making it difficult to perform a detailed study.

3. Mass-modelling of the BCG NGC 1399

In recent years, with technological advancement, there has been a great interest in comprehending the nature and origin of massive galaxies using the diffuse intra-cluster light (ICL) in groups and clusters of galaxies through observations (Iodice et al., 2016, 2019; Kluge et al., 2020) and cosmological simulations (Cooper et al., 2015; Pillepich et al., 2015; Marini et al., 2022). The ICL is considered an important tracer for measuring the gravitational potential of the system, as it extends out to several 100 kpc, which is similar to the size of DM halos, and thus provides a direct opportunity to understand the mass-assembly and DM content of ETGs (Montes & Trujillo, 2018, 2019; Montes, 2022). However, due to the low surface brightness nature of the ICL (mostly $\mu_g > 29$ mag arcsec²), it is very challenging to obtain spectroscopy and any kinematical information directly. An alternative is to use discrete kinematical tracers such as globular clusters (GCs) and planetary nebulae, which are observable out to tens of effective radii of galaxies.

GCs are bright, compact sources and are excellent kinematic tracers of the galaxy potential. They exist in two types, metal-rich (red) GCs and metal-poor (blue) GCs (Brodie & Strader, 2006). These two classes of GCs show different kinematical properties and spatial distributions. The red GCs follow the stellar light distribution of their host galaxy and have kinematics similar to that of the galaxy's inner spheroid. In contrast, the blue GCs dominate in the outskirts of galaxy halos and have complex kinematics (Schuberth et al., 2008; Coccato et al., 2013; Pota et al., 2018; Chaturvedi et al., 2022; Hughes et al., 2022). The velocity dispersion profiles of the red and blue GCs are also different. The different properties of GCs suggest different origins of the two classes, with the red GCs born in-situ and the blue GCs being accreted from infalling low-mass cluster galaxies (Ashman & Zepf, 1992; Kundu & Whitmore, 2001; Peng et al., 2006). Clearly, these properties are correlated with the two-phase hierarchical formation scenario of galaxy formation (Cooper et al., 2013; Pillepich et al., 2015).

The distinct kinematic behaviour and spatial distribution of the red and blue GCs allow breaking the mass-anisotropy degeneracy, a fundamental challenge of dynamical modelling. In addition, the availability of kinematic tracers out to large physical scales alleviates the degeneracy between dynamical stellar mass-to-light (M/L) ratio and DM mass (Napolitano et al., 2009, 2014; Zhu et al., 2016b; Li et al., 2020). Studying the kinematics of the core of the Hydra I cluster core, Hilker et al. (2018) found that kinematic substructures can boost the line-of-sight velocity dispersion, and thus could influence the mass-modelling results. Other similar works point toward the same picture that ignoring the presence of the substructures in the mass modelling affects the dynamical mass estimates (Old et al., 2017; Tucker et al., 2020).

After the Virgo cluster, the Fornax galaxy cluster (at 20 Mpc distance) is the nearest galaxy cluster and its central galaxy, NGC 1399, is a well studied system that hosts a large number of GCs. It provides an excellent opportunity to investigate the formation and evolution of an early-type galaxy in a dense environment. Previous photometric studies of the Fornax cluster have detected the presence of GC substructures between NGC 1399 and its neighbouring galaxies (D'Abrusco et al., 2016; Iodice et al., 2019; Cantiello et al., 2020), and therefore the Fornax cluster offers the chance to investigate the role of substructures on the mass-modelling.

To understand the mass-assembly of the Fornax cluster, we are conducting the Fornax cluster VLT spectroscopic survey (hereafter FVSS, for details, see [Pota et al., 2018](#); [Spiniello et al., 2018](#); [Chaturvedi et al., 2022](#); [Napolitano et al., 2022](#)) targeting GCs and planetary nebulae in the central 1.5 square degrees. FVSS is a multi-instrument observing campaign using FORS2, VIMOS, MUSE and FLAMES at the ESO VLT. Most recently, [Chaturvedi et al. \(2022\)](#), hereafter FVSS-III, combined the FVSS VLT/VIMOS results with previous GCs velocity measurements mainly from the Fornax 3D survey ([Fahrion et al., 2020a](#)) and [Schubert et al. \(2008\)](#) and produced the largest GCs radial velocity catalogue of more than 2300 GCs in the Fornax cluster. In FVSS-III, we provided the spectroscopic confirmation and kinematical characterization of the GC substructures between the Fornax cluster galaxies. We also showed that the outer halo of NGC 1399 and intra-clusters substructures are dominated mainly by blue GCs. The photometrically detected GC streams in Fornax were also confirmed statistically in phase space using the COSTA algorithm ([Gatto et al., 2020](#)) in [Napolitano et al. \(2022\)](#).

In the present work, we use the kinematics of the GC system around NGC 1399 to obtain the mass profile of the central galaxy out to 200 kpc. We perform a two-component Jeans modelling to reduce the mass-anisotropy degeneracy and obtain constraints on the orbital distribution of GCs. The key goals of this work are a) to obtain a total mass estimate of NGC 1399, b) to investigate the effect of the substructures and intra-cluster GCs on the mass modelling, and c) to gain insight into the orbital distribution of the GCs.

This chapter is organized as follows: In Section 3.2 we present the spatial density and kinematics of the GCs. Section 3.3 briefly introduces the Jeans dynamical modelling and fitting method, and in Section 3.4 we present the results obtained from the modelling work. Lastly, in Section 3.5, we present our summary and conclusion of our work.

3.2 Data

This section presents the observables required for the Jeans modelling work of Section 3.3, including the GCs surface density profiles and kinematics details of the GCs sample. As mentioned in the introduction, we use the GCs radial velocity catalogue presented in FVSS-III and additional literature compilation for the mass-modelling work of NGC 1399. For a detailed description of the data reduction and radial velocity measurements, we refer to paper FVSS-III.

3.2.1 GCs sample for dynamical modelling

One of the primary goals of this paper is to assess the influence of intra-cluster GCs (hereafter ICGCs) on the mass-modelling of NGC 1399. An accurate definition of the intra-cluster population should involve dynamical arguments about how bound a population of test-particles is to the galaxy potential ([Dolag et al., 2010](#)). This would imply to robustly separate the central galaxy potential from the cluster potential and select as bound members the

3. Mass-modelling of the BCG NGC 1399

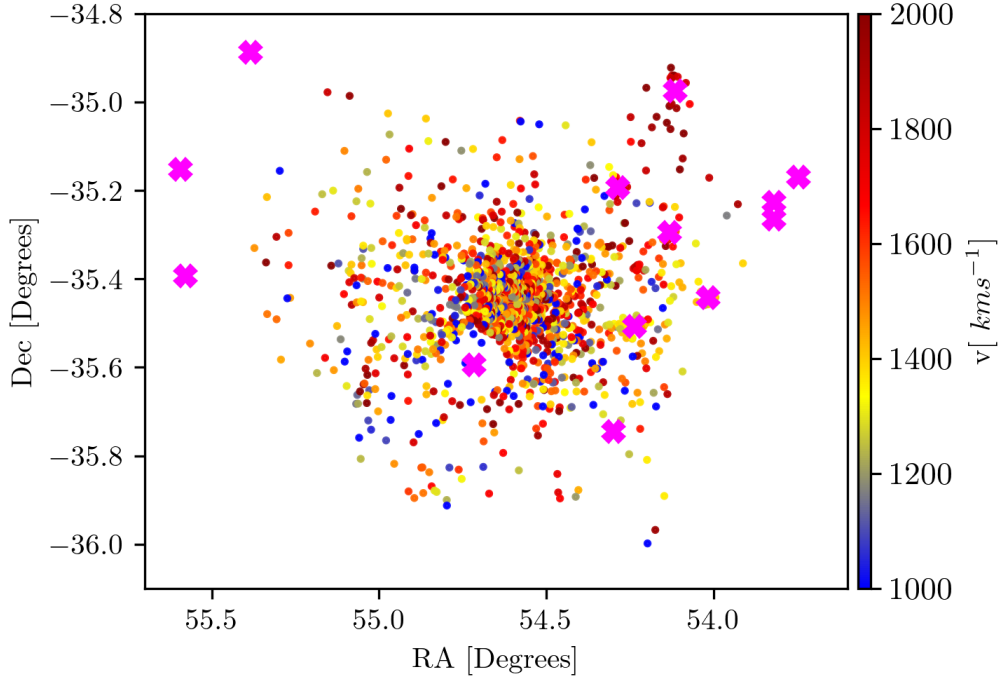


Figure 3.1.: Radial velocity map of GCs of NGC 1399 and the IC sample within 1.5 square degrees of the Fornax cluster. Dots are colour coded according to the GCs line-of-sight velocity. Magenta crosses indicate major Fornax cluster galaxies.

ones that are solidly inside the escape velocity of the central galaxy potential with respect to the cluster potential.

In this work we want to make a first step toward this more compelling separation, by evaluating the impact of a non-rigorous but conservative ICGCs population, defined on the basis of a more heuristic approach. For this purpose, we define two samples of the GCs for our modelling work. The first sample consists of the GCs within two effective radii of NGC 1399, where we exclude extreme radial velocity GCs (hereafter referred to as *inner* sample) likely to be unbound to the galaxy and just projected on its central region by chance. The second sample consists of the entire sample of GCs, including the ones in the outer halo of NGC 1399 extending out to five effective radii (hereafter referred to as *full* sample). This sample includes, besides the *inner* sample, also: 1) a dominant component of GCs belonging to the intra-cluster component, and 2) the GCs bound to all other galaxy cluster members in the area covered by the FVSS sample.

For the *inner* sample, we selected the GCs by performing cuts in a phase-space distribution similar to paper FVSS-III. We first calculated the scatter in the radial velocities of GCs within two effective radii (r_{eff}) of a galaxy and used $\pm 2\sigma$ of this velocity scatter around the galaxy LOS velocity as the lower and upper boundary to select the GCs belonging to each galaxy (for details, see section 5.2 of FVSS-III). In contrast to FVSS-III, instead of applying fixed cuts in velocity, we calculate the radially varying LOS velocity scatter of GCs within

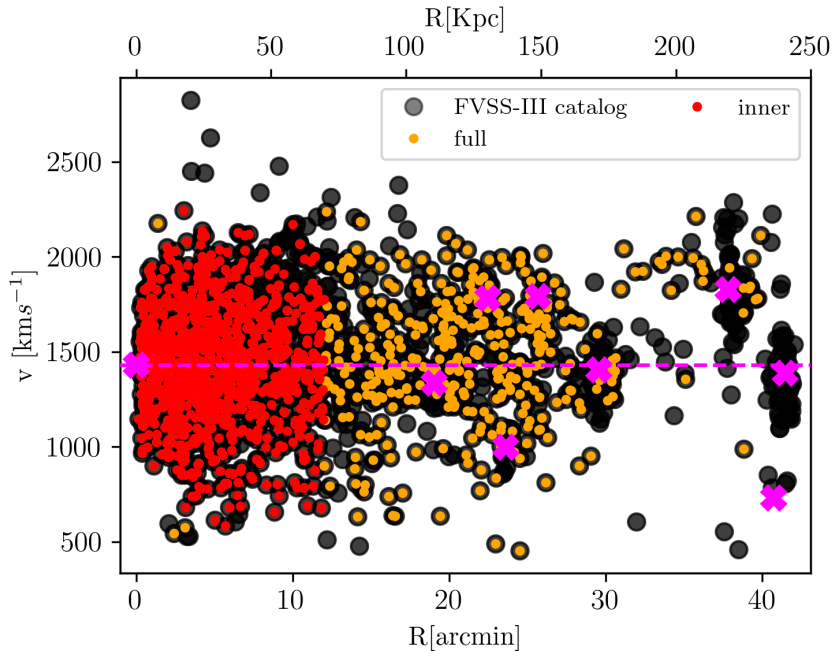


Figure 3.2.: LOS velocities of GCs sample (as mentioned in Sect.3.2) vs. cluster-centric distance. Black dots indicate the full sample of GCs from paper FVSS-III. Red and orange dots indicate the GCs of the *inner* and *full* samples, respectively. Magenta crosses indicate major galaxies and the horizontal dashed line marks the systemic velocity of NGC 1399.

$2r_{\text{eff}}$ of NGC 1399. We used $\pm 2.5\sigma$ velocity scatter around NGC 1399 LOS velocity as the lower and upper boundary to select the GCs belonging to the central galaxy. We adopted the r -band r_{eff} measured using the isophotal fitting from Iodice et al. (2019).

The giant elliptical NGC 1404 lies at a projected distance of $2r_{\text{eff}}$ from NGC 1399, and its outer halo GCs overlap in phase space with the GCs of NGC 1399. Therefore, we removed the GCs belonging to NGC 1404 from the GCs sample selected within $2r_{\text{eff}}$. The GCs selection around NGC 1404 was done in a similar way as done for the *inner* sample but adopting the effective radius of NGC 1404.

For the *full* sample, we consider the entire FVSS-III catalog of GCs, although we limit it to 200 kpc distance due to spatial incompleteness of the spectroscopic samples. Within 200 kpc, the GC systems of another four major galaxies, NGC 1387, NGC 1380B, NGC 1379 and NGC 1380, contribute to the sample. We remove the GCs bound to these galaxies similarly as described above. This left us with a total of 1640 GCs. Figure 3.1 shows the radial velocity map of *full* sample of GCs, while figure 3.2 shows the projected LOS velocity of the two different GCs samples. Red and orange dots denote the *inner* and *full* samples. One can clearly see the presence of GCs between the Fornax cluster galaxies. Despite the sharp separation of these two samples, we remark that the *full* sample extends outside a radius of $10'$, which has been found to mark a transition in the observed profiles of the light distribution (Iodice et al., 2016), X-ray distribution (Paolillo et al., 2002), mirrored by the dynamical properties (Napolitano et al., 2002) and kinematics (Spiniello et al., 2018) of

3. Mass-modelling of the BCG NGC 1399

the planetary nebulae and GCs (Pota et al., 2018). All these evidences converge toward a scenario where the intra-cluster population is expected to dominate in the regions at $R > 10'$ (~ 58 kpc), consistent with our selection.

3.2.2 Globular clusters (GCs) surface density

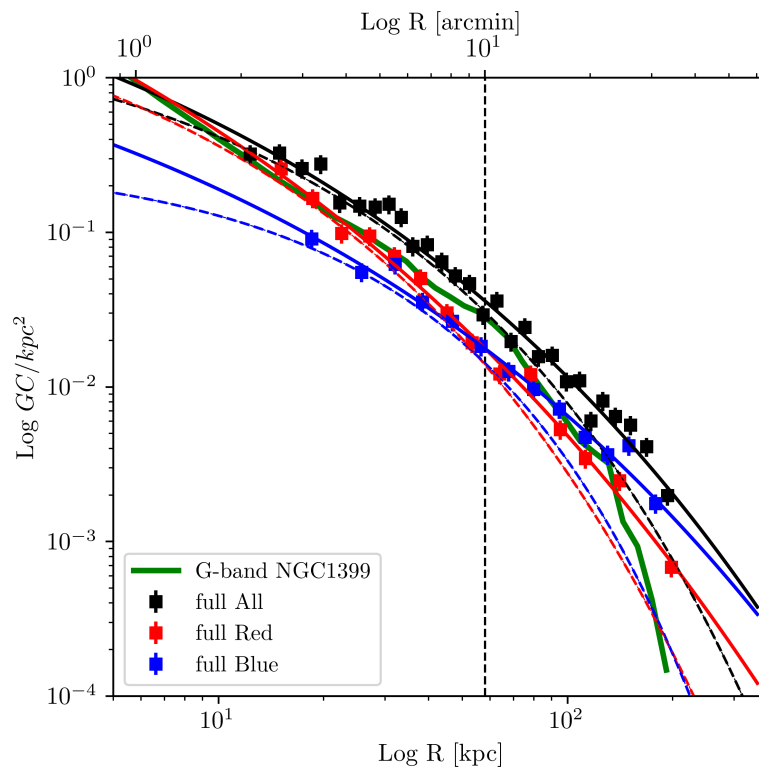


Figure 3.3.: GCs radial surface density profiles around NGC 1399. The vertical dashed line indicates one effective radius of NGC 1399. The green curve shows the g band scaled stellar surface brightness of NGC 1399. The solid black, red and blue curves show the Sersic fits of all, red and blue GCs of the *full* sample, respectively, whereas the dashed curves show the same for the *inner* sample.

As an input for the dynamical modelling, we need the GC tracer density (described in section 3.3). To measure the GCs surface density, we divided the spectroscopic GC sample into circular radial bins with an equal number of 50 GCs in each bin. The uncertainty of the surface density was determined with the Poissonian method. To have a uniform sample of GC magnitudes in each circular bin, we selected GCs brighter than $i < 23.2$ mag. For dividing the GCs sample into red and blue subpopulations, we adopted a $g - i$ colour value of ~ 0.97 , used in FVSS-III. To account for the inner spatial incompleteness we fit the GCs surface density profile from 1 to 30 arcminutes and drop the first binned datapoint.

Similar to the work of Pota et al. (2015), we characterise the GCs surface density profile, using the Sersic function Sérsic (1963), of the form:

$$I(r) = I_o \exp \left\{ -b \left[\left(\frac{R}{R_e} \right)^{1/n_e} - 1 \right] \right\} \quad (3.1)$$

, where $b = 1.9992n - 0.3271$ and I_o is the surface density at characteristic radii R_e .

Table 3.1.: Best fit parameters of the Sersic profile for the GCs surface density profile.

Sample	I_e	R_e	n_e
<i>inner</i>	log [GC/kpc ²]	[kpc]	
All	0.063	40.39	2.11
Red	0.085	25.63	2.35
Blue	0.025	43.02	1.41
<i>full</i>			
All	0.038	56.03	3.38
Red	0.069	30.10	4.32
Blue	0.083	87.90	3.63

The best-fit values of the all, red and blue GC populations of the *inner* and *full* samples are shown in Table 3.1. Figure 3.3 shows the corresponding GC number density profiles. Continuous lines indicate the Sersic fits of the *full* sample. For clarity, we only show the Sersic fit and not the data points of the *inner* (marked as dashed curve) samples. Figure 3.3 also shows the *g*-band stellar surface brightness profile of NGC 1399, adapted from the work of [Iodice et al. \(2016\)](#). We find that red GCs show a similar surface density profile as the galaxy’s stellar surface brightness.

The projected number density profile can be used to derive the 3D density profile, needed for the dynamical modelling (described in Section 3.3, see also [Napolitano et al., 2014](#)). The de-projection of the GC number density $j(r)$ is performed, assuming a spherical symmetry, via the Abel integration ([Binney & Tremaine, 1987](#)):

$$j(r) = -\frac{1}{\pi} \int_R^\infty \frac{dI}{dR} \frac{dR}{\sqrt{R^2 - r^2}} \quad (3.2)$$

Here, r and R are the 3D and 2D radii. $I(R)$ is the projected number density of the tracer, in units of number/ kpc^2 for GCs.

3.2.3 GCs kinematics

The line of sight velocity distribution (LOSVD) of particles in a given potential is usually described, in the most general case, via Gauss Hermite polynomials ([Gerhard, 1993](#)). The first and second-order velocity moments quantify the Gaussian-like component of the LOSVD, and the higher-order moments can measure the deviation of the LOSVD from a Gaussian distribution. Higher order moments such as kurtosis (κ) contain information about the

3. Mass-modelling of the BCG NGC 1399

orbital distribution of the GCs (Napolitano et al., 2014). Following Napolitano et al. (2014) we model the projected velocity dispersion and kurtosis profile using the high-order radial Jeans equations (see also Lokas et al., 2005), as we detail in Sect. 3.3. Here below we describe the procedure to derive the observed velocity moments that will be modeled with our dynamical procedure.

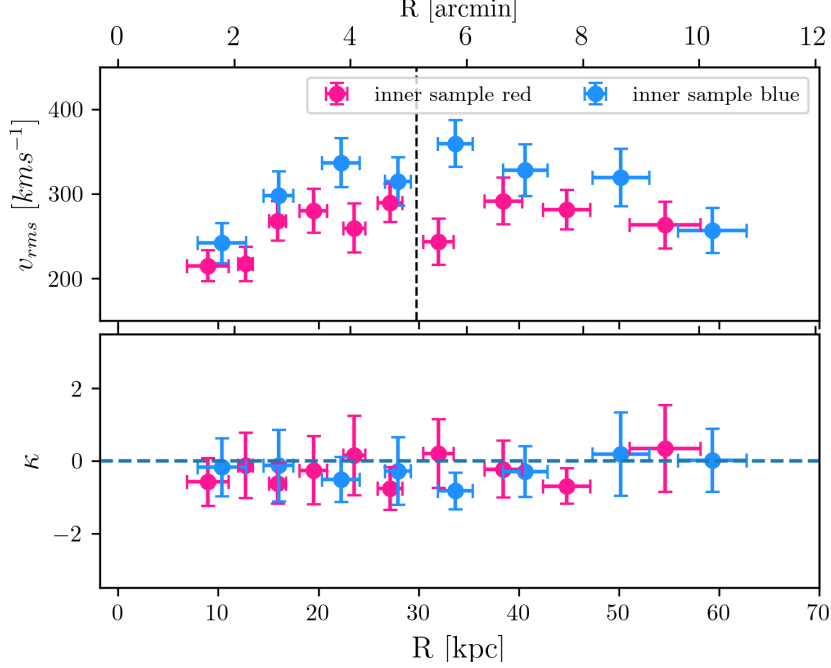


Figure 3.4.: Velocity dispersion and kurtosis profiles of the *inner* sample as defined in section 3.2. Top and bottom panels show the velocity dispersion and kurtosis profiles of red and blue GCs, respectively. The vertical dashed line in the top subplot indicates $1r_{\text{eff}}$ of NGC 1399.

Velocity dispersion

We calculate the GC velocity dispersion in a similar manner as described in paper FVSS-III. We first divide the GCs in circular radial bins such that each bin contains an equal number of GCs and use the following expression to derive the velocity dispersion:

$$v_{rms}^2 = \frac{1}{N} \sum_{i=1} (v_i - v_{sys})^2 - (\Delta v_i)^2 \quad (3.3)$$

Here v_i is the radial velocity of i th GC, and Δv_i is its velocity uncertainty. We use a systemic velocity $v_{sys} = 1430 \text{ km s}^{-1}$ from Iodice et al. (2019). The uncertainty of the velocity dispersion is determined through a bootstrap technique. For each radial bin, we measure the velocity dispersion 1000 times and consider its 1σ scatter as the uncertainty. For the *inner* sample, we used a bin size of 50 GCs for the red and blue subpopulations, whereas, for the *full* sample, we used 100 GCs per bin. We have checked that using a smaller bin

size for both samples produces a noisier profile, however, the overall pattern of the profile remains the same.

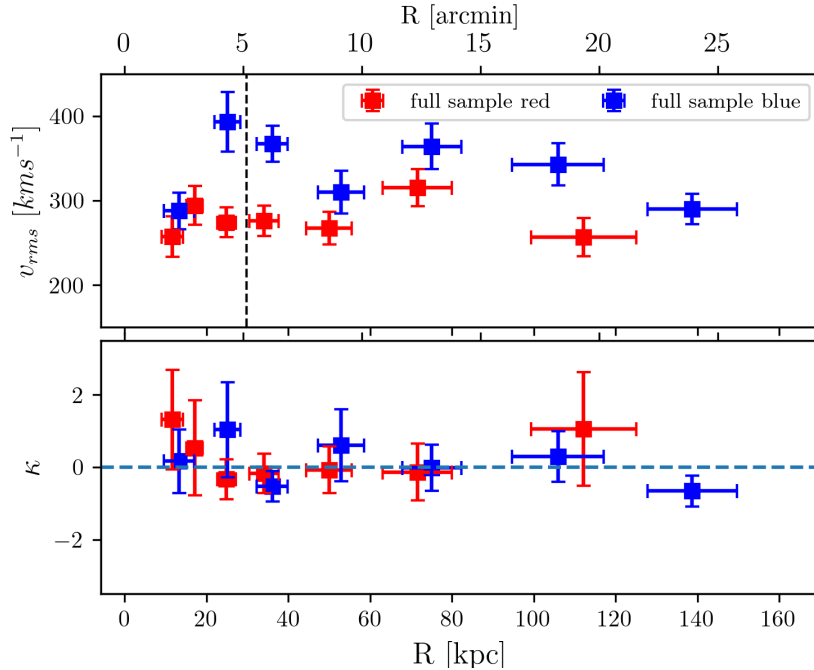


Figure 3.5.: Same as Figure 3.4 but for the *full* sample.

In Figure 3.4, the top panel shows the velocity dispersion profiles of the red and blue GCs of the *inner* sample, and Figure 3.5 for the *full* sample. The vertical dashed line indicates one effective radius of NGC 1399. We notice that for both samples, the blue GCs have a higher velocity dispersion than the red GCs. In case of the *inner* sample, the velocity dispersion profile is smooth since the GCs selection was performed using a $\pm 2.5\sigma$ LOS velocity cut around NGC 1399. This removes the extreme radial velocity GCs. In the case of the *full* sample, blue GCs have velocity dispersions which are, on average, $\sim 100 \text{ km s}^{-1}$ higher than those of red GCs. Beyond one r_{eff} , the velocity dispersion profile of red GCs remains flat around 300 km s^{-1} and the one of the blue GCs around $\sim 380 \text{ km s}^{-1}$.

Higher order velocity moments

We measure the kurtosis in the same circular radial bins as used for the velocity dispersion profiles with the following expression (see [Joanes & Gill, 1998](#), for the exact expression):

$$\kappa = \frac{\overline{v^4}}{\overline{v^2}^2} - 3 \quad (3.4)$$

For a Gaussian LOSVD, $\kappa \sim 0$, a value of $\kappa > 0$ suggests radial orbits, and $\kappa < 0$ tangential orbits. In Figure 4, the GCs kurtosis profiles of both samples are shown. For the *inner* sample, the blue and red GCs have a relatively constant κ with values mostly < 0 ,

3. Mass-modelling of the BCG NGC 1399

suggesting tangential orbits. In the case of the *full* sample, the kurtosis profile shows a noisy behaviour within one r_{eff} . There is no distinct behaviour between the two populations. For the outermost bins, κ becomes even noisier.

3.2.4 GCs rotation

To find any rotational signature in the GC population, we modelled the GC kinematics as a function of position angle with a simple model that describes the rotational amplitude and velocity dispersion. We adopted the fitting methodology similar to the approach of [Fahrion et al. \(2020a\)](#), for details, see their section 4.2.1) or [Côté et al. \(2001\)](#); [Veljanoski & Helmi \(2016\)](#).

Compared to paper FVSS-III, here we reexamined the rotational analysis in more detail. We first start by analysing the *inner* sample. We divided the GCs into two radial bins, each 5 arcmin wide. Red GCs do not show any rotational signature. The rotational amplitude is lower than 30 km s^{-1} . In contrast, for the blue GCs, we observe a rotational amplitude of $\sim 74 \pm 35 \text{ km s}^{-1}$ and a rotational angle of 126 degrees. These values agree with the previous rotational analysis of NGC 1399 GCs by [Schuberth et al. \(2010\)](#), see sections 7 and 7.4). However, we observe a lower rotational amplitude of blue GCs in comparison to [Schuberth et al. \(2010\)](#). The measured difference between our and [Schuberth et al. \(2010\)](#) values could be explained by different GC samples.

For the *full* sample, we divided the sample into three radial bins, each 10 arcmin wide. Similar to the *inner* sample, we do not see any rotation signature for the red GCs. Only in the outer bins between 20 to 30 arcmin distance we find a rotational amplitude of $\sim 60 \pm 50 \text{ km s}^{-1}$. However, the value is not significant due to the large uncertainty. For the blue GCs, we observe a mild rotation with an amplitude of $\sim 65 \pm 25 \text{ km s}^{-1}$ within 20 arcmin. In terms of v_{rot}/σ , the blue GCs have a value of ~ 0.22 , showing a slowly rotating system.

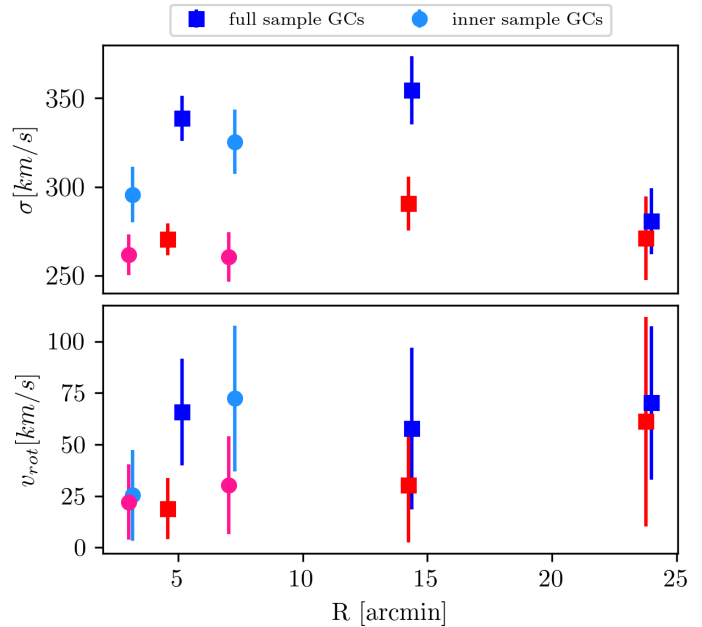


Figure 3.6.: Rotational amplitude and velocity scatter of GCs.

3.3 Dynamical modelling

We use the tracer density (sec. 3.2.2) and kinematics information to obtain the baryonic and DM mass profile of NGC 1399 and the Fornax cluster. We apply higher order Jeans moments for the dynamical modelling work, similar to what was used in [Napolitano et al. \(2009, 2011, 2014\)](#). Here we briefly summarise the Jeans modelling and present the methodology.

3.3.1 Jeans modelling

The Jeans equations are obtained by taking the velocity moments of the collisionless Boltzmann equation, which relates the tracer's phase-space distribution in a given gravitational potential. The Jeans equation connects the tracer velocity distribution and its anisotropy to the total dynamical mass of the system. Assuming a spherical symmetry and a non-rotating system, the Jeans equation is written as:

$$\frac{d}{dr}(j\sigma_r^2) + \frac{2\beta}{r}j\sigma_r^2 = -j\frac{d\phi}{dr} = j\frac{GM_{\text{tot}}}{r^2} \quad (3.5)$$

Here j is the tracer 3D number density, M_{tot} is the total mass of the system, σ_r is the radial velocity dispersion, and ϕ is the gravitational potential. β is the tracer anisotropy, which can be expressed as:

$$\beta = 1 - \frac{\sigma_t^2}{\sigma_r^2} \quad (3.6)$$

Here, $\sigma_t = \sigma_\phi = \sigma_\theta$ for a spherical symmetry.

One of the limitations of the Jeans modelling technique is the mass-anisotropy degeneracy. Traditionally, the approach considers the different orbital distributions like radial, tangential or isotropic and solves equ. 3.5 to obtain the projected velocity dispersion. The fourth moment of the LOSVD, kurtosis, contains information about the orbital distribution of the tracers. The projected fourth-moment Jeans equations writes:

$$\frac{d}{dr}(j\overline{v_r^4}) + \frac{2\beta}{r}j\overline{v_r^4} = -3j\sigma_r^2\frac{d\phi}{dr} \quad (3.7)$$

Using this equation to constrain the kurtosis can alleviate and control the mass-anisotropy degeneracy (see [Lokas & Mamon, 2003](#); [Lokas et al., 2005](#)). This procedure has been applied and well tested for the dynamical modelling of massive galaxies (for details see [Napolitano et al., 2009, 2011, 2014](#)).

We apply the dispersion-kurtosis analysis and use the solution of the Jeans equations, σ_r and $\overline{v_r^4}$, to obtain the projected second and fourth velocity moments as:

$$\sigma_{\text{los}}^2(R) = \frac{2}{I(R)} \int_R^\infty \left(1 - \beta \frac{R^2}{r^2}\right) \frac{j\sigma_r^2}{\sqrt{r^2 - R^2}} dr \quad (3.8)$$

3. Mass-modelling of the BCG NGC 1399

and projected fourth moment,

$$v_{los}^4(R) = \frac{2}{I(R)} \int_R^\infty \left(1 - 2\beta \frac{R^2}{r^2} + \frac{\beta(1+\beta)}{2} \frac{R^4}{r^4} \right) \frac{j\bar{v}_r^4 r}{\sqrt{r^2 - R^2}} dr \quad (3.9)$$

In equ. 3.9 β is constant, but can be generalised for radial dependence (see equ. 35 and 37 of Richardson & Fairbairn, 2013). In our case, we consider the β parametrisation introduced by Churazov et al. (2010) :

$$\beta(r) = \frac{\beta_{out} r^c + \beta_{in} r_a^c}{r^c + r_a^c} \quad (3.10)$$

Equation 3.10 is characterised by the two anisotropy parameters β_{in} and β_{out} that produce asymptotic values for $r \rightarrow 0$ and $r \rightarrow \infty$, respectively, and r_a is the anisotropy radius and exponent 'c' regulates the transition between β_{in} and β_{out} . We adopt $c = 2$, which corresponds to the Osipkov–Merritt model (Osipkov, 1979; Merritt, 1985), where $\beta_{in} = 0$ and $\beta_{out} = 1$. For our modelling purpose, we fix $c = 2$ and vary β_{in} and β_{out} .

3.3.2 Gravitational potential

For the gravitational potential we have considered the two components of stellar and dark matter (DM) mass. The total mass as in Eq. 3.5, is defined as:

$$M_{tot}(r) = M_*(r) + M_{DM}(r) \quad (3.11)$$

where M_* and M_{DM} are the stellar and dark matter mass.

The stellar mass profile $M_*(r)$ is obtained by integrating the deprojected g -band luminosity profile of NGC 1399 as:

$$M_*(r) = 4\pi\Upsilon_* \int_0^r \nu_*(r) r^2 dr \quad (3.12)$$

where Υ_* is the stellar-to-mass ratio.

Dark matter halo

Numerical dark matter only simulations have shown that the DM halo can be well described with a cuspy profile in the centre. However, the very inner character of the profile depends on the numerical details used in the simulations (Bullock et al., 2001; Schaller et al., 2015). Observational studies of low-surface brightness galaxies have shown a cored DM profile (Burkert, 1995). In our case, we have considered two profiles describing the dark matter (DM) contribution to the gravitational potential, the cored Burkert profile (Burkert, 1995) and the cuspy NFW profile (Navarro et al., 1997).

Burkert profile

The Burkert DM density profile is characterised by the scale radius r_o and density normalisation parameter ρ_o and is expressed as the following:

$$\rho(r) = \frac{\rho_o}{\left(1 + \frac{r}{r_o}\right) \left(1 + \frac{r^2}{r_o^2}\right)} \quad (3.13)$$

The cumulative mass profile for the Burkert halo is given as:

$$M(r) = 4\pi\rho_o r_o^3 \left(\frac{1}{2} \ln \left(1 + \frac{r}{r_o}\right) + \frac{1}{4} \ln \left(1 + \frac{r^2}{r_o^2}\right) - \frac{1}{2} \arctan \left(\frac{r}{r_o}\right) \right) \quad (3.14)$$

NFW profile

The NFW profile is given by:

$$\rho_{NFW}(r) = \frac{\rho_s}{\left(\frac{r}{r_s}\right) \left(1 + \frac{r}{r_s}\right)^2} \quad (3.15)$$

where ρ_s and r_s are the characteristic density and radius. The cumulative mass profile for the NFW halo is expressed as :

$$M_{NFW}(r) = 4\pi\rho_s r_s^3 \left(\ln \left(1 + \frac{r}{r_s}\right) - \frac{\frac{r}{r_s}}{1 + \frac{r}{r_s}} \right) \quad (3.16)$$

3.3.3 Maximum likelihood analysis

We employ a maximum likelihood (ML) approach to infer the best-fit parameters used in our dynamical modelling. Following bayesian analysis, the posterior probability distribution is the product of the likelihood function of the observation (the data in our case are velocity dispersion or kurtosis) given the model with some parameters and priors on the model parameters. The set of model parameters that maximize the likelihood function produces a model that best fits the data. The total likelihood is the product of the individual measurements of the dataset.

In our case, we create two likelihood functions corresponding to the velocity dispersion and kurtosis of the GCs. Assuming a Gaussian LOSVD, for a given population k of GCs (either red or blue) with a standard deviation equal to the uncertainty of the measured v_{rms} , the log-likelihood of observing a GC population having a velocity dispersion v_{rms} , given a set of model parameters $\mathbf{M} = \{\Upsilon, r_s, \rho, \beta_{in}, \beta_{out}\}$ is:

3. Mass-modelling of the BCG NGC 1399

$$\ln p_{v_{rms}}(v_{rms_k} | \mathbf{M}_k) = -\frac{1}{2} \sum_{i=1}^N \left[\left(\frac{v_{rms,i} - \sigma_k}{\Delta v_{rms,k}} \right)^2 + \ln(2\pi \Delta v_{rms,i}^2) \right] \quad (3.17)$$

Here N is the number of bins used in the v_{rms} profile. Similarly, we have another log-likelihood term for κ , and the combined log-likelihood is written as:

$$\ln L = \ln p_{v_{rms}} + \ln p_{\kappa} \quad (3.18)$$

Now considering the two-component Jeans modelling for the combined red and blue subpopulations, we have the total log-likelihood expressed as :

$$\mathcal{L} = \sum_{k=1}^2 \ln L_k \quad (3.19)$$

Model Parameters

For one-component modelling of GCs, we have five parameters, including the mass-to-light ratio Υ_* , the scale radius and density normalization parameter of the DM density profile and two anisotropy parameters of beta: $\{\Upsilon_*, r_s, \rho, \beta_{in}, \beta_{out}\}$.

We first modelled the red GCs of NGC 1399 and adopted the best fit value of Υ_* for the rest of the models. For the two-component models, this left us with a total of six parameters as: $\{\Upsilon_*, r_s, \rho, \beta_{inr}, \beta_{outr}, \beta_{inb}, \beta_{outb}\}$.

To find the best-fit parameters, we utilize the EMCEE package (Foreman-Mackey et al., 2013), a python-based implementation of the affine-invariant Markov Chain Monte Carlo (MCMC) sampling algorithm. The EMCEE package uses several walkers to explore the parameters space and uses a specified number of steps to converge to best-fit values. We used a total of 50 walkers and run the models for 2500 steps to ensure the parameters space is well explored. For the prior function we used a uniform prior range as following: $\Upsilon_* : \{1, 10\}$, $r_s : \{10, 300\}$ kpc, $\log \rho : \{5.5, 9.5\}$ M_{\odot}/kpc^3 and $\beta_{in} = \beta_{out} : \{-1.5, 1.0\}$.

3.4 Results

This section presents our results from the dynamical modelling and the best-fit parameters. We performed the dynamical modelling fitting for one component tracer, i.e. fitting the red and blue GCs kinematics independently, as well as a joint two-component tracer modelling for fitting both red and blue GCs kinematics together. Here, we focus on the two-component modelling since it allows us to reduce the mass-anisotropy degeneracy.

Table 3.2.: Best fit parameter of the two-component joint modelling.

Sample	Parameters										Likelihood
<i>inner</i>	ρ_o	r_o	β_{outr}	β_{inr}	β_{outb}	β_{inb}	$\text{Log } M_{200}$	R_{200}			\mathcal{L}
	$[M_\odot/\text{kpc}^3]$	$[\text{kpc}]$					M_\odot	kpc			
Burkert	$7.02^{+0.16}_{-0.14}$	$34.03^{+7.80}_{-6.63}$	$-0.26^{+0.67}_{-0.77}$	$-0.69^{+0.69}_{-0.60}$	$0.62^{+0.24}_{-0.37}$	$-1.15^{+0.62}_{-0.46}$	$13.34^{+0.46}_{-0.45}$	$590.94^{+247.47}_{-171.72}$			-95.40
NFW	$6.18^{+0.32}_{-0.27}$	$147.70^{+86.80}_{-57.38}$	$-0.32^{+0.66}_{-0.73}$	$-0.71^{+0.63}_{-0.55}$	$0.64^{+0.23}_{-0.35}$	$-1.17^{+0.58}_{-0.47}$	$13.81^{+1.01}_{-1.00}$	$845.62^{+990.67}_{-452.18}$			-97.48
<i>full</i>											
Burkert	$7.04^{+0.13}_{-0.12}$	$35.54^{+5.82}_{-5.10}$	$0.13^{+0.23}_{-0.38}$	$0.45^{+0.20}_{-0.37}$	$0.27^{+0.18}_{-0.32}$	$-0.86^{+0.60}_{-0.57}$	$13.42^{+0.35}_{-0.34}$	$628.37^{+193.26}_{-145.43}$			-76.89
NFW	$6.45^{+0.21}_{-0.18}$	$98.18^{+27.07}_{-22.76}$	$0.07^{+0.30}_{-0.44}$	$0.11^{+0.38}_{-0.57}$	$0.42^{+0.13}_{-0.24}$	$-0.97^{+0.47}_{-0.35}$	$13.62^{+0.58}_{-0.57}$	$732.59^{+410.31}_{-260.53}$			-76.85

3. Mass-modelling of the BCG NGC 1399

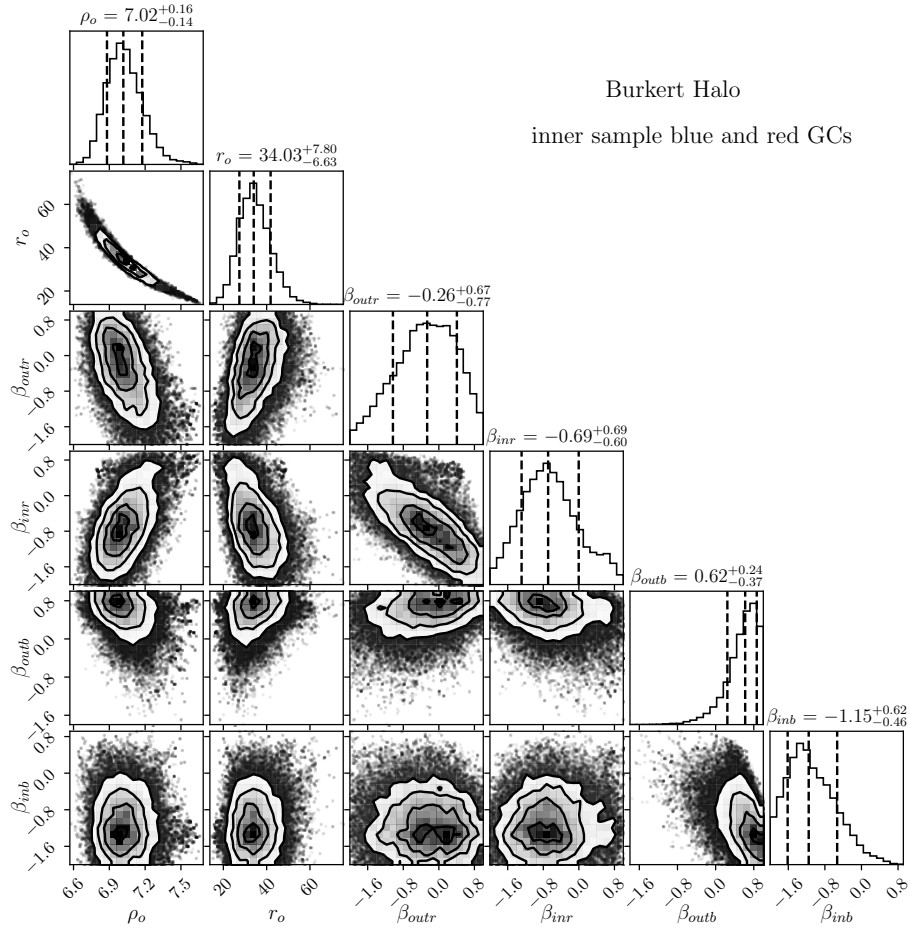


Figure 3.7.: 1D and 2D posterior distributions of the parameters (MCMC output) from the two-component Jeans modelling using the Burkert halo for the *inner* sample. The histogram on top of each column shows the 1D distribution of the corresponding parameter, and error bars (vertical dashed lines) mark the ± 16 and 84 percentiles. In the 2D projections, the contours denote the 1, 2, 3σ region of the projected covariance.

3.4.1 Fit to the kinematic data

For simplicity and to reduce the number of parameters in the modelling, we adopt the mass-to-light ratio parameter (Υ_*) resulting from fitting the red and blue GCs of the *inner* sample. For both Burkert and NFW halo, we find that the resulting Υ_* is ~ 4.20 in the Sloan *g* band. We use this value as a fixed parameter for the *full* sample models.

inner sample

We begin with the joint-component modelling of the *inner* sample. We find that both, NFW and Burkert halo, produce the observed kinematics quite well. Table 3.2 shows the best-fit parameters for both models. Figures 3.7 and 3.8 show the 1D and 2D posterior distributions of the parameters for the Burkert and NFW halo, respectively. The scale radius of the NFW halo is unusually high, but due to large uncertainties it is not well constrained. Moreover,

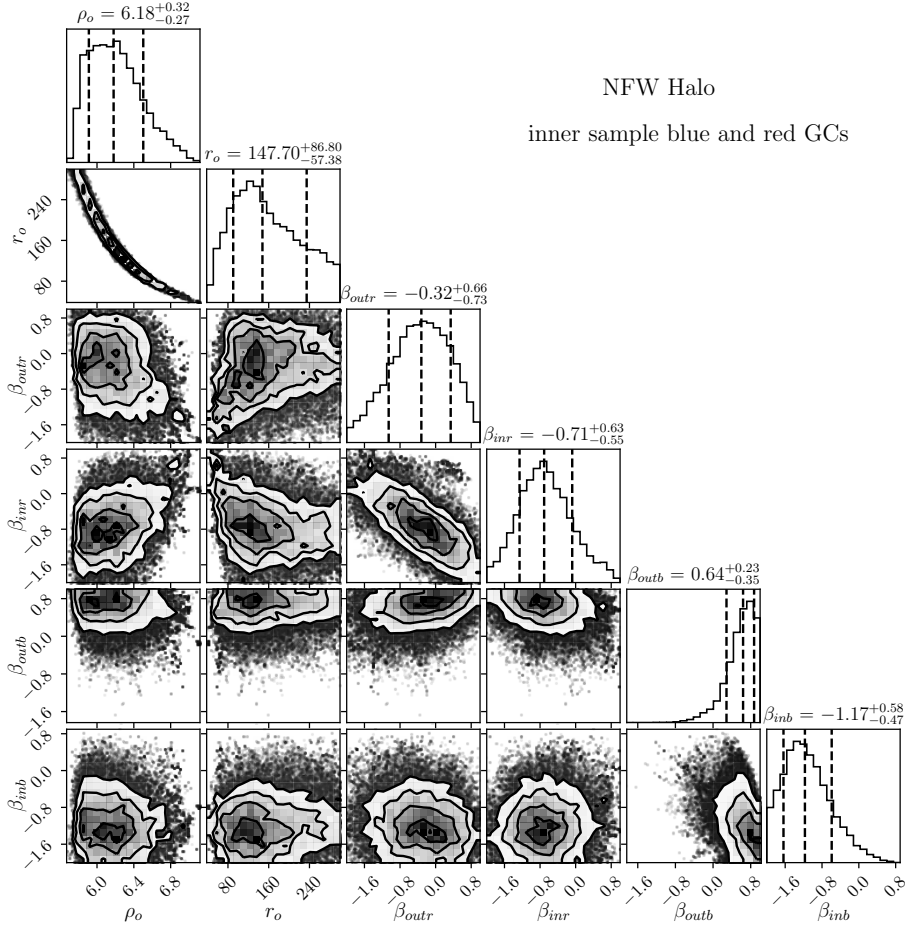


Figure 3.8.: Same as figure 3.7, but using NFW halo.

the outer anisotropy parameter (β_{out}) for blue GCs is not well constrained. In Figure 3.9, the left and right panels show the best fit models for the Burkert and NFW halo, respectively. For the anisotropy profile, both models show strong tangential anisotropy for the blue and red GCs in the inner region (within 30 kpc). Beyond that red GCs gradually tend to an isotropic behaviour, whereas blue GCs show a mild radial anisotropy in the outskirts.

The maximum likelihood from these two models is almost the same, and, therefore, it is hard to differentiate between the best fit model. However, to compare these two and other models, we have calculated the virial mass M_{200} and virial radius r_{200} . Here M_{200} is defined as the enclosed mass within r_{200} , such that the average density within r_{200} is 200 times the critical density of the Universe. Table 3.2 shows the M_{200} and r_{200} values of the models. Given the large-scale radius obtained for the NFW halo, the resulting M_{200} for the NFW halo is higher than that of the Burkert halo. However, considering the unconstrained value of the scale radius of the NFW halo, the obtained value is not reliable.

3. Mass-modelling of the BCG NGC 1399

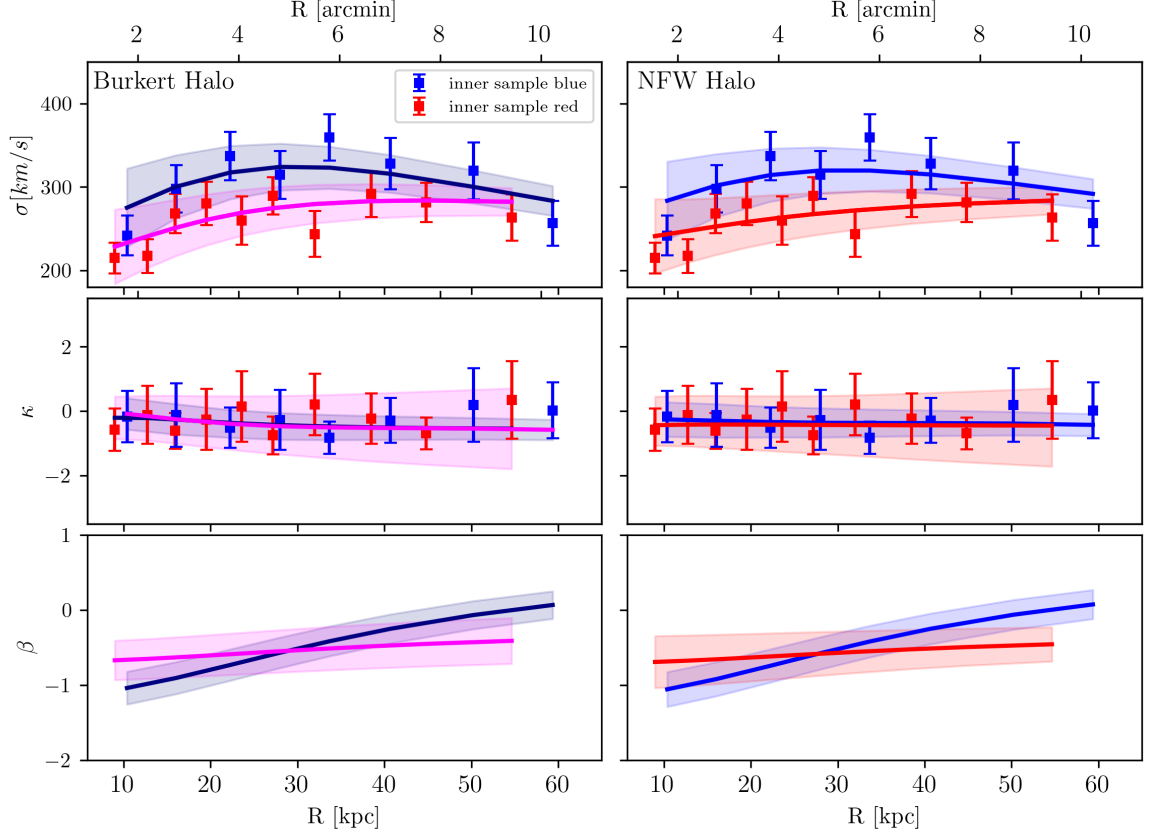


Figure 3.9.: Velocity dispersion and kurtosis profiles of the *inner* sample as defined in Section 3.2. Left: Best fit model for Burkert halo. Top and middle panels show the velocity dispersion and kurtosis profiles for the red and blue GCs. Solid line indicates the best fit model. Lower panel shows the anisotropy profile obtained from the best fit parameter (Table 3.2) using equ. 3.10. Right: Same as left but for the NFW halo best parameters.

full sample

Similar to the *inner* sample, both Burkert and NFW halos reproduce the observed kinematics well for the *full* sample. Figures 3.10 and 3.11 show the 1D and 2D posterior distributions of the parameters for the full sample for Burkert and NFW halo, respectively. Figure 3.12 shows the best fit model to the observed kinematics of the *full* sample. Compared to the *inner* sample, we find a different anisotropy behaviour for the red GCs in the inner region. For the Burkert halo, the red GCs show a mild radial anisotropic behaviour within 60 kpc and tend to have isotropic behaviour after 60 kpc. They show a similar behaviour for the NFW halo. In the case of the blue GCs, we find that within 40 kpc, they have a strong tangential behaviour and tend to have a mild tangential anisotropy within 80 kpc. Beyond that, the blue GCs show an isotropic behaviour getting mildly radial with increasing radius. In contrast to the *inner* sample, we find that M_{200} from both Burkert and NFW profile agree well within 1σ uncertainty. The M_{200} from NFW profile is slightly higher than the

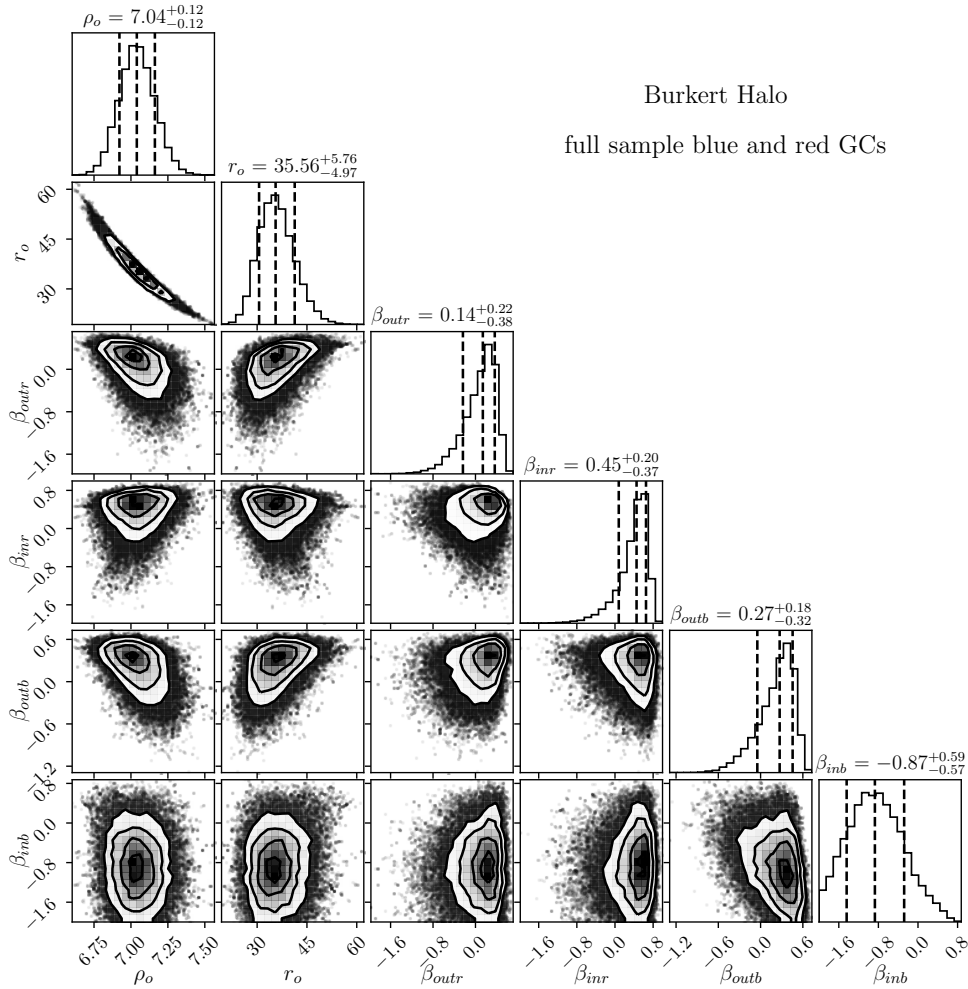


Figure 3.10.: Same as Figure 3.7, but for *full* sample and Burkert halo

Burkert halo and is around ~ 1.5 times of M_{200} measured from Burkert halo.

3.5 Discussion

In this section, we discuss and compare our modelling results and the orbital anisotropy of GCs to previous studies of NGC 1399 and simulation studies within the Λ CDM framework.

3.5.1 Mass profile

NGC 1399 has been well studied before using different kinematical tracers, allowing us to compare our NGC 1399 mass profile results with the previous literature studies. The earliest approaches to dynamically understand NGC 1399 were made by [Saglia et al. \(2000\)](#); [Napolitano et al. \(2002\)](#); [Schuberth et al. \(2008\)](#). Figure 3.13 shows the enclosed mass profile obtained from our best-fit models and compares it with previous work. The black and

3. Mass-modelling of the BCG NGC 1399

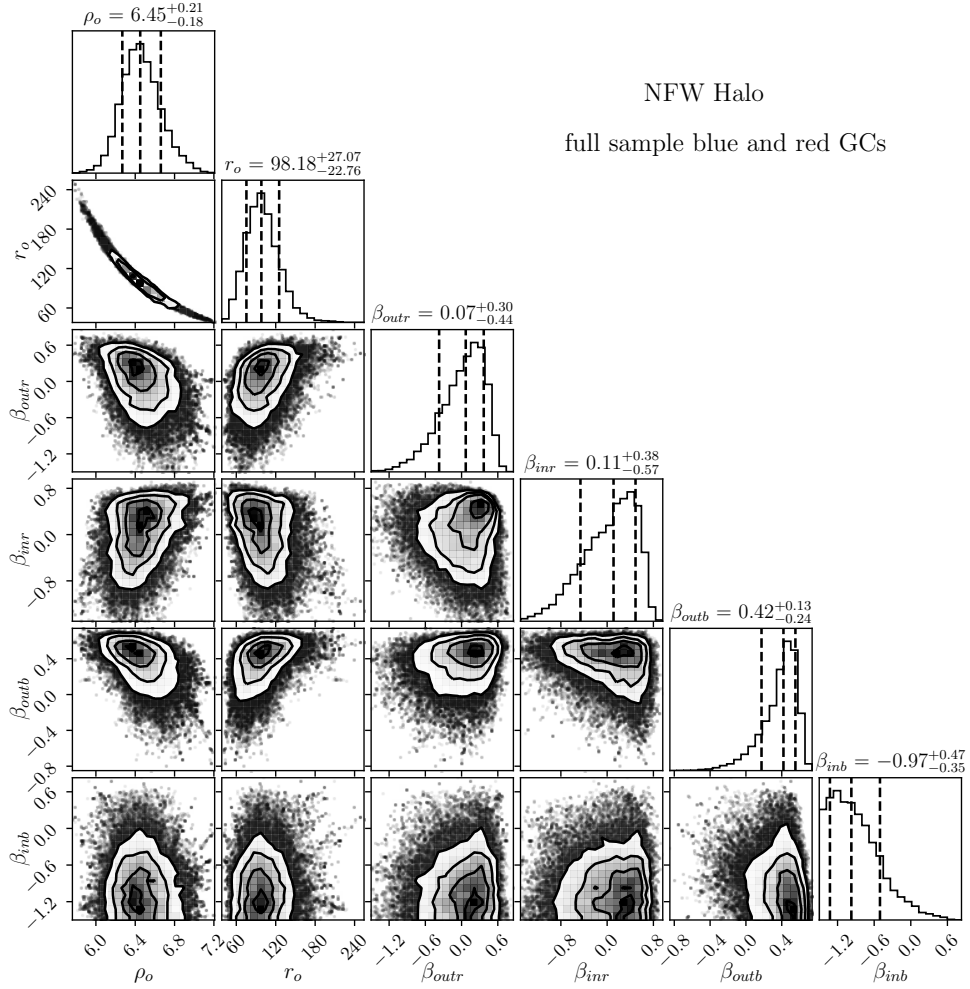


Figure 3.11.: Same as Figure 3.7, but for *full* sample and NFW halo

red curves indicate the mass profiles for the Burkert and NFW profiles for the *full* sample, respectively, whereas the dashed curves show the same but for the *inner* sample. For clarity, the 1σ uncertainty is shown only for the mass profile of the *full* sample.

For the *inner* sample, we find that the mass profiles for the Burkert (black dashed line) and NFW (red dashed line) halos agree. Within the inner 100 kpc, the mass profiles are almost the same, and beyond that the profiles start deviating. The NFW mass profile shows a ~ 1.5 times higher mass than the Burkert mass profile. In contrast to the *inner* sample, the mass profiles of the *full* sample for both, the Burkert and NFW halos, are in excellent agreement with each other within 150 kpc. Beyond that the mass profiles start deviating from each other. The virial masses M_{200} for both samples are listed in Table 3.2 and agree within their 1σ uncertainties with each other. The bottom panel in Figure 3.13 shows the DM fraction measured for the Burkert and NFW profiles for the *full* sample. At $1r_{\text{eff}}$, DM constitutes more than 70% of the total mass and contributes more than 95% at $5r_{\text{eff}}$.

Previous mass-profile measurements of NGC 1399 using GCs data have been performed by

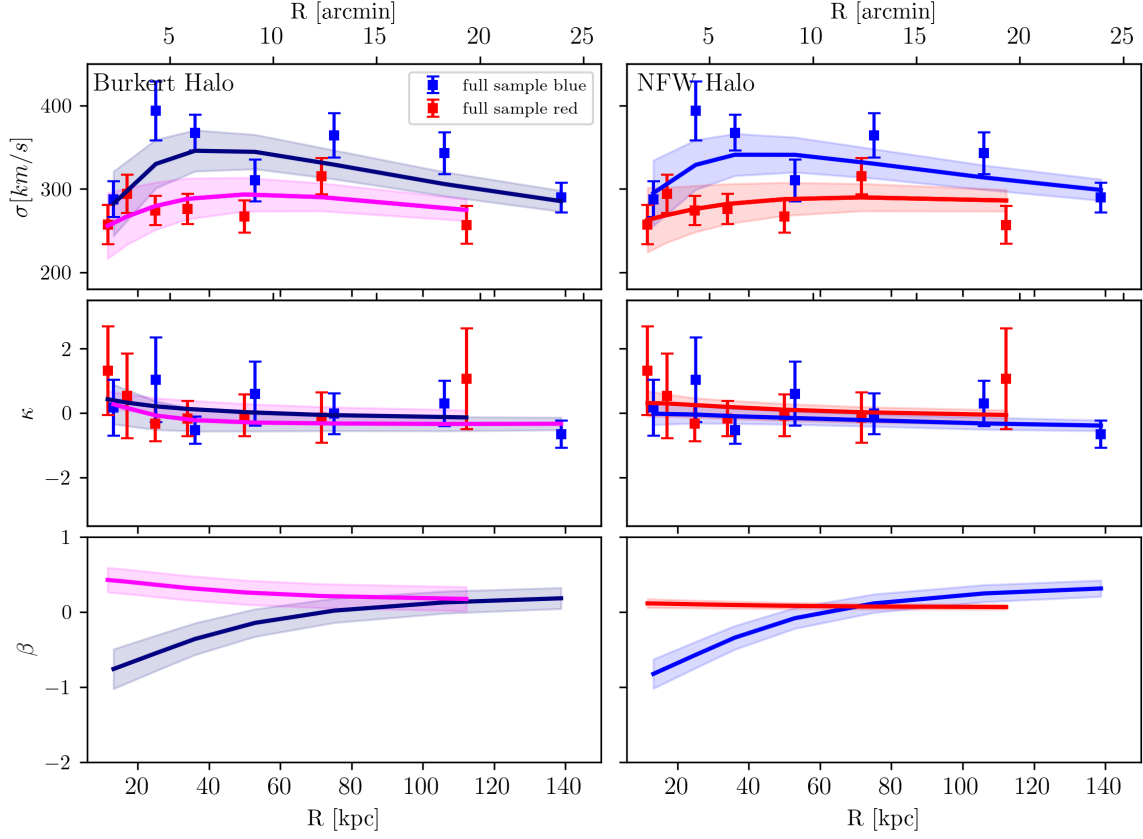


Figure 3.12.: Velocity dispersion and kurtosis profiles of the *full* sample. Left: Best fit model for Burkert halo. Top and middle panels show the velocity dispersion and kurtosis profiles for the red and blue GCs (squares) and solid lines indicate the best fit models. Right: Same as left but for the NFW halo best parameters.

Richtler et al. (2008); Schubert et al. (2008); Samurović (2016). Here we compare our results mainly with the Schubert et al. (2008) results. They used spherical Jeans modelling and GCs kinematics within 80 kpc around NGC 1399 to obtain its mass profile. In combination with GCs, they also used stellar kinematics available within the inner 10 kpc of NGC 1399 (Saglia et al., 2000). Assuming tangential, radial and isotropic beta profiles, they performed various sets of models. The mass profile from their best fit model ‘a10’, where they used red GCs and stellar kinematical modelling (for details, see their section 10), is shown as orange curve in Figure 3.13. Another mass profile from their model ‘a7’, which used a combined kinematic modelling of red and blue GCs, is shown in light green. Our mass profiles from both samples are consistent with the ‘a7’ model of Schubert et al. (2008), whereas the *inner* sample, shows a slightly higher enclosed mass profile. This might be related to the different physical scales of the *inner* and *full* samples. Our *inner* sample extends to 60 kpc, which is similar to the extent of the Schubert et al. (2008) GCs sample, whereas our *full* sample extends up to 150 kpc.

3. Mass-modelling of the BCG NGC 1399

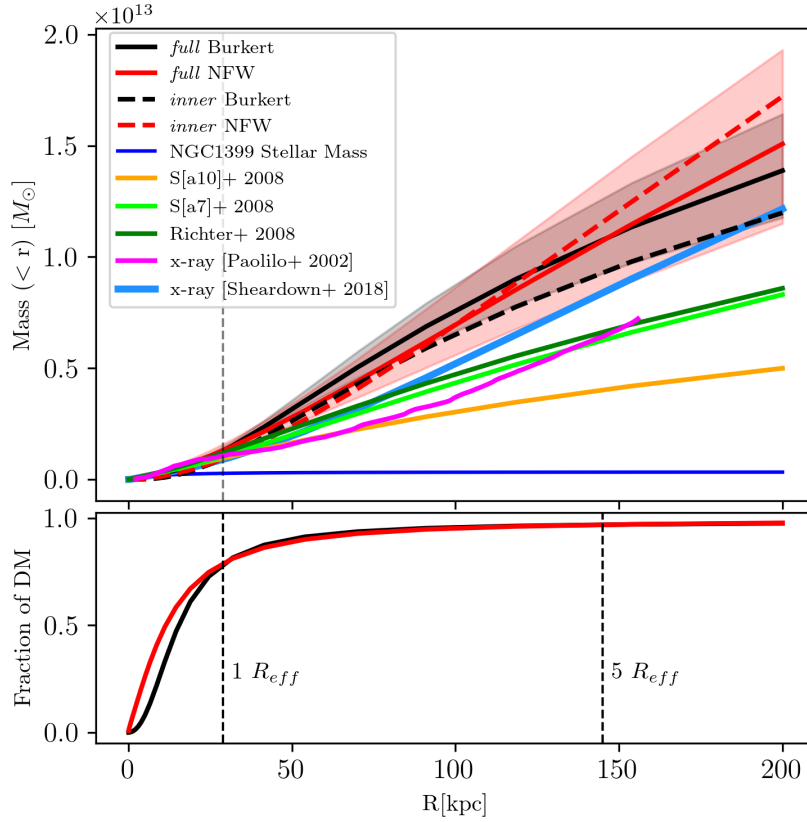


Figure 3.13.: Top panel: Enclosed mass profile of NGC 1399. The black and red solid lines indicate the enclosed mass for the *full* sample of Burkert and NFW halo, respectively. The dashed black and red lines denote the same but for the *inner* sample. Other lines show results from the literature. Bottom panel: DM fraction for the *full* sample for the Burkert (black) and NFW (red) halo.

One of the limitations of our dynamical modelling is that we used only cusp and core profiles and not a generalised inner slope of the DM halo profile. In the literature, several studies point towards the different physical processes, such as dynamical friction and active galactic nuclei feedback, that can change the inner slope of the DM halo profile (Blumenthal et al., 1986; Schaller et al., 2015; Peirani et al., 2017). The inner DM profile is influenced by the distribution of stars in galaxies; therefore, it is crucial to probe the generalised DM halo profile (Sand et al., 2004, 2008; Newman et al., 2013). In a future work (Chaturvedi et al. in prep), we plan to use archival MUSE data of NGC 1399 and orbit-based superposition Schwarzschild modelling technique (Jethwa et al., 2020) to fully understand the DM halo profile of NGC 1399.

The mass profile of NGC 1399 and the Fornax clusters as derived from X-ray studies was presented by Ikebe et al. (1996); Paolillo et al. (2002). In figure 3.13, the mass profile from Paolillo et al. (2002) is shown as a pink curve. Sheardown et al. (2018) studied the infall trajectory of the nearby giant elliptical NGC 1404 into the Fornax cluster using simulations

to match the X-ray observations performed by Chandra and XMM Newton, which extend out to 200 kpc from NGC 1399. They used a double Hernquist potential to model the total gravitational potential of the Fornax cluster, shown as the light blue curve in figure 3.13. The mass profile from Sheardown et al. (2018) overlaps with our mass profile for the NFW model of the *full* sample.

In summary, we find that independent of the DM halo profile used, the mass profiles for the *full* and *inner* samples agree within 1σ uncertainty with each other. By considering the *full* sample of GCs, we could constrain the DM halo parameters quite well, which results in obtaining a similar enclosed mass profile from both NFW and Burkert halo. This suggests that ICGCs trace the cluster potential and are essential in getting the total mass estimate.

3.5.2 Comparison with simulation studies

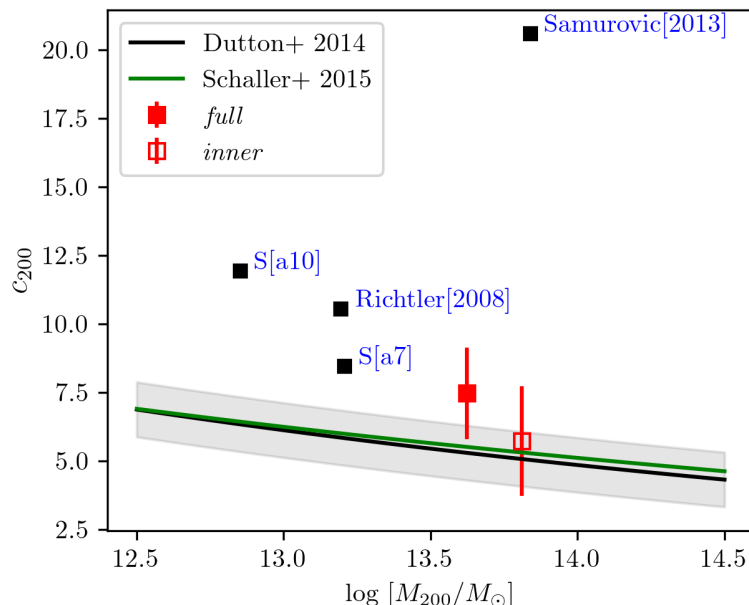


Figure 3.14.: Virial mass and concentration parameter relation. The black line and shaded grey region indicate the c_{200} and M_{200} relation and its uncertainty from Dutton & Macciò (2014) work. The open and filled red squares denote the measurements from our work for the *inner* and *full* sample, respectively. Black squares indicate the previously measured concentration parameter values of NGC 1399. The labels 'S[a7]', 'S[a10]', 'Richtler' and 'Samurovic' indicate the works from which these values were taken (a7, a10 models from Schubert et al., 2010) and Richtler et al. (2008); Samurović (2016), respectively.

Here we compare our results with results from cosmological simulations in the Λ CDM framework. Several of those simulations show a universal relation between DM concentration parameter c_{vir} and virial mass (Navarro et al., 1997; Bullock et al., 2001; Dutton & Macciò, 2014; Schaller et al., 2015; Diemer & Kravtsov, 2015). The concentration parameter c_{vir} relates the inner scale radius with the virial quantity parameters and is expressed as r_{vir}/r_s . As mentioned in Section 3.3, for comparing the different models, we used $\Delta_{vir} \sim 200$. We

3. Mass-modelling of the BCG NGC 1399

use the concentration-mass relation from the work of [Dutton & Macciò \(2014\)](#). They used the Planck cosmology ([Planck Collaboration et al., 2014](#)) in their DM-only cosmological simulations and found the following halo-mass relation:

$$\log_{10}c = a + b\log_{10}(M/10^{12}[M_{\odot}]) \quad (3.20)$$

where a and b are 0.905 ± 0.001 and -0.101 ± 0.001 (for redshift $z \sim 0$).

In Figure 3.14, the black dashed line shows the relation between c_{200} and M_{200} , and the shaded grey region marks its 1σ uncertainty. The green line shows the same relation from the [Schaller et al. \(2015\)](#) work, where they used EAGLE simulations, including baryonic matter. The filled and open red squares mark c_{200} obtained for the NFW profile for the *full* and *inner* samples, respectively. The previous measurements of the concentration parameter of NGC 1399 are indicated as the black squares from the work of [Schuberth et al. \(2010\)](#); [Richtler et al. \(2008\)](#); [Samurović \(2016\)](#). To compare these measurements with our work, we have rescaled them to Δ_{200} . The uncertainties on previous measurements were challenging to obtain, and accounting for uncertainties in our measurements, it's clear that our results are in close agreement with the simulation work based on the Λ CDM framework. With our modelling, we find a large DM scale radius for the NFW profile, whereas R_{200} is of the same order as previous measurements (see table 3.2). This results in a lower concentration parameter value close to the simulation work. We want to mention here that we cannot constrain the DM halo inner slope very well since we excluded the central kinematics of NGC 1399. Our results of c_{vir} and M_{200} may change upon considering a generalised NFW profile where the inner slope and scale radius are highly degenerate.

3.5.3 GCs orbital distribution

Lastly, we compare our anisotropy profiles with other massive systems available in the literature and discuss the results. In Figure 3.15, we show the orbital velocity anisotropy profile for the two-component joint modelling of the *full* sample. We obtained a radial anisotropic behaviour for the red GCs within 60 kpc, which becomes isotropic with increasing radius. For the blue GCs, we find a different behaviour. In the innermost region, they show a tangential anisotropic behaviour and become radial anisotropic in the outskirts beyond 60 kpc. This behaviour of blue GCs is consistent with the accretion scenario, i.e they were accreted from radially infalling galaxies.

In the literature, few works have probed the orbital distribution of GCs around massive galaxies ([Agnello et al., 2014](#); [Napolitano et al., 2014](#); [Zhu et al., 2016b](#); [Li et al., 2020](#)). These studies are based on various sample sizes and use different techniques, so the measured anisotropy, even for the same system, is not always consistent. Considering these caveats, we compare our results with massive systems such as NGC 5846 and M87 and draw some conclusions based on recent simulation studies of [Ramos-Almendares et al. \(2018\)](#).

M87 is the massive central galaxy of the Virgo cluster and hosts a very rich GC system. [Agnello et al. \(2014\)](#) showed that the red GCs around M87 have slightly tangential orbits in the inner parts and a nearly isotropic behaviour in the outskirts. In contrast, the blue

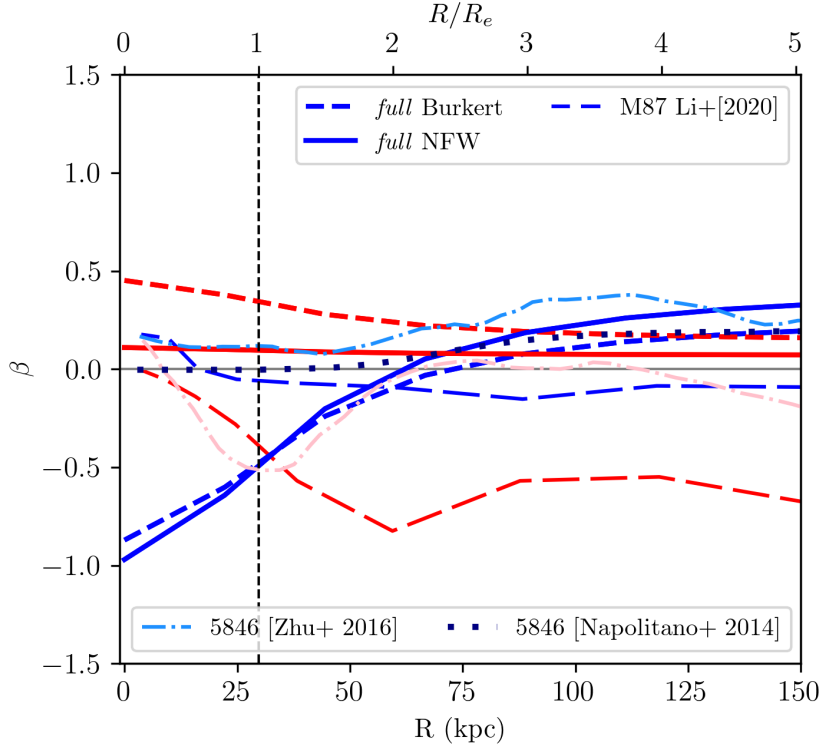


Figure 3.15.: Velocity anisotropy distribution of GCs for the *full* sample. Dashed red and blue lines indicate the anisotropy of the red and blue GCs for the Burkert halo and solid lines indicate the anisotropy for the NFW halo.

GCs are nearly isotropic in the centre and show a mildly tangential anisotropy at larger radii (>100 kpc.) Recently, [Li et al. \(2020\)](#) studied the M87 GC system out to 400 kpc with discrete dynamical modelling and found that red GCs have an isotropic behaviour in the centre and become tangential in the outskirts. The blue GCs show radial behaviour in the innermost region and are slightly tangential in the outskirts. In figure 3.15, long dashed blue and red lines denote the velocity anisotropy of M87 from [Li et al. \(2020\)](#). For NGC 1399, we observe that both red and blue GCs show a mild radial anisotropy in the outskirts. The light blue and pink dashed curves in figure 3.15 show the anisotropy profiles of NGC 5846 from [Zhu et al. \(2016b\)](#). In this galaxy the blue GCs show a radial anisotropic behaviour in the outskirts similar to what we observed for the blue GCs in NGC 1399.

Our finding of radial anisotropy of GCs, particularly of blue GCs, is consistent with recent work based on the Illustris simulation. [Ramos-Almendares et al. \(2018\)](#) found that intra-cluster GCs show a radial anisotropy ($\beta \geq 0.3$), suggesting that GCs have been accreted on radial orbits. For blue GCs, we find tangential orbits in the inner region of NGC 1399. It will be interesting to investigate how the inclusion of the inner stellar kinematics of NGC 1399 effects the dynamical modelling and orbital distributions of the inner red and blue GCs.

3.6 Summary and Conclusions

In this work, we have applied spherical non-rotating Jeans modelling to perform the dynamical mass-modelling of NGC 1399 using its GC system out to 200 kpc. We have solved the Jeans equation to obtain the projected dispersion and kurtosis of the observed GCs to obtain the total mass of NGC 1399 and velocity anisotropy of its GCs system. Our approach consists of the joint two-component tracer modelling of red and blue GCs, thus alleviating the mass-anisotropy degeneracy. We used two halo profiles for the dark matter halo, NFW and Burkert halo.

We used the FVSS spectroscopic catalogue produced in the FVSS-III paper and defined two kinematical samples of GCs around NGC 1399, divided based on a phase space and velocity cut to investigate the effect of intra-cluster GCs in the mass modelling (see section 3.2). The *inner* sample is limited to $2r_{\text{eff}}$ and the *full* sample extends to $\sim 6.5r_{\text{eff}}$.

The following are the main results of our work:

- 1) We find that both NFW (cusp) and Burkert (core) DM halo can reproduce the observed kinematics well. With our current modelling approach, we cannot discriminate which profile is preferred, the cusp or the core profile. The total mass obtained from our two-component tracer modelling agrees within 1σ uncertainty for both profiles. The virial mass (M_{200}) measured from the *inner* sample for the Burkert halo is $\log(M) = 13.34 \pm 0.45M_{\odot}$, and $\log(M) = 13.81 \pm 1.01M_{\odot}$ for the NFW halo.
- 2) Independent of the DM halo profile used, we find that the dynamical modelling of the *full* GC sample produces a M_{200} which is in close agreement for both profiles. The virial mass (M_{200}) for the Burkert halo is $\log(M) = 13.42 \pm 0.35M_{\odot}$, and for the NFW halo $\log(M) = 13.62 \pm 0.58M_{\odot}$.
- 3) Based on the velocity anisotropy parameterisation used in the dynamical modelling (see Section 3.3), we have measured the orbital distribution of the GCs around NGC 1399. For the *inner* sample, we find that independent of the DM halo profile used, both red and blue GCs show tangential anisotropy and become isotropic with increasing radii. For the *full* sample, red GCs show an isotropic behaviour. In contrast, blue GCs show strong tangential orbits within 60 kpc and tend to mild radial anisotropy in the outskirts consistent with recent simulation work pointing to an accreted nature of blue GCs.

Although we have not explicitly investigated the effect of the substructures observed around the vicinity of NGC 1399, our work demonstrates that including the GCs in the outer halos can change the mass estimates. Therefore, it is crucial to properly investigate the mass modelling based on the different phase space kinematics information. In future work, we plan to include the stellar kinematics of NGC 1399 and also the upcoming new observations from the FVSS survey to perform a multi-component mass-modelling of the Fornax cluster and expand our knowledge about its DM halo profile in detail.

4 | Distribution of atomic hydrogen in TNG50 Fornax-like galaxy clusters

The previous two chapters were based on using observational studies of the Fornax cluster and mass-modelling technique. In chapter 2, I used the VIMOS-MOS data of the Fornax cluster to detect and kinematically characterize the GCs within its core and intra-cluster regions. In chapter 3, I used the GCs radial velocity catalogue to perform the mass modelling of the Fornax central galaxy NGC1399 out to $5 r_{\text{eff}}$. We learned that including the ICGCs in the dynamical modelling can affect the mass estimate. Now, in this chapter, I study the intra-cluster medium of Fornax-like halos, from a theoretical point of view. Utilizing the TNG50-Illustris cosmological simulations and adopting the MeerKAT Fornax survey (MFS) observational criteria, I study the cold gas distribution in Fornax-like clusters and predict the expected HI covering fraction expected for MFS. The content of this chapter is based on *Chaturvedi et. al 2023, in prep, ApJ*, which will be submitted soon.

4.1 Introduction

In the current baryon cycling paradigm, galaxy evolution is strongly linked with the gaseous halo surrounding galaxies in the hot intra-cluster medium in the cluster environment. In this chapter, we call all baryons between the halo's central galaxy interstellar medium and its virial radius as the intra-cluster medium (hereafter ICM). This includes gaseous halos of individual galaxies known as the circum-galactic medium (CGM) residing within the cluster environment.

Cold gas in the ICM provides the fuel needed for star formation in galaxies. The ICM contains information about gas accretion and feedback driven by stellar and AGN outflows, which regulates the growth of galaxies. These processes lead to the development of the ICM as a multiphase and complex gaseous medium in the cluster environment ([Tumlinson et al., 2017](#)).

Understanding the physical processes in the ICM is crucial to building a comprehensive picture of galaxy evolution. For the low-mass, star-forming galaxies, it is expected that its halo can host an abundant amount of cold gas that may be acquired as fuel for future star formation. In the case of the massive galaxies halos, it can be attributed that they lack cold gas, resulting in their quiescent nature and not showing any recent star formation activity

4. Distribution of atomic hydrogen in TNG50 Fornax-like galaxy clusters

(Gauthier & Chen, 2011). However, current observational (Chen et al., 2018; Berg et al., 2019; Zahedy et al., 2019) and simulation studies (Davé et al., 2020; Rahmati et al., 2015; van de Voort et al., 2019; Nelson et al., 2020) suggest that at intermediate redshift ($0.3 \leq z \leq 0.8$), massive halos also have a significant amount of cold gas. For example, Chen et al. (2018); Zahedy et al. (2019) studied the CGM of luminous red galaxies (LRG) at redshift $z \sim 0.21$ - 0.55 and found that they host high column density of cold gas, as traced by HI and MgII. Other similar studies point toward the same conclusion that LRGs host an abundant amount of cold gas (Zhu et al., 2014; Lan & Mo, 2018; Anand et al., 2021, 2022).

We highlight here the important question of the origin and survival of cold gas in the ICM of massive halos at low redshift. Recently, more simulations have been able to predict the cold gas distribution in the CGM. For example, Nelson et al. (2020) have shown that cold gas in the halos of LRGs can be attributed to the thermal instability triggered by local density perturbations. They suggest that these perturbations are related to gas stripped from the infalling galaxies, tidal interaction, or ram pressure stripping. Performing a comparative study between cosmological and idealized simulations (individual galaxy halo simulations) Fielding et al. (2020) have also shown that cold gas is distributed out to large radii, and even extends to the virial radius for the Milky Way-like halos. They also suggest that non-spherical accretion and satellite galaxies contribute to the cold gas phase in the outer CGM.

In contrast to intermediate redshifts, the ICM of massive halos ($M_{\odot} \geq 10^{11}$) in the local Universe ($z \sim 0$) is limited to a few studies. Nonetheless, using the HI 21 cm emission line, radio observations have demonstrated the abundant existence of cold neutral atomic gas around massive elliptical galaxies (Serra et al., 2012, 2013a; Young et al., 2014; Serra et al., 2013b). However, these observations are limited to within tens of kpc around the targeted galaxies and are typically not sensitive to HI column densities below $\leq 10^{20}$, and therefore do not provide a comprehensive picture of the ICM.

The upcoming observations of the MeerKAT Fornax survey (hereafter MFS, Serra et al., 2019), a radio and continuum observation of the Fornax cluster, provide an excellent opportunity to study the HI gas in the Fornax CGM. Recent photometric and spectroscopic studies (Chaturvedi et al., 2022; Cantiello et al., 2020) have shown that the Fornax cluster mass assembly is still ongoing, making it an interesting target to study. MFS is dedicated to study the HI distribution within Fornax and the effect of the cluster environment on it. MFS will be sensitive down to a HI column density sensitivity of $\sim 5 * 10^{19} \text{ cm}^{-2}$ at a spatial resolution of ~ 10 arcsec (corresponds to ~ 1 kpc at Fornax distance) (Serra et al., 2019). With a mosaic area of 12 square degrees, MFS will detect HI in the Fornax intra-cluster (hereafter IC) region.

The recent availability of high-resolution TNG50 cosmological simulations (Nelson et al., 2019; Pillepich et al., 2019) provides a median spatial resolution of ~ 100 parsec, and its validation of cold gas (neutral and molecular hydrogen) against observational work (Popping et al., 2019; Diemer et al., 2019) makes TNG50 an ideal setup to explore the cold gas distribution in Fornax-like halos. This also provides a chance to forecast the upcoming MFS survey results and test the simulations against the MFS observations. In this work, we use

the TNG50 simulations (Nelson et al., 2019; Pillepich et al., 2019) and adopt the observing criteria of the MFS to study the HI content in the TNG50 halos similar to the Fornax galaxy cluster. We study the HI content and distribution in these halos and their IC regions. We calculate the HI covering fraction for these halos and predict the expected observed MFS HI covering fraction.

Both the spatial and velocity distribution of HI gas in the ICM of clusters and groups can be used to gain insight into the origin and survival of this cold gas. If the gas is correlated in both position and velocity with satellites, we can argue that the HI is likely either stripped from satellites, or cooling is induced by satellites. However, if cold gas is not correlated with satellite galaxy positions or velocities, we might argue that either cold gas formation is related to the central galaxy or that cold gas survives in the ICM for long enough to become virialized. In this paper we take the first step of making these spatial and velocity maps, leaving gas particle tracking to future work.

The chapter is organized as follows: In Section 4.2, we briefly introduce the TNG50 simulation and present the methodology for calculating the HI covering fraction. Section 4.3 presents our results about the HI distribution and its covering fraction. In Section 4.4, we discuss our results and compare them to current observational studies. Section 4.5 presents the summary of the work.

4.2 Simulation and Methodology

This section briefly introduces the TNG50 simulation and criteria for selecting the Fornax cluster-like halos. In addition, we present our methodology for calculating the HI column density and HI covering fraction of the selected halos in TNG50.

4.2.1 The TNG simulations

For our study, we use the TNG50 simulation (Nelson et al., 2019; Pillepich et al., 2019), the highest resolution simulation of the IllustrisTNG cosmological magneto-hydrodynamical (MHD) simulation suite (Nelson et al., 2018; Springel et al., 2018; Pillepich et al., 2018; Marinacci et al., 2018; Naiman et al., 2018). The IllustrisTNG project is a set of large cosmological simulations that include a variety of galaxy formation physics, including AGN feedback, that has been designed to match a wide range of observational constraints (Pillepich et al., 2018; Springel et al., 2018), and runs on the moving mesh code AREPO (Springel, 2010). The AREPO code solves the coupled evolution of dark matter, gas, stars, and black holes under the influence of self-gravity and ideal MHD. Developed with the key motivation to study galaxy formation physics and understand the growth of cosmic structure physics, the IllustrisTNG project uses three distinct simulation box sizes.

TNG50 runs with a box size of 51.7 Mpc per side with 2160^3 gas and dark matter particles. It provides a baryon mass resolution of $8.4 * 10^4 M_{\odot}$. The TNG50 simulation has three separate subbox runs and we used TNG50-1 (hereafter denoted as TNG50) which provides

4. Distribution of atomic hydrogen in TNG50 Fornax-like galaxy clusters

Table 4.1.: TNG50 halos similar to the Fornax galaxy cluster

TNG50 Halo ID	Virial Mass (M_{200})	Virial radii (R_{200})
1	13.97	9.59
2	13.81	8.46
3	13.54	6.92
4	13.50	6.71
6	13.54	6.88
7	13.52	6.80
9	13.51	6.75

a median spatial resolution of ~ 100 pc. We adopt this run, although the other boxes contain a larger number of Fornax cluster-sized objects, because we need high spatial resolution to study the interaction of cold clouds and the hot group medium. TNG50 adopts initial conditions and cosmological parameters consistent with the [Planck Collaboration et al. \(2016\)](#) cosmology with $h = 0.68$, $\Omega_b = 0.05$, $\Omega_m = 0.31$, $\Omega_\lambda = 0.69$, and $\sigma_8 = 0.82$ and assuming a flat universe governed by a Λ cold dark matter (Λ CDM) cosmology.

4.2.2 Fornax-like Halo selection

In TNG50, a galaxy cluster or a group of galaxies is referred as a halo or FOF (hereafter referred as halo), identified through the friends-of-friends algorithm. Within each halo, the SUBFIND algorithm identifies the subhalos including the primary most massive central galaxy and other satellite galaxies (hereafter referred as subhalos). To find galaxy clusters similar to the Fornax cluster in TNG50 at snapshot 99 (redshift $z = 0$), we applied virial mass selection criteria in the mass range of $10^{13.5} \leq M_{200} \leq 10^{14} M_\odot$, where M_{200} is defined as the mass enclosed within a virial radius R_{200} equal to 200 times the critical density of the Universe. With this condition, we find a total of 7 halos. From here onward, we refer to these halos as Fornax-like halos. In Table 4.1, we list the physical properties of these halos.

4.2.3 Atomic HI content

To determine the HI mass of gas particles in TNG50 Fornax-like halos, we use the [Popping et al. \(2019\)](#) molecular hydrogen fraction (H_2) catalogue, previously calculated for the TNG simulations. They studied the H_2 content of the galaxies for the IllustrisTNG simulations (specifically TNG100 and TNG50). [Popping et al. \(2019\)](#) adopted multiple empirical and theoretically motivated recipes to divide the neutral gas within a cell into a molecular and atomic component. In this work we use their fiducial recipe, which is based on the work by [Gnedin & Kravtsov \(2011\)](#).

[Gnedin & Kravtsov \(2011\)](#) performed detailed simulations including non-equilibrium chemistry and simplified 3D on-the-fly radiative transfer calculations. Based on these simulations, the authors presented fitting formulae for the H_2 fraction of neutral gas, as a function of the

dust-to-gas ratio of the gas relative to solar, the impinging UV radiation field and surface density of the neutral gas. Popping et al. (2019) assume that the dust-to-gas ratio scales with the metallicity of the neutral gas, that the local UV radiation field scales with the SFR of the gas cell with an additional contribution from the ionising UV background field. They calculated the gas surface density of a gas cell by multiplying its density with the Jeans length of the cell. A detailed description of the implementation of the Gnedin & Kravtsov (2011) fitting formulae within the TNG simulation suite is presented in Popping et al. (2019, see their Section 2).

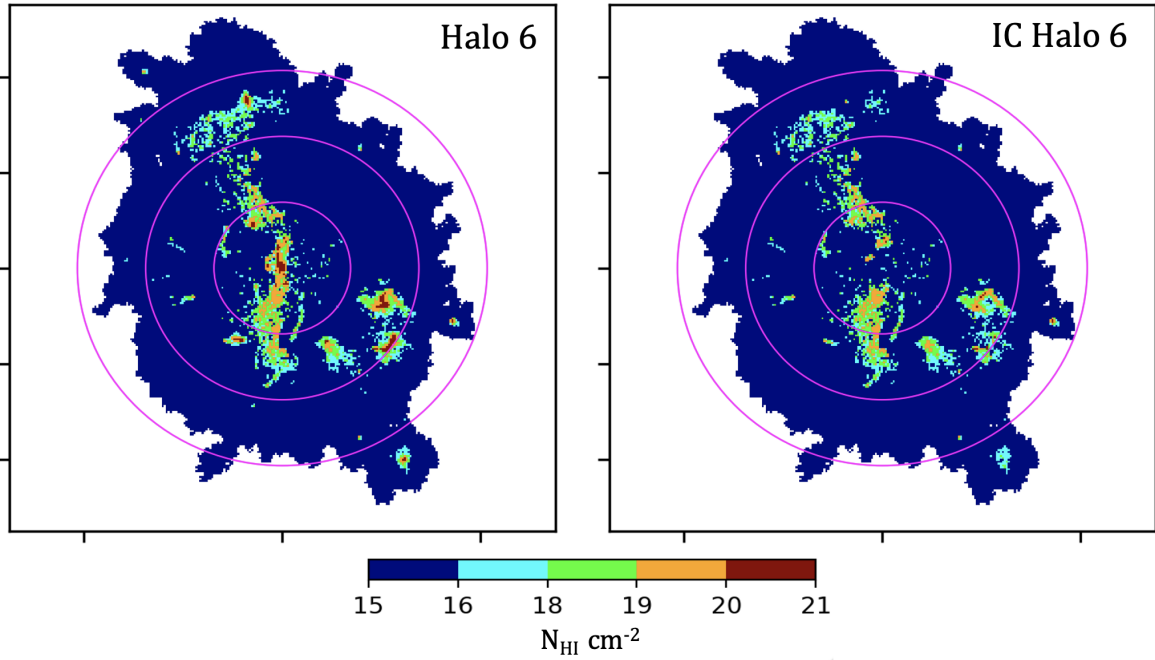


Figure 4.1.: HI distribution in the TNG50 halo 6 at redshift $z=0$, colour-coded with the HI column density. The maps are made using a pixel scale of 10 kpc and are shown projected along the (arbitrarily chosen) z -axis. The three pink circles indicate the virial radius of the halos marked at 0.5, 1.0 and 1.5 times R_{vir} . **Left:** Full halo HI distribution, **right:** HI distribution in the IC region.

4.2.4 HI column density

To measure the HI column density (hereafter denoted as N_{HI}), we perform a two-dimensional binning of the HI gas particles in the phase space, adopting a pixel size of 2 kpc similar to the MFS spatial resolution limit. For the binned HI gas particles, we calculate the N_{HI} in a pixel as follows:

$$N_{HI} = \frac{\sum_{i=1}^n M_{HI}}{m_{HI} * \text{Pixel Area}}$$

Here M_{HI} is the HI mass of a single gas particle summed over total n gas particles in a given pixel, and m_{HI} is the mass of the HI atom, and the area of the pixel is cm^2 , giving us

4. Distribution of atomic hydrogen in TNG50 Fornax-like galaxy clusters

N_{HI} in units of cm^{-2} .

4.2.5 Halo HI covering fraction

To understand and quantify the HI distribution in the halos, we measure their HI covering fraction in different column density bins adopting a range of $N_{\text{HI}} \geq 18, 19, \text{ and } 20 \text{ cm}^{-2}$. We measure the HI covering fraction in two ways similar to [Rahmati et al. \(2015\)](#) as follows:

Cumulative HI covering fraction (hereafter denoted as $f_{\text{HI}}(R)$) is defined as the fraction of surface area covered by the binned pixels having column density higher than a given N_{HI} value within a radius R over a total area of pixels within the same area of the 2d projected halo. $f_{\text{HI}}(R)$ is expressed as:

$$f_{\text{HI}}(R) = \frac{\sum_{i=1}^N A_{N_{\text{HI}}|R}}{\sum_{i=1}^N A|R} \quad (4.1)$$

Here $A_{N_{\text{HI}}}$ is the single pixel area with a column density equal or higher the given N_{HI} value and is summed over N such pixels in a given area of radius R divided by the total pixels in radius R .

Differential HI covering fraction (hereafter denoted as $f_{\text{HI}}(\Delta R)$) is defined similarly to be cumulative HI covering fraction, except here we consider the radial bins defined between radius R_j and R_{j+1} and $f_{\text{HI}}(\Delta R)$ is expressed as:

$$f_{\text{HI}}(\Delta R) = \frac{\sum_{i=1}^N A_{N_{\text{HI}}|\Delta R}}{\sum_{i=1}^N A|\Delta R} \quad (4.2)$$

4.3 Results

This section presents our results showing the HI distribution and covering fraction in the TNG50 Fornax-like halos and their IC regions. For the HI distribution in the IC regions of halos, we remove the HI gas particles gravitationally bound to all the subhalos (including central) within a halo, out to ten times the stellar half mass radius (denoted as $R_{1/2*}$).

Figure 4.1 (top panel) shows the HI distribution in TNG50 halo 6 around its central galaxy (left panel) and in the IC region (right panel). Three pink circles indicate the virial radius drawn at 0.5, 1.0 and 1.5 R_{vir} . For visualization purposes in the maps, we used a pixel scale of 10 kpc.

Figure 4.2 shows the HI distributions for all other Fornax-like halos (first two rows) and in their IC regions (lower two rows). The first visual impression we get from these plots is the large-scale distribution of HI extending beyond 0.5 virial radii for all the halos. We could also see the streams or filamentary-like structures connecting the central and satellite galaxies. Even for the HI distribution in the IC regions, it is quite clear that HI clouds extend out to 1 virial radius. In the IC region, the observed HI structures have primarily

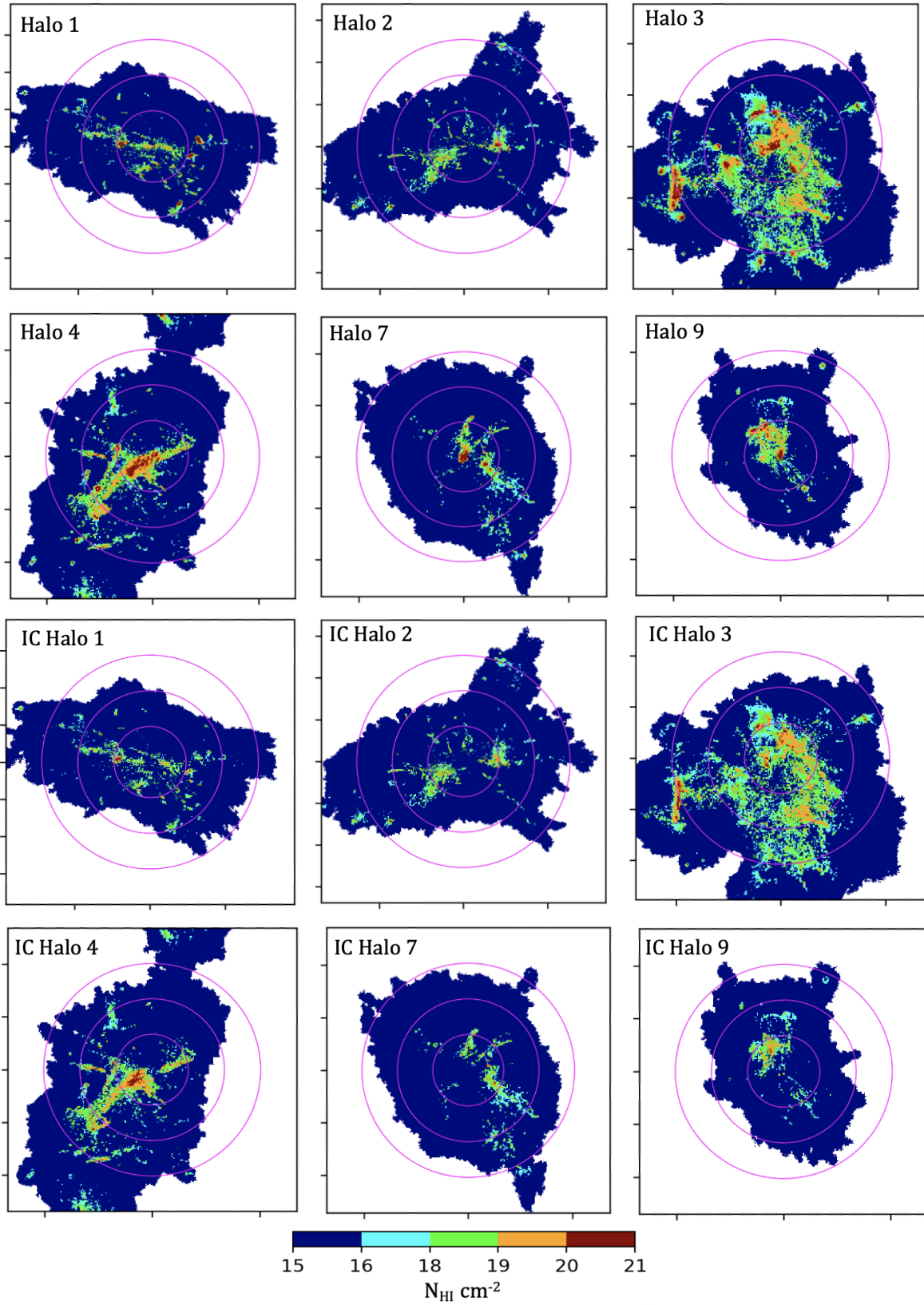


Figure 4.2.: HI distribution in the Fornax-like halos (first two rows) and in their IC regions (bottom two rows). The three pink circles indicate the virial radius of the halos marked at 0.5, 1.0 and 1.5 times R_{vir} .

4. Distribution of atomic hydrogen in TNG50 Fornax-like galaxy clusters

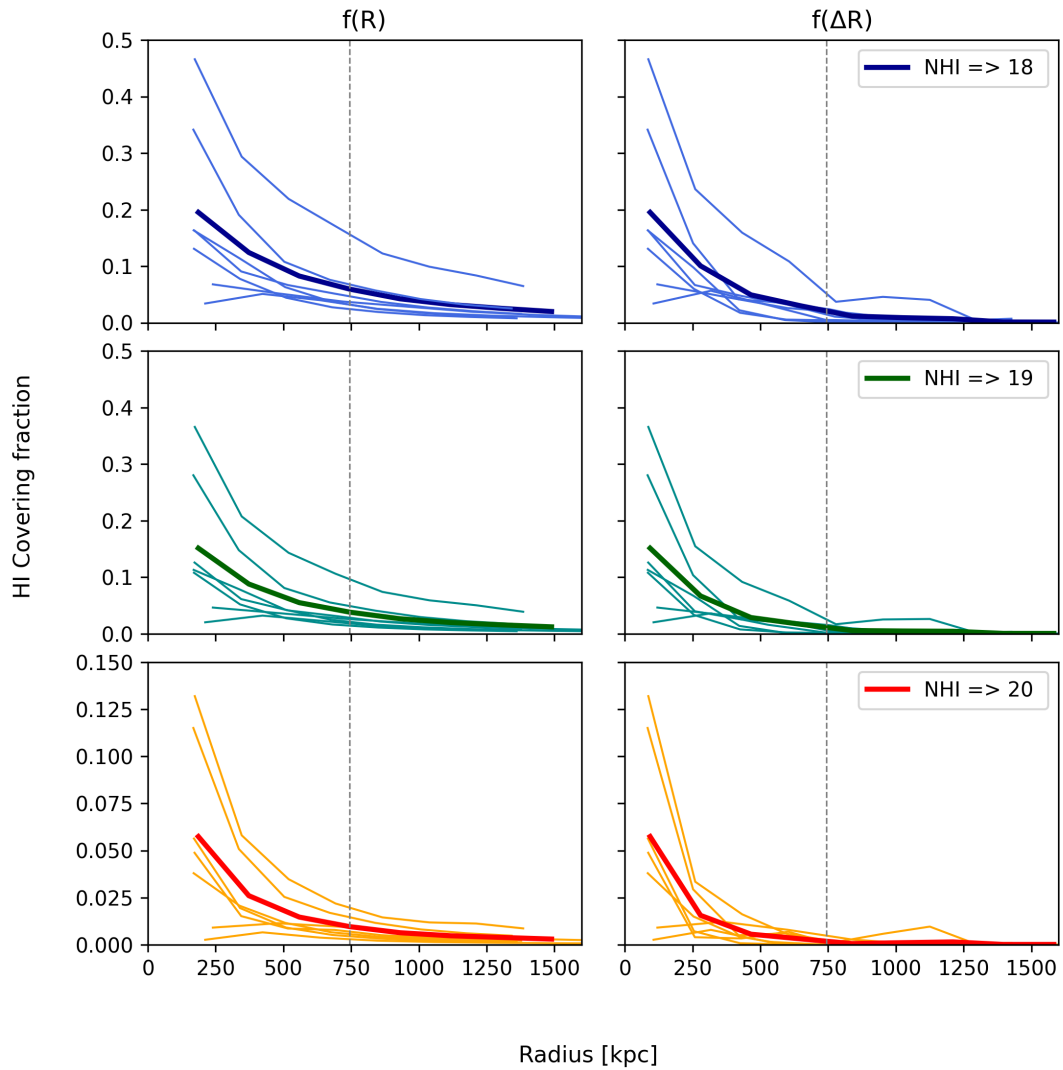


Figure 4.3.: HI cumulative (left panel) and differential (right panel) covering fraction profiles of Fornax-like halos. The first, middle, and bottom rows show the covering fraction for HI column densities $N_{HI} \geq 18$, 19 and 20, respectively. The thin lines indicate the individual halos, and the thick lines mark the average value. Vertical dashed lines indicate the average virial radii of the halos.

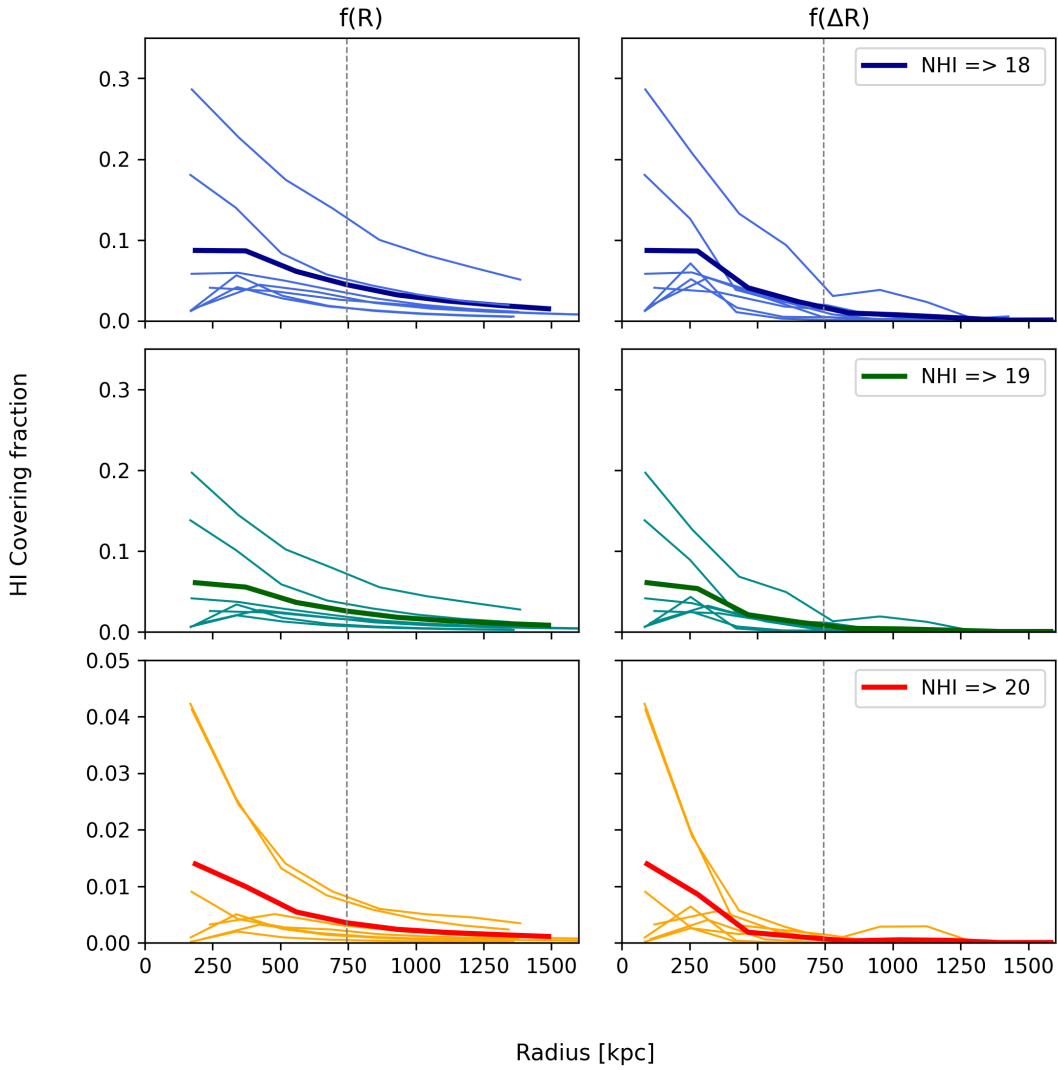


Figure 4.4.: The same as figure 4.3, but for the HI distribution in the intra-cluster (IC) region of Fornax-like halos. We obtain the IC HI by removing the gas particles gravitationally bounded to all the galaxies within $10 \times$ their stellar half mass radii.

4. Distribution of atomic hydrogen in TNG50 Fornax-like galaxy clusters

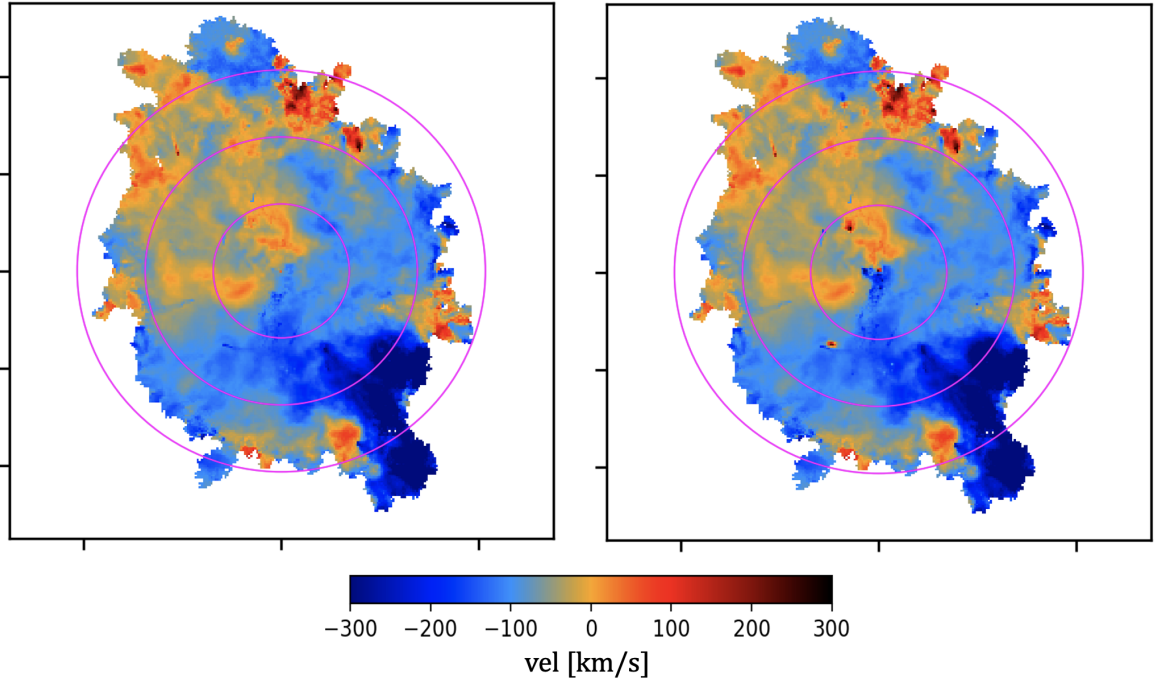


Figure 4.5.: Same as figure 4.1, but showing the velocity map of the HI distribution in the TNG50 halo 6 at redshift $z=0$, colour-coded by relative line-of-sight velocity. **Left:** Full halo HI distribution, **right:** HI distribution in the IC region.

column densities N_{HI} lower than 20, whereas the structures beyond 0.5 virial radii have N_{HI} lower than 19.

4.3.1 HI covering fraction profiles

We used the HI projected maps as shown in figure 4.1 for measuring the HI covering fraction as discussed in section 4.2. We measured the HI covering fractions of halos in three projections, along X, Y, and Z, using a pixel scale of 2 kpc. In figure 4.3 we show the cumulative and differential covering fraction profiles measured along the (arbitrarily chosen) Z-axis in the left and right panel, respectively. By definition, the innermost point of the cumulative and differential covering fractions are the same, then the differential covering fractions decrease more steeply than the cumulative covering fractions. The first, middle, and bottom row in both panels show the covering fraction for HI column density for $N_{HI} \geq 18, 19$ and 20, respectively. The thin lines indicate the individual halos, and the thick lines mark the average value.

We focus mainly on the N_{HI} bins of 18 and 19, which are the expected range for the MFS. We found that regardless of the projection axis, the average covering fraction for the bins at 18 and 19 is between 10-15 % at 0.5 virial radius and drops to 5-10% at $1 R_{vir}$. The differential covering fraction at 0.5 virial radius is between 5-10% and drops to less than 5% at $1 R_{vir}$.

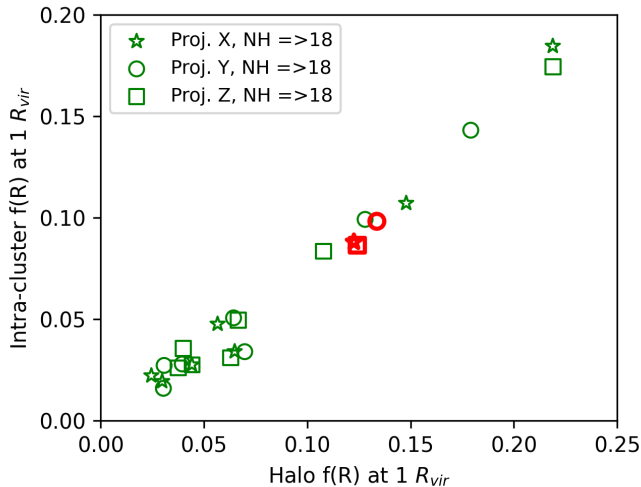


Figure 4.6.: Halo and intra-cluster cumulative HI covering fractions at $1 R_{vir}$ for three projected axes. Open stars, circles and squares indicate the X, Y and Z projections, respectively. The red star, circle and square indicate the average values

These covering fractions quantify our visual impression. Although all the halos have some HI gas within $0.5 R_{vir}$, it is distributed non-uniformly in smaller structures that look like filaments or clouds. These structures and clouds are potentially associated with the central galaxy and satellite galaxies (we discuss this in section 4.4.3).

4.3.2 Intra-cluster HI covering fraction

Figure 4.2 shows the HI distribution in the IC regions of the halos. An abundant quantity of HI gas particles with column density $N_{HI} \geq 18$ extends into the IC regions. It is primarily high column density HI gas particles $N_{HI} > 20$, which are removed as we perform our selection for the IC gas particles.

Similar to figure 4.3, we show the HI covering profiles for the IC regions in figure 4.4. For the N_{HI} bins 18 and 19, the cumulative covering fraction at 0.5 virial radius is between 5-10% and drops to less than 5% at $1 R_{vir}$ radius. In the case of $f(\Delta R)$, the covering fraction remains between 5-10% within $0.5 R_{vir}$ radius, suggesting that most of the IC HI gas is bounded to the central galaxy of the halo.

We checked the differences in the HI covering fraction along the different projected spaces. We find that, on average, the HI covering fraction remains the same and varies only by a few percent when changing the projected axis. Figure 4.6 shows the cumulative HI covering fraction at $1 R_{vir}$ between the Fornax-like halo and their IC region in three different projected axes for a column density $N_{HI} \geq 18$. The open stars, circles and squares indicate the X, Y and Z axis, respectively. The red star, circle and square indicate the average values. On average, the IC HI covering fraction is between 70-80% of the total HI covering fraction. This suggests that a large fraction, around $\sim 75\%$ of the extended HI gas, is actually part of

4. Distribution of atomic hydrogen in TNG50 Fornax-like galaxy clusters

the IC HI gas.

4.3.3 HI covering fraction in velocity space

We also measured the cumulative HI covering fraction in velocity space, adopting a velocity bin size of $\sim 100 \text{ km s}^{-1}$ within a range of -700 to 700 km s^{-1} . Figure 4.5 shows the HI distribution in velocity space, and figure 4.7 shows the HI covering fraction in velocity space for the halo and its IC region. The top, middle, and bottom panels show $f(R)$ for HI column densities of 18, 19 and 20. The thin lines indicate the individual halos, and the thick lines mark the average values. Dashed thin lines indicate the values of the IC regions. We find that in velocity space, on average the $f(R)$ is less than 5% for the column densities N_{HI} of 18 and 19, and significantly drops to less than 1 % for $N_{HI} = 20$.

4.4 Discussion

In this section, we discuss our results and compare the HI covering fraction to available observations and other cosmological simulation studies.

4.4.1 Comparison to other cosmological simulations

We begin by checking our measured cumulative HI covering fraction with the available HI covering fraction from the studies of [Nelson et al. \(2020\)](#). They measured the abundance of cold gas in TNG50 halos for massive halos with mass $> 10^{11} M_{\odot}$ at intermediate redshift $z \sim 0.5$. Although we have only 7 TNG50 halos, and apart from the evolution of the halos from redshift $z \sim 0.5$ to 0, the simulations and HI model we used are very similar to [Nelson et al. \(2020\)](#); therefore, the HI covering fraction should be of the same order. Indeed, our measured HI covering fractions for N_{HI} agree well with the [Nelson et al. \(2020\)](#) values. For a column density of $N_{HI} < 17$, we find a covering fraction of $\sim 70 \pm 15\%$ at 10 kpc, dropping to $30 \pm 15\%$ at 100 kpc, and for $N_{HI} < 20$, at 100 kpc, the covering fraction is roughly 10%, similar to the findings of [Nelson et al. \(2020\)](#). [Rahmati et al. \(2015\)](#) used the EAGLE simulation to study the HI distribution at high-redshift massive galaxies. They found a strong evolutionary trend in the HI covering fraction within the virial radius with redshift. For an averaged HI column density in between $17.3 < N_{HI} < 21$, the HI covering fraction drops from 70 % at $z = 4$ to 10 % at $z = 1$.

Previously, [van de Voort et al. \(2019\)](#) have shown that with standard mass refinement and high spatial resolution of 1 kpc the inferred HI column density can significantly change. Studying zoom-in simulations, they found that the HI covering fraction for $N_{HI} \geq 19$ at 150 kpc is almost doubled from 18% to 30%. Although the simulation setup of [van de Voort et al. \(2019\)](#) and TNG50 are different, when considering the kpc resolution scale, we also find similar results comparable with the [van de Voort et al. \(2019\)](#) values. In our case the cumulative HI covering fraction within 150 kpc is around 25 %, quite close to the [van de](#)

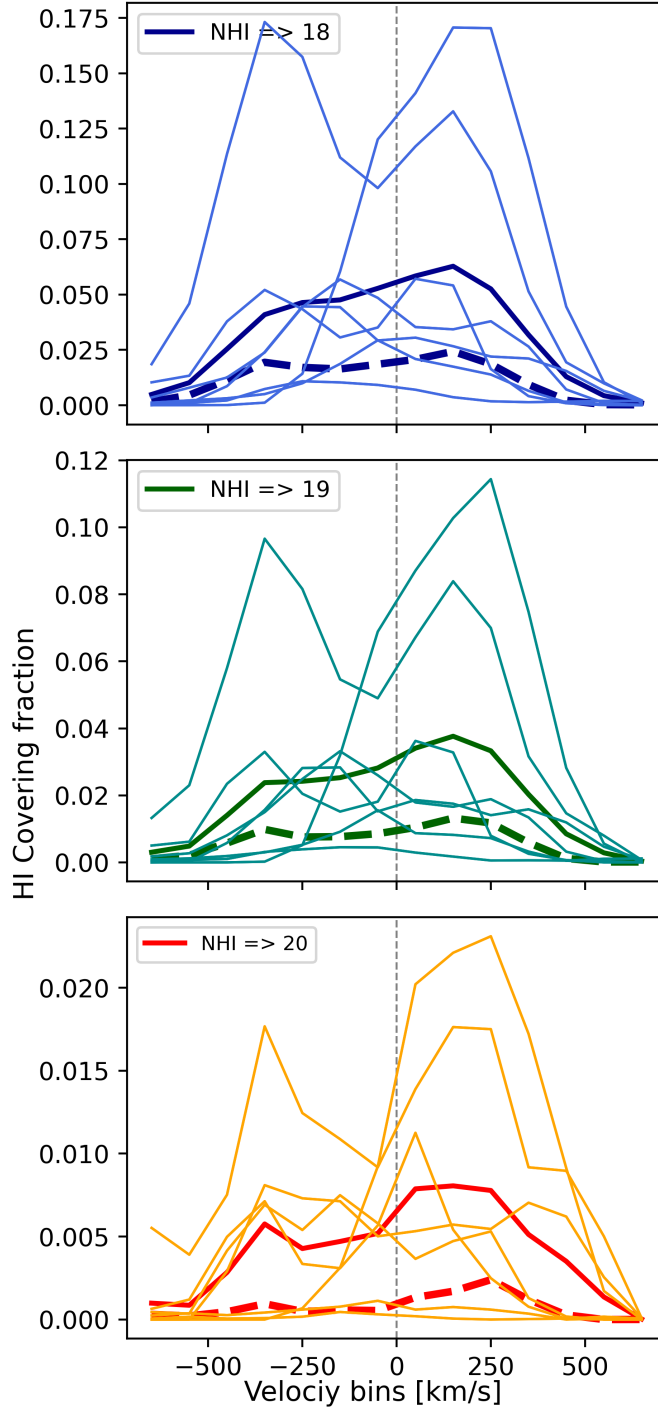


Figure 4.7.: HI cumulative covering fraction profiles of Fornax-like halos in the velocity space. The first, middle, and bottom rows show the covering fraction for HI column densities $N_{HI} \geq 18, 19$ and 20 , respectively. The thin lines indicate the individual halos, and the thick lines mark the average value. The thick dashed lines mark the average HI cumulative covering fraction in velocity space.

4. Distribution of atomic hydrogen in TNG50 Fornax-like galaxy clusters

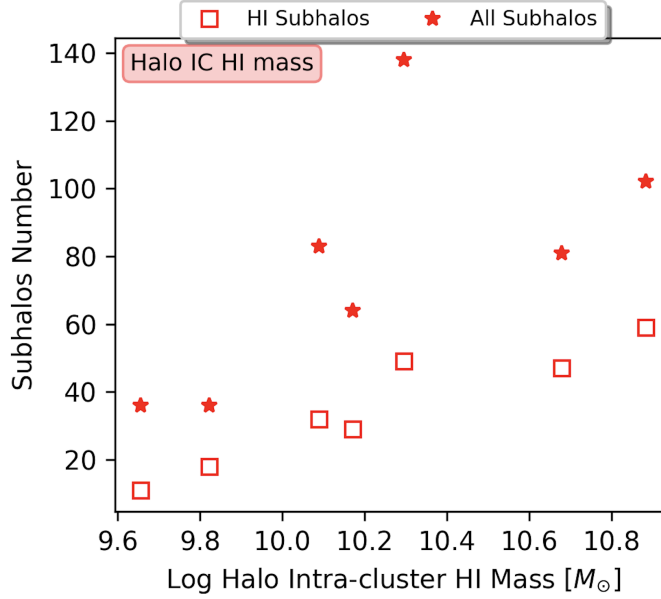


Figure 4.8.: Number of satellites as a function of intra-cluster HI mass

Voort et al. (2019) result.

4.4.2 Detection of HI clouds in the Intra-cluster region through observational work

For all the TNG50 Fornax-like halos, we found that HI clouds can be found outside 0.5 virial radius, corresponding to an average physical scale of around 300 kpc. Although only a few, there are observational studies showing the existence of remote HI clouds associated with galaxies. An important example is the detection of HI clouds in the inter-galactic medium of the galaxy group HCG44, where the HI clouds extend to more than ~ 300 kpc (Serra et al., 2013a). Another example is the case of NGC 4532, where the HI tail of the galaxy with some discrete clouds extends to 500 kpc and constitutes around 10% of the total HI mass (Koopmann, 2007).

Most recently, using the MeerKAT observations of the Fornax-A group, Kleiner et al. (2021) reported the detection of HI clouds at ~ 220 kpc from NGC 1316, the central galaxy of Fornax A, a subgroup of the Fornax cluster. Although observational support of detecting HI clouds in the IC regions around galaxies are few and rare, our and other simulation work like that of Rahmati et al. (2015); van de Voort et al. (2019); Nelson et al. (2020) strongly suggest the existence of dense small HI clumps within the CGM medium. In our work we find that within the IC region, the HI clouds have a column density $N_{HI} \sim 19$ or less, and current observations are not that sensitive. It will be really interesting to see what MFS will observe in the Fornax cluster and what is the fraction of cold gas in the IC region.

4.4.3 Possible Origin Scenario

A detailed study about the origin or production of a large amount of HI gas in TNG50 Fornax-like halos is beyond the scope of this work. However, we speculate here on a possible scenario. Recently, [Nelson et al. \(2020\)](#) studied the cold gas distribution in TNG50 massive halos at intermediate redshift $z \sim 0.5$. Using Lagrangian tracer analysis, they showed that cold gas in TNG50 halos is produced by stripped gas, either due to ram pressure stripping (RPS) or tidal stripping. These gas clouds can later stimulate the cooling process leading to a significant amount of cold gas. We checked if we could see any correlation between the satellite galaxies' number with the total IC HI mass. Figure 4.8 shows the satellite number as function of IC HI mass. We find that the number of satellites with HI gas increases with halo IC HI mass. This suggests that the HI mass in the IC regions of Fornax-like clusters could be associated with the stripped HI gas from satellite galaxies, similar to the findings of [Nelson et al. \(2020\)](#).

4.5 Summary and Conclusion

In this paper, utilizing the publically available TNG50 simulation data, we have studied the distribution of HI gas in the halos similar to the Fornax galaxy cluster. Adopting the MFS observational constraints, we have measured the HI covering fraction of the halos with a mass of $10^{13.5} \leq M_{200} \leq 10^{14} M_{\odot}$. The following points summarise our findings and conclusion:

- 1) Atomic hydrogen in TNG50 Fornax-like halos shows a wide spatial distribution, visualized as clouds and filamentary structures. The HI gas is non-uniformly distributed and extends beyond 0.5 virial radii of the central galaxy. On a physical scale, this corresponds to ~ 250 kpc.
- 2) Using our HI covering fraction measurements on the simulations, we predict the upcoming MFS should observe a HI covering fraction of 10 ± 5 % at 0.5 virial radii at HI column density $N_{HI} \geq 19$.
- 3) IC regions in Fornax-like halos hold a substantial fraction of HI. After removing the HI gas bounded to galaxies out to $10 \times R_{1/2}$, the HI in the IC is 1/3 of the total HI mass. In the IC region, the HI covering fraction corresponds to around 75% of the total HI covering fraction.
- 4) We find that the number of satellite galaxies with HI increases with increasing HI mass in the IC region. This suggests that HI in the IC regions is associated with the stripped gas of satellite galaxies, similar to the results of [Nelson et al. \(2020\)](#).

With this work, we have demonstrated by using TNG50 data that HI cold gas can co-exist and survive in the hot-intra cluster medium for the Fornax-like clusters. We plan to perform a future follow-up study to pinpoint the origin of these HI clouds, whether they are possibly stripped or in situ formed in the cluster environment.

5 | Summary and conclusions

In the current standard hierarchical structure formation scenario, galaxy clusters are the largest gravitationally bound objects in the Universe. Their assembly is driven by early mergers of massive galaxies embedded in big DM halos and sequential accretion of galaxy groups. During their growth, various physical processes act on infalling cluster galaxies, like ram pressure stripping and tidal forces, which all contribute in shaping their luminous and dark matter content. These processes leave dynamical imprints in their outer halos as well as in intra-cluster regions where dynamical timescales are long. Therefore, stellar halos are crucial in understanding the formation and evolution of galaxies. However, since the stellar light becomes fainter in the galaxy's outskirts, it is challenging to obtain any spectroscopic and hence kinematical properties. In this regard, discrete tracers such as globular clusters play an important role in learning about the galaxy halo.

Globular clusters (GCs) are bright and compact tracers which are observable to the tens of effective radii of a galaxy. They provide a opportunity to learn about the mass-assembly history of the galaxies. GCs exist in two major subclasses:- red (metal-rich) GCs and blue (metal-poor) GCs. The red GCs are found to have radial number density profiles similar to the integrated light of their host galaxies, while blue GCs are spatially more extended into the intergalactic and intra-cluster regions and trace the metal-poor component of the stellar halos. These properties of GCs make them excellent kinematic tracers to perform the mass modelling of individual galaxies and galaxy clusters.

Mass-modelling work of the nearby Hydra I galaxy cluster and other systems have shown that ignoring the presence of substructures, which are generated by accretion and merger events, could impact the dynamical mass estimates (Old et al., 2017; Hilker et al., 2018; Tucker et al., 2020). Therefore, properly identifying and including the substructures in the mass modelling is crucial to determine the mass estimate of a galaxy cluster. In this thesis, I have studied the mass assembly of the Fornax cluster using its GCs as a kinematical tracer to explore its baryonic and DM distribution.

The Fornax cluster is one of the most massive galaxy over-density and a dynamically evolving system. It provides a unique opportunity to study the growth of galaxies and intracluster light in a dense environment in great detail. Various photometric studies (Iodice et al., 2016, 2019) of the Fornax cluster have detected the presence of substructures in the form of faint stellar light between its central galaxy, NGC 1399 and neighbouring galaxies. Thanks to its proximity and building on ancillary data, the Fornax cluster offers a unique opportunity to map its complex kinematics from the core to its half virial radii (~ 350 kpc).

5. Summary and conclusions

In this thesis, I kinematically characterize the GCs population within the core and intra-cluster region of the Fornax cluster. I have studied the phase space distribution of GCs in Fornax and have explored the properties of intra-cluster globular clusters (ICGCs). With the final goal of understanding the baryonic and DM profile of the Fornax cluster, I used the GCs radial velocity catalogue to perform modelling of the Fornax using the Spherical Jeans modelling technique. In addition, I investigated the role of ICGCs in dynamical modelling. To explore the intra-cluster medium of Fornax-like halos, I studied the distribution of HI in TNG50 halos similar to the Fornax-like cluster.

In the following, I summarise the key results and conclusion of this thesis. This also answers the questions raised in Sect. 1.5 as the motivation of this thesis:

GC system of the Fornax cluster: In chapter 2, I studied the GC system of the Fornax cluster. I re-analyzed the VLT/VIMOS data of GCs within the central one square degree of the Fornax cluster, previously, analyzed by [Pota et al. \(2018\)](#); however, due to technical limitations, they recovered a lower fraction of GCs. I used the improved ESO-VIMOS reflex pipeline to reduce the data. I used pPXF, a python implemented tool to measure the radial velocities of GCs over the full spectral fitting range. I confirmed the detection of a total of 777 GCs, which led to double the number of GCs detected on the same dataset in previous work. Together with the previous literature measurements, I produced the most extensive GCs radial velocity catalogue of 2341 objects in Fornax.

The phase space distribution of the red (metal-rich) GC, showed that most of them are bound to the major galaxies in the Fornax. In contrast, blue GCs are spatially extended and occupy the outer halos of the galaxies. The radial velocity map of the full GCs sample provided the spectroscopic and first kinematical characterization of the ICGCs. The different overdense regions are marked by streams of higher radial velocity GCs, giving evidence of the interaction between the central NGCC1399 and other cluster member galaxies. In addition, Fornax's substructures and intra-cluster region are dominated mainly by blue GCs.

Role of substructures in dynamical mass-modelling of NGC1399: In chapter 3, I used the GCs radial velocity catalogue produced in chapter 2 to perform the mass-modelling of NGC 1399 out to 200 kpc. I solved spherical non-rotating Jeans equations to derive the projected dispersion and kurtosis of the observed GCs to obtain the total mass of NGC 1399. Considering the red and blue GCs subpopulations allowed me to perform a two-component tracer modelling, thus reducing the mass-anisotropy degeneracy. To investigate the effect of ICGCs on mass modelling, I defined two kinematic samples of GCs selected based on the phase-space and velocity cuts. The first *inner* sample is limited to $2 r_{\text{eff}}$, and the second *full* sample extends to $6.5 r_{\text{eff}}$.

I find that both NFW (cusp) and Burkert (core) DM halos can reproduce the observed GCs kinematics well. The total mass from NFW and Burkert halos for *inner* and sample agrees within one σ uncertainty. For the *full* sample, I find that independent of the DM halo used, both profiles result in a M_{200} value that is in close agreement for both profiles. The virial mass for the *full* sample for the Burkert halo is $\log(M) = 13.42 \pm 0.45 M_{\odot}$, and for the NFW halo it is $\log(M) = 13.62 \pm 0.58 M_{\odot}$. The DM halo parameters for the *full* sample of GCs is well constrained, resulting in obtaining a similar enclosed mass profile from

both NFW and Burkert halo. This suggests that ICGCs trace the cluster potential and are essential to consider to obtain the total mass estimate. Lastly, I found that independent of the DM halo used, blue GCs show mild radial anisotropy with increasing radius consistent with recent simulation work pointing to an accreted nature of blue GCs.

Intra-cluster medium of Fornax-like halos: Finally, in chapter 4, I studied the intra-cluster medium of galaxy clusters similar to the Fornax cluster. Utilizing the publically available TNG50 cosmological simulation and adopting the MFS survey observing criteria, I investigated the distribution of HI in Fornax-like galaxy clusters in the TNG50 halos. For that, I applied the virial mass selection criterium of $10^{13.50} \leq M_{200} \leq 10^{14} M_{\odot}$ to find seven Fornax-like clusters in the TNG50 simulation at snapshot 99 ($z \sim 0$).

The TNG50 halos show a wide variety of atomic hydrogen distribution, visualized as HI clouds and filamentary structures. HI is non-uniformly distributed and extends beyond 0.5 virial radii (~ 250 kpc) of the central galaxy. Using the measured HI covering fraction, I predict the MFS should observe a HI covering fraction of $10 \pm 5\%$ at 0.5 virial radii at HI column density $N_{HI} \geq 19$. The HI distribution in the IC regions of the halos corresponds to around 75 % of the total HI covering fraction, suggesting that a significant fraction of HI gas in TNG50 halos actually consists of IC HI gas.

In conclusion, my thesis has expanded our knowledge about the GC system of the Fornax cluster and its importance in dynamical mass-modelling work. The detection of ICGCs streams in Fornax provides the first kinematical evidence of interactions between the central galaxy NGC 1399 and other major galaxies. My work demonstrates that substructures and ICGCs are essential to be considered in the dynamical mass-modelling work and could impact the total estimated mass. The presence of a large amount of cold gas in Fornax-like halos in the TNG50 simulations suggests that cold gas can co-exist and survive in the hot-IC medium. It will be intriguing to see what MFS will observe within the Fornax cluster. With its capability and high sensitivity, MeerKAT will provide observational constraints on the predictions from current simulations.

6 | Outlook

In this thesis, I explored the Fornax cluster’s mass assembly using its globular cluster system. In addition, I have shown via the TNG50 cosmological simulation that galaxy clusters similar to Fornax can host a significant amount of cold gas. There remain many open questions to investigate and understand in terms of adequately comprehending the mass assembly of the Fornax and other nearby galaxy clusters. The broader and bigger questions which need to be addressed in future are: what are the nature and the exact origin of the intra-cluster GCs? How can we quantify the role of substructures in the mass-modelling? Will the MFS survey observe a large quantity of cold HI gas in the Fornax cluster, thereby supporting predictions from current simulations. If so, a follow-up question would be how cold gas could survive and exist in the cluster environment?

In the following, I present some future projects that are extensions and follow-up research projects based on my thesis work.

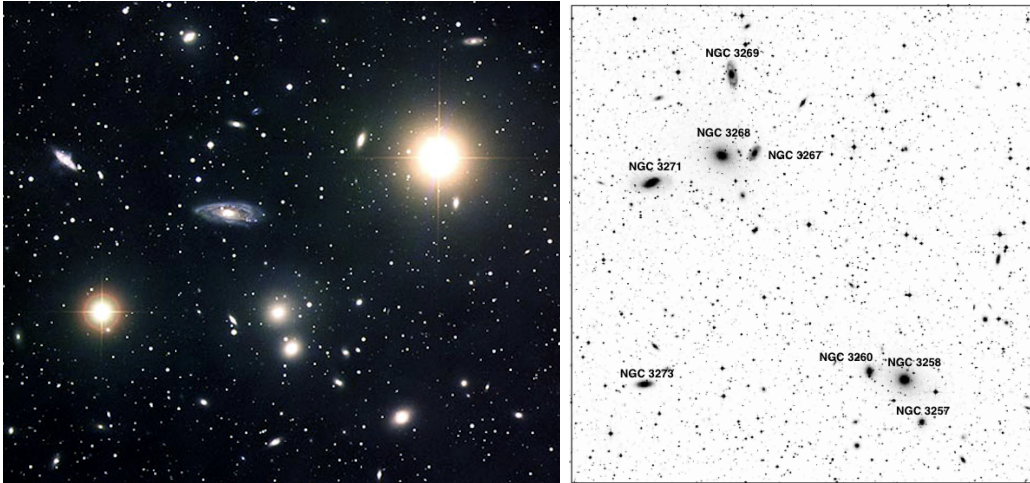


Figure 6.1.: Images of the Hydra I (left) and Antlia (right) clusters showing their major galaxies (credit: ESO)

While the Fornax cluster acts as the ideal test bench for studying the mass-assembly process, it is essential to investigate other nearby galaxy clusters to comprehend the mass assembly of clusters on a statistical basis. In my subsequent work, I aim to provide the first quantitative exploration of how substructures impact the mass modelling of different galaxy clusters. One of the primary goals will be to characterize the DM profile within the core of

6. Outlook

galaxy clusters and compare it with cosmological models. Another goal will be to obtain accurate dynamical mass measurements out to large cluster-centric distances to infer the luminous and DM distributions of different galaxy clusters.

I aim to extend my study of galaxy clusters beyond Fornax to other nearby clusters such as Hydra I and Antlia. It has been shown that diffuse ICL and stellar streams exist in these clusters, as seen in deep photometry between their central and neighbouring galaxies (Iodice et al., 2016; Arnaboldi et al., 2012b). In contrast to the Virgo and Coma clusters, these galaxy clusters are less explored and present a wide range of different IC features. Antlia (distance ~ 35 Mpc) is in a merging state of two subgroups dominated by giant galaxies (Bassino et al., 2006), whereas Hydra I (distance ~ 50 Mpc) is dominated by a massive central galaxy (NGC 3311). Due to their close distance, the GC systems of these galaxy clusters are readily observable with current VLT instruments, like FORS2 and MUSE.

6.1 Substructures in nearby galaxy clusters

This project will aim to identify and kinematically characterize the substructures of galaxy clusters and look for disturbances and interactions of IC populations within the outer halo kinematics of major galaxies. Using the novel algorithm developed by Gatto et al. (2020) I intend to identify the cold substructures in the phase-space of the Fornax cluster. To fulfil the goals of this project, I will utilize my own approved observing programmes done with FLAMES and FORS2 at ESO-VLT. They focus on obtaining spectroscopy of GCs in substructures and in the outer halos of individual galaxies (see fig. 6.2). Currently, these observations are underway and expected to be fully completed within 2023.

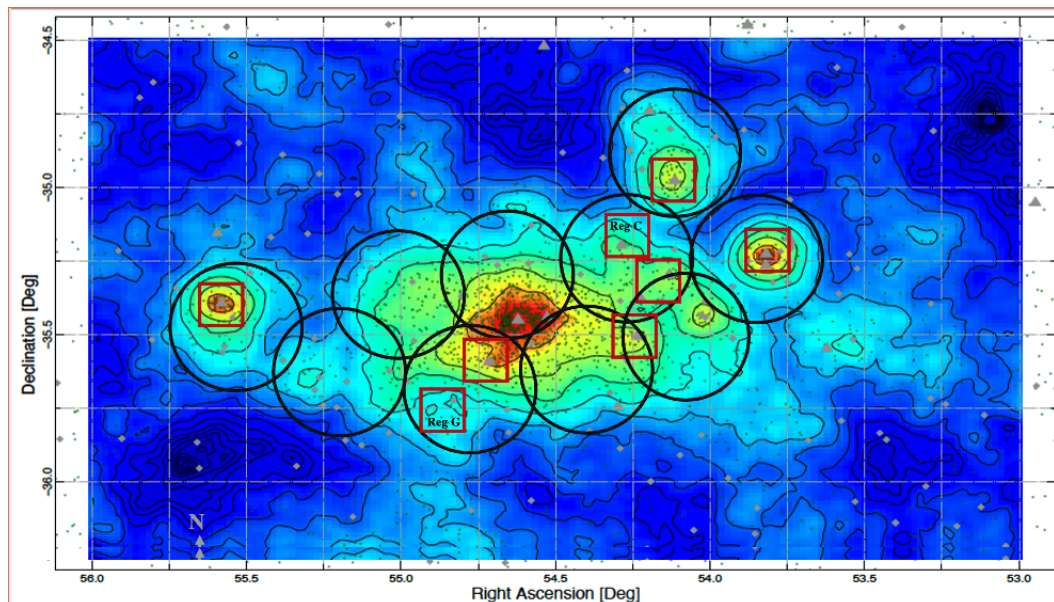


Figure 6.2.: FLAMES (black circles) and FORS2 pointings (red squares) over the surface density map of GCs tracing the Fornax substructures.

6.2. Dynamical mass-modeling to infer the luminous and DM distributions

The upcoming FLAMES observations will have a spectral resolution sufficient to measure the metallicity-sensitive Calcium triplet (Foster et al., 2009, 2010). This will be a novel approach to measure GC metallicities in the IC regions of nearby galaxy clusters and will be crucial to constrain formation scenarios of intra-cluster GCs (Brodie & Strader, 2006).

I will use established full spectrum fitting routines (Cappellari & Emsellem, 2004; Cappellari et al., 2013) to measure the radial velocities of GCs. Additionally, I will measure the stellar population properties, such as the metallicity of the GCs in substructure regions. For the Hydra I and Antlia clusters, I will use archival ESO and Hubble Space Telescope data sets to photometrically detect GC streams in their IC regions around the central cluster galaxies.

6.2 Dynamical mass-modeling to infer the luminous and DM distributions

With my PhD work, I have laid the ground work required to understand the impact of substructures in the mass-modeling of the Fornax cluster. My work has shown that we are currently missing a substantial amount of GCs to identify and fully characterise the substructures in the cluster. However, the upcoming FLAMES data will change this and will fully characterise the substructures in the cluster. I will use an advanced chemo-dynamical and orbit-based super-position modelling approach (Zhu et al., 2016a,b), which will allow me to use the combined information of potential tracers properties, such as radial velocity, position, metallicity. The inclusion of GCs kinematics from the outer regions of the Fornax cluster and the inner stellar kinematics of NGC 1399 from the archival MUSE data will provide a better constraint on the inner slope of DM halo, resolving the tension with cosmological simulations (Newman et al., 2013).

6.3 Role of cluster environment on galaxy evolution

Dwarf galaxies are considered as building blocks in standard cosmology. However, the low surface brightness of most dwarf galaxies prevents us from studying them in detail. The shallow gravitational potentials of low-mass galaxies make them particularly susceptible to morphological transformation and disruption processes. Hence, low-mass galaxies offer a unique laboratory to explore the processes that shape galaxies. My work on the Fornax cluster has shown that metal-poor GCs mostly dominate its intra-cluster region, with similar metallicities as metal-poor dwarf galaxies (Peng et al., 2006; Brodie & Strader, 2006).

Metal-poor ICGCs are often considered to have originated from stripped/disrupted dwarf galaxies, and studying them in correlation with still-present dwarf galaxies, could unveil the mechanism leading to the build-up of the ICGC population. For this project, I will use the available dwarf galaxies catalogue of the Fornax cluster (Venhola et al., 2020) in synergy with my VIMOS and newly available FLAMES GCs catalogue to look for phase-space, colour and metallicity correlations between GCs and dwarf galaxies. This part of the project will be

6. Outlook

essential to characterize the impact of the cluster environment on the evolution of low-mass galaxies.

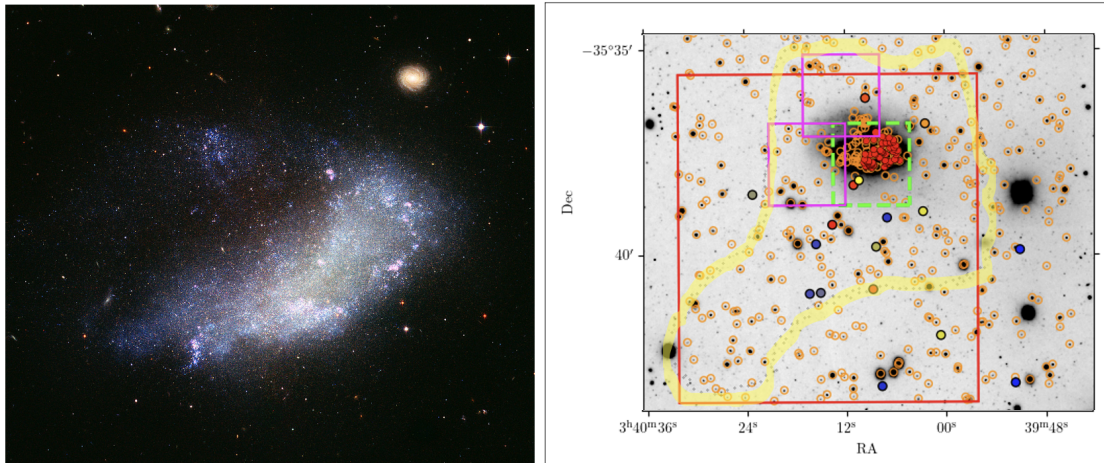


Figure 6.3.: Left: A color composite image of NGC 1427A (credit: ESO). Right: Approved MUSE (pink square) and FORS2 (red square) observations of NGC 1427A. The dashed square indicates archival MUSE observations.

In particular, one very interesting system is the irregular galaxy NGC 1427A in the Fornax cluster. NGC 1427A (distance ~ 20 Mpc, $M_* \sim 6 \times 10^9 M_\odot$) is a bright arrow-shaped dwarf irregular galaxy presently infalling toward or crossing the core of the Fornax cluster. It has been the focus of various studies due to its highly peculiar shape (left panel in fig. 6.2). It is unclear whether its morphology is the result of tidal interaction, ram pressure stripping, or an ongoing merger with an even smaller dwarf galaxy. To understand the peculiar morphology of NGC 1427A, we acquired MUSE and FORS2 observations to cover the full extent of the stellar body of NGC 1427A and the northern object (right panel in fig. 6.2). These observations will give us a complete view of NGC 1427A's stellar, star cluster and ionized gas content.

These research projects will advance our understanding of the mass-assembly process of nearby galaxy clusters, providing information about their formation and evolution mechanisms. With this future work, I will examine the nature of the DM profile within the cluster core, which will help resolve issues with different cosmological models. My work will be the first quantified study to explore the impact and contribution of substructures on the mass budget of galaxy clusters. This will be exemplary for considering the substructures to the total mass estimates of galaxy clusters at higher redshifts, where substructure detection is not possible yet. My work will produce the most extended sample of extra-galactic globular clusters in the Fornax, Hydra I and Antlia galaxy clusters, setting a benchmark for future GCs surveys for higher redshift galaxy clusters.

A | Appendix of Chapter 2

A.1 Test regarding pPXF parameter choices

Effect of initial velocity guesses on the resulting pPXF radial velocity: To determine how strongly the pPXF initial radial velocity guess can affect the resulting radial velocity, we fitted a few spectra with varying initial velocity guesses ranging between 800 and 1800 km s^{-1} with a step of 200 km s^{-1} . The figure shows three example spectra at S/N=6, 12, and 17. The resulting radial velocities are mostly consistent, and the variations are less than 5%, which is smaller than the individual velocity measurement errors.

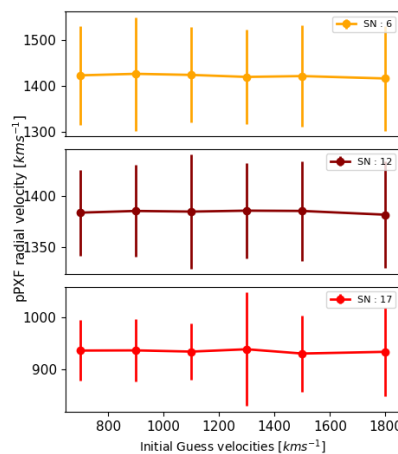


Figure A.1.: Effect of initial radial velocity guesses on the resulting radial velocity measurements.

Variation in the derived radial velocity and velocity dispersion as a function of the polynomial degree: Here we present the results of tests mentioned in sect. 2.3.1. For GCs for which we obtained a radial velocity consistent with the Fornax cluster ($450 < v < 2500 \text{ km s}^{-1}$), but a velocity dispersion higher than 20 km s^{-1} , we varied the additive and multiplicative polynomials to quantify the effect on the derived radial velocity and velocity dispersion. Based on consistent values of radial velocity and dispersion, we selected the additive and multiplicative polynomials. In figure A.2 we show the radial velocity (left) and velocity dispersion (right) measured for one spectrum, on a grid of additive and multiplicative

A. Appendix of Chapter 2

polynomials with orders in between 0 and 6. These plots show that the radial velocity remains quite consistent for additive polynomials with orders of 2 to 5 and multiplicative polynomial with orders in between 2 and 5. At the same time, the velocity dispersion remains lower than 20 km s^{-1} within this polynomial range.

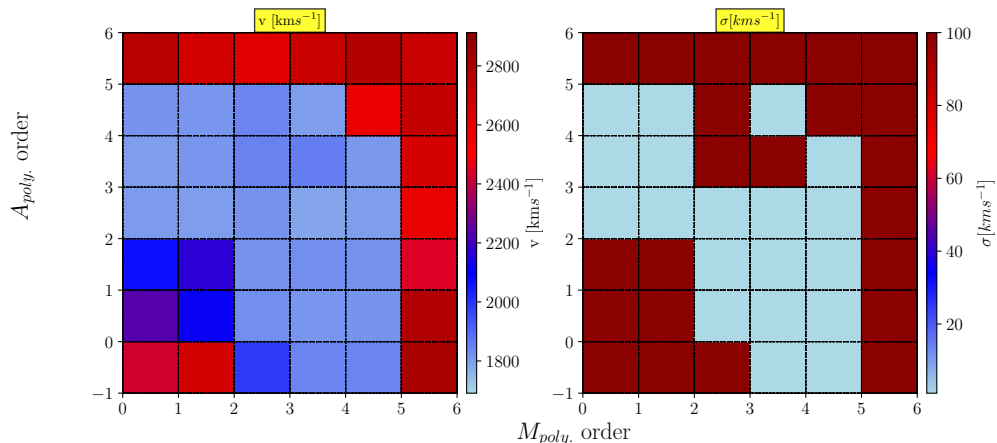


Figure A.2.: Choosing pPXF polynomials. Derived radial velocity (left panel) and the velocity dispersion (right panel) for a GC spectrum of $S/N \sim 5$ as a function of additive and multiplicative polynomial degree. Assigning to the additive polynomial a grade equal to -1 means running pPXF without it, i.e. using only multiplicative polynomials.

Effect of higher-order pPXF polynomials on radial velocity: To quantify the effect of higher-order polynomials on the inferred radial velocities as well as using only additive polynomials, as is often done when fitting stellar kinematics, we used five sets of additive and multiplicative polynomials denoted as [additive, multiplicative] : [3,5] (our choice), [5,0], [10,0], [15,0], [10,10], [15,15]. The measured radial velocities from pPXF for these sets of polynomials for spectra of three different S/N are shown in figure A.3. The derived radial velocities are always consistent and show only slight variations, which are within 5%.

A.1. Test regarding pPXF parameter choices

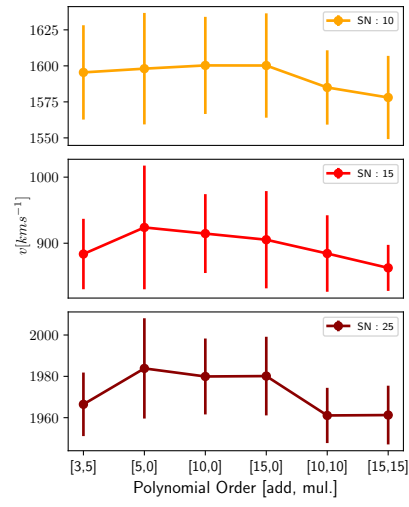


Figure A.3.: Effect of higher order polynomials on radial velocity measurements.

A.2 Example of a GC portfolio

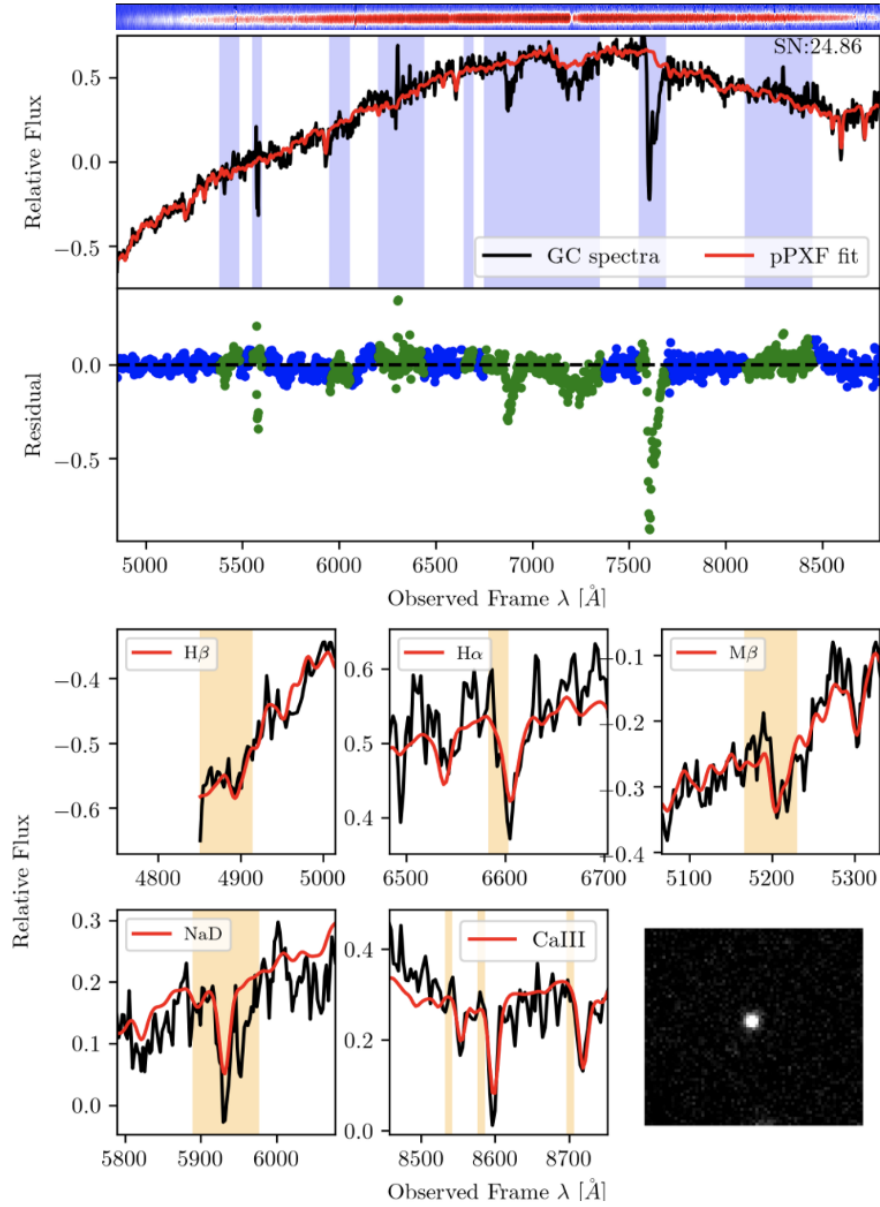


Figure A.4.: Example of a GC portfolio. The top panel shows the 1D extracted spectrum from the 2D VIMOS observation (on top). The middle panel shows the pPXF fit and its residuals in the subplot. The lower panel shows zoom-in wavelengths regions of absorption features used to visually select bonafide GCs. The lower right subpanel shows the 2D image of the GC from pre-imaging.

A.3 Catalogue of VIMOS dataset GCs

Table A.3 shows an overview of our VIMOS data GC radial velocity catalogue. Together with the A and B class objects, we also included class C objects in the catalogue, totalling 851 GCs (see the sect. 3.4 for details.) For each GC, we provide its measured radial velocity and its uncertainty, S/N, and object class (A, B, and C). We also give the magnitude information for each GC in $g, r, i,$ and u band obtained from the matched FDS photometric catalogue presented by [Cantiello et al. \(2020\)](#).

Table A.1.: Excerpt of our VIMOS GCs catalogue.

Point Name (1)	FVSS-GC-ID (2)	R.A. (J2000) (3)	Dec.(J2000) (4)	v [km s ⁻¹] (5)	Δv [km s ⁻¹] (6)	S/N (7)	Object Class (8)
fnx01_q1_ext1_4_slit_73	FVSSIIIGC:033903.86-352428.66	54.766100	-35.407960	1948.80	14.74	25.39	A
fnx01_q1_ext1_9_slit_214	FVSSIIIGC:033859.41-352129.81	54.747550	-35.358280	799.97	88.59	15.03	A
fnx01_q1_ext1_10_slit_201	FVSSIIIGC:033857.80-352112.35	54.740820	-35.353430	1675.47	152.62	13.57	A
fnx01_q1_ext1_12_slit_59	FVSSIIIGC:033856.18-352449.00	54.734090	-35.413610	681.64	59.39	15.45	A

ID (FDS) (9)	R.A. (J2000) (FDS) (10)	Dec. (J2000) (FDS) (11)	g [mag] (12)	Δg [mag] (13)	r [mag] (14)	Δr [mag] (15)
FDSJ033903.86-352428.64	54.766102	-35.407955	21.704	0.014	20.959	0.014
FDSJ033859.41-352129.71	54.747524	-35.358253	22.223	0.015	21.53	0.017
FDSJ033857.80-352112.32	54.740826	-35.353424	22.244	0.017	21.636	0.016
FDSJ033856.18-352448.90	54.734097	-35.413582	20.651	0.016	19.958	0.013

i [mag] (16)	Δi [mag] (17)	u [mag] (18)	Δu [mag] (19)
20.566	0.013	23.558	0.094
21.530	0.017	21.287	0.087
21.375	0.024	23.276	0.074
19.707	0.012	21.975	0.031

Notes. Column list:(1) GC named as in the VIMOS pointing id; (2) CGs named as in the FVSS ID (FVSSIIIGC:RA-DEC); (3) right ascension; (4) declination; (5) GC radial velocity; (6) radial velocity uncertainty; (7) spectral S/N; (8) GC object class; (9) FDS ID (10) right ascension (FDS); (11) declination (FDS); (12-13) g -band magnitude with error; (14-15) r -band magnitude and its error; (16-17) i -band magnitude and its error; (18-19) u -band magnitude and its error.

References

- Agnello, A., Evans, N. W., Romanowsky, A. J., & Brodie, J. P. 2014, *Monthly Notices of the Royal Astronomical Society*, 442, 3299
- Alamo-Martínez, K. A., Blakeslee, J. P., Jee, M. J., et al. 2013, *The Astrophysical Journal*, 775, 20
- Allen, S. W., Evrard, A. E., & Mantz, A. B. 2011, *Annual Review of Astronomy and Astrophysics*, 49, 409, [_eprint: https://doi.org/10.1146/annurev-astro-081710-102514](https://doi.org/10.1146/annurev-astro-081710-102514)
- Anand, A., Kauffmann, G., & Nelson, D. 2022, *Monthly Notices of the Royal Astronomical Society*, 513, 3210
- Anand, A., Nelson, D., & Kauffmann, G. 2021, *Monthly Notices of the Royal Astronomical Society*, 504, 65
- Angora, G., Brescia, M., Caviuoti, S., et al. 2019, *MNRAS*, 490, 4080
- Arnaboldi, M., Ventimiglia, G., Iodice, E., Gerhard, O., & Coccato, L. 2012a, *A&A*, 545, A37
- Arnaboldi, M., Ventimiglia, G., Iodice, E., Gerhard, O., & Coccato, L. 2012b, *A&A*, 545, A37
- Ashman, K. M. & Zepf, S. E. 1992, *ApJ*, 384, 50
- Bacon, R., Copin, Y., Monnet, G., et al. 2001, *MNRAS*, 326, 23
- Bassino, L. P., Richtler, T., & Dirsch, B. 2006, *MNRAS*, 367, 156
- Bekki, K., Forbes, D. A., Beasley, M. A., & Couch, W. J. 2003, *MNRAS*, 344, 1334
- Berg, M. A., Howk, J. C., Lehner, N., et al. 2019, *The Astrophysical Journal*, 883, 5
- Bergond, G., Athanassoula, E., Leon, S., et al. 2007, *A&A*, 464, L21
- Bílek, M., Duc, P.-A., Cuillandre, J.-C., et al. 2020, *MNRAS*, 498, 2138
- Binney, J. & Tremaine, S. 1987, *Galactic dynamics*
- Binney, J. & Tremaine, S. 2008, *Galactic Dynamics: Second Edition*
- Blaña Díaz, M., Gerhard, O., Wegg, C., et al. 2018, *MNRAS*, 481, 3210
- Blakeslee, J. P., Jordán, A., Mei, S., et al. 2009, *ApJ*, 694, 556
- Blumenthal, G. R., Faber, S. M., Flores, R., & Primack, J. R. 1986, *ApJ*, 301, 27
- Boselli, A. & Gavazzi, G. 2006, *PASP*, 118, 517

References

- Boselli, A. & Gavazzi, G. 2014, *A&A Rev.*, 22, 74
- Brodie, J. P. & Strader, J. 2006, *Annual Review of Astronomy and Astrophysics*, 44, 193
- Bullock, J. S. & Johnston, K. V. 2005, *ApJ*, 635, 931
- Bullock, J. S., Kolatt, T. S., Sigad, Y., et al. 2001, *MNRAS*, 321, 559
- Burkert, A. 1995, *ApJ*, 447, L25
- Bykov, A. M., Churazov, E. M., Ferrari, C., et al. 2015, *Space Sci. Rev.*, 188, 141
- Cantiello, M., Blakeslee, J. P., Raimondo, G., et al. 2014, *A&A*, 564, L3
- Cantiello, M., D'Abrusco, R., Spavone, M., et al. 2018, *A&A*, 611, A93
- Cantiello, M., Venhola, A., Grado, A., et al. 2020, *A&A*, 639, A136
- Cappellari, M. 2016, *Annual Review of Astronomy and Astrophysics*, 54, 597, [_eprint: https://doi.org/10.1146/annurev-astro-082214-122432](https://doi.org/10.1146/annurev-astro-082214-122432)
- Cappellari, M. 2017, *MNRAS*, 466, 798
- Cappellari, M. & Emsellem, E. 2004, *PASP*, 116, 138
- Cappellari, M., Emsellem, E., Krajnović, D., et al. 2011, *MNRAS*, 413, 813
- Cappellari, M., McDermid, R. M., Alatalo, K., et al. 2013, *MNRAS*, 432, 1862
- Chaturvedi, A., Hilker, M., Cantiello, M., et al. 2022, *Astronomy & Astrophysics*, 657, A93
- Chen, H.-W., Zahedy, F. S., Johnson, S. D., et al. 2018, *Monthly Notices of the Royal Astronomical Society*, 479, 2547
- Chilingarian, I. V., Mieske, S., Hilker, M., & Infante, L. 2011, *MNRAS*, 412, 1627
- Churazov, E., Tremaine, S., Forman, W., et al. 2010, *MNRAS*, 404, 1165
- Cleveland, W. S. 1979, *Journal of the American Statistical Association*, 74, 829
- Cleveland, W. S. & Devlin, S. J. 1988, *Journal of the American Statistical Association*, 83, 596
- Cocato, L., Arnaboldi, M., & Gerhard, O. 2013, *MNRAS*, 436, 1322
- Cocato, L., Gerhard, O., Arnaboldi, M., et al. 2009, *MNRAS*, 394, 1249
- Conroy, C., Wechsler, R. H., & Kravtsov, A. V. 2007, *ApJ*, 668, 826
- Cooper, A. P., D'Souza, R., Kauffmann, G., et al. 2013, *Monthly Notices of the Royal Astronomical Society*, 434, 3348
- Cooper, A. P., Gao, L., Guo, Q., et al. 2015, *Monthly Notices of the Royal Astronomical Society*, 451, 2703
- Côté, P., Blakeslee, J. P., Ferrarese, L., et al. 2004, *ApJS*, 153, 223
- Côté, P., Marzke, R. O., & West, M. J. 1998, *ApJ*, 501, 554
- Côté, P., McLaughlin, D. E., Hanes, D. A., et al. 2001, *ApJ*, 559, 828
- D'Abrusco, R., Cantiello, M., Paolillo, M., et al. 2016, *ApJ*, 819, L31
- Davis, M., Efstathiou, G., Frenk, C. S., & White, S. D. M. 1985, *ApJ*, 292, 371

- Davé, R., Crain, R. A., Stevens, A. R. H., et al. 2020, *Monthly Notices of the Royal Astronomical Society*, 497, 146
- de Zeeuw, P. T., Bureau, M., Emsellem, E., et al. 2002, *MNRAS*, 329, 513
- Dekel, A., Devor, J., & Hetzroni, G. 2003, *MNRAS*, 341, 326
- Diemer, B. & Kravtsov, A. V. 2015, *ApJ*, 799, 108
- Diemer, B., Stevens, A. R. H., Lagos, C. d. P., et al. 2019, *MNRAS*, 487, 1529
- Dirsch, B., Richtler, T., Geisler, D., et al. 2003, *AJ*, 125, 1908
- Dirsch, B., Richtler, T., Geisler, D., et al. 2004, *AJ*, 127, 2114
- Dolag, K., Komatsu, E., & Sunyaev, R. 2016, *MNRAS*, 463, 1797
- Dolag, K., Murante, G., & Borgani, S. 2010, *MNRAS*, 405, 1544
- Dolfi, A., Forbes, D. A., Couch, W. J., et al. 2021, *MNRAS*, 504, 4923
- Douglas, N. G., Napolitano, N. R., Romanowsky, A. J., et al. 2007, *ApJ*, 664, 257
- Dressler, A. 1980, *ApJ*, 236, 351
- Drinkwater, M. J., Gregg, M. D., Hilker, M., et al. 2003, *Nature*, 423, 519
- Drinkwater, M. J., Phillipps, S., Jones, J. B., et al. 2000, *A&A*, 355, 900
- Dutton, A. A. & Macciò, A. V. 2014, *MNRAS*, 441, 3359
- Eigenthaler, P., Puzia, T. H., Taylor, M. A., et al. 2018, *ApJ*, 855, 142
- Fahrion, K., Lyubenova, M., Hilker, M., et al. 2020a, *A&A*, 637, A26
- Fahrion, K., Lyubenova, M., Hilker, M., et al. 2020b, *A&A*, 637, A27
- Fensch, J., Mieske, S., Müller-Seidnitz, J., & Hilker, M. 2014, *A&A*, 567, A105
- Fielding, D. B., Tonnesen, S., DeFelippis, D., et al. 2020, *ApJ*, 903, 32
- Firth, P., Drinkwater, M. J., Evstigneeva, E. A., et al. 2007, *MNRAS*, 382, 1342
- Forbes, D. A., Brodie, J. P., & Grillmair, C. J. 1997, *AJ*, 113, 1652
- Forbes, D. A. & Remus, R.-S. 2018, *MNRAS*, 479, 4760
- Foreman-Mackey, D., Hogg, D. W., Lang, D., & Goodman, J. 2013, *Publications of the Astronomical Society of the Pacific*, 125, 306
- Foster, C., Forbes, D. A., Proctor, R. N., et al. 2010, *AJ*, 139, 1566
- Foster, C., Proctor, R. N., Forbes, D. A., et al. 2009, *MNRAS*, 400, 2135
- Freudling, W., Romaniello, M., Bramich, D. M., et al. 2013, *A&A*, 559, A96
- Gaia Collaboration, Babusiaux, C., van Leeuwen, F., et al. 2018, *A&A*, 616, A10
- Gaia Collaboration, Prusti, T., de Bruijne, J. H. J., et al. 2016, *A&A*, 595, A1
- Gatto, M., Napolitano, N. R., Spiniello, C., Longo, G., & Paolillo, M. 2020, *A&A*, 644, A134
- Gauthier, J.-R. & Chen, H.-W. 2011, *MNRAS*, 418, 2730
- Genel, S., Vogelsberger, M., Springel, V., et al. 2014, *MNRAS*, 445, 175

References

- Gerhard, O. E. 1993, *MNRAS*, 265, 213
- Gnedin, N. Y. & Kravtsov, A. V. 2011, *ApJ*, 728, 88
- Graham, A. W., Colless, M. M., Busarello, G., Zaggia, S., & Longo, G. 1998, *A&AS*, 133, 325
- Gregg, M. D. & West, M. J. 1998, *Nature*, 396, 549
- Gunn, J. E. & Gott, J. Richard, I. 1972, *ApJ*, 176, 1
- Guth, A. H. 1981, *Physical Review D*, 23, 347
- Harris, W. E., Brown, R. A., Durrell, P. R., et al. 2020, *ApJ*, 890, 105
- Hartke, J., Arnaboldi, M., Gerhard, O., et al. 2018, *A&A*, 616, A123
- Helmi, A. 2020, *Annual Review of Astronomy and Astrophysics*, 58, 205, `_eprint: https://doi.org/10.1146/annurev-astro-032620-021917`
- Hilker, M., Barbosa, C. E., Richtler, T., et al. 2015, in *IAU Symposium*, Vol. 309, *Galaxies in 3D across the Universe*, ed. B. L. Ziegler, F. Combes, H. Dannerbauer, & M. Verdugo, 221–222
- Hilker, M., Baumgardt, H., Infante, L., et al. 2007, *A&A*, 463, 119
- Hilker, M., Infante, L., & Richtler, T. 1999a, *A&AS*, 138, 55
- Hilker, M., Infante, L., Vieira, G., Kissler-Patig, M., & Richtler, T. 1999b, *A&AS*, 134, 75
- Hilker, M., Richtler, T., Barbosa, C. E., et al. 2018, *A&A*, 619, A70
- Hubble, E. P. 1926, *ApJ*, 64, 321
- Hughes, A. K., Sand, D. J., Seth, A., et al. 2022, *New Velocity Measurements of NGC 5128 Globular Clusters out to 130 kpc: Outer Halo Kinematics, Substructure and Dynamics*, `arXiv:2208.08997 [astro-ph]`
- Ikebe, Y., Ezawa, H., Fukazawa, Y., et al. 1996, *Nature*, 379, 427
- Iodice, E., Capaccioli, M., Grado, A., et al. 2016, *ApJ*, 820, 42
- Iodice, E., Spavone, M., Capaccioli, M., et al. 2019, *A&A*, 623, A1
- Jethwa, P., Thater, S., Maindl, T., & Van de Ven, G. 2020, *DYNAMITE: DYnamics, Age and Metallicity Indicators Tracing Evolution*, *Astrophysics Source Code Library*, record `ascl:2011.007`
- Joanes, D. N. & Gill, C. A. 1998, *Journal of the Royal Statistical Society: Series D (The Statistician)*, 47, 183
- Jonas, J. & the MeerKAT Team. 2018, in *Proceedings of MeerKAT Science: On the Pathway to the SKA — PoS(MeerKAT2016)* (Stellenbosch, South Africa: Sissa Medialab), 001
- Jordán, A., Blakeslee, J. P., Côté, P., et al. 2007, *ApJS*, 169, 213
- Jordán, A., Côté, P., Ferrarese, L., et al. 2004, *ApJ*, 613, 279
- Jordán, A., Peng, E. W., Blakeslee, J. P., et al. 2009, *ApJS*, 180, 54
- Kissler-Patig, M., Grillmair, C. J., Meylan, G., et al. 1999, *AJ*, 117, 1206

- Kleiner, D., Serra, P., Maccagni, F. M., et al. 2021, *Astronomy & Astrophysics*, 648, A32
- Kluge, M., Neureiter, B., Riffeser, A., et al. 2020, *ApJS*, 247, 43
- Ko, Y., Hwang, H. S., Lee, M. G., et al. 2017, *ApJ*, 835, 212
- Koopmann, R. A. 2007, A 500 kpc HI Tail of the Virgo Pair NGC4532/DDO137 Detected by ALFALFA, arXiv:0707.3277 [astro-ph]
- Krajnović, D., Emsellem, E., Cappellari, M., et al. 2011, *MNRAS*, 414, 2923
- Kravtsov, A. V. & Borgani, S. 2012, *Annual Review of Astronomy and Astrophysics*, 50, 353, [_eprint: https://doi.org/10.1146/annurev-astro-081811-125502](https://doi.org/10.1146/annurev-astro-081811-125502)
- Kravtsov, A. V. & Gnedin, O. Y. 2005, *ApJ*, 623, 650
- Kundu, A. & Whitmore, B. C. 2001, *AJ*, 121, 2950
- Lan, T.-W. & Mo, H. 2018, *The Astrophysical Journal*, 866, 36
- Lee-Waddell, K., Serra, P., Koribalski, B., et al. 2018a, *MNRAS*, 474, 1108
- Lee-Waddell, K., Serra, P., Koribalski, B., et al. 2018b, *MNRAS*, 474, 1108
- LeFevre, O., Saisse, M., Mancini, D., et al. 2003, 4841, 1670
- Li, C., Zhu, L., Long, R. J., et al. 2020, *MNRAS*, 492, 2775
- Łokas, E. L. & Mamon, G. A. 2003, *MNRAS*, 343, 401
- Łokas, E. L., Mamon, G. A., & Prada, F. 2005, *MNRAS*, 363, 918
- Longobardi, A., Arnaboldi, M., Gerhard, O., & Mihos, J. C. 2015, *A&A*, 579, L3
- Longobardi, A., Arnaboldi, M., Gerhard, O., Pulsoni, C., & Söldner-Rembold, I. 2018a, *A&A*, 620, A111
- Longobardi, A., Peng, E. W., Côté, P., et al. 2018b, *ApJ*, 864, 36
- Madrid, J. P., O’Neill, C. R., Gagliano, A. T., & Marvil, J. R. 2018, *ApJ*, 867, 144
- Mamon, G. A. & Łokas, E. L. 2005, *MNRAS*, 363, 705
- Mancillas, B., Duc, P.-A., Combes, F., et al. 2019, *A&A*, 632, A122
- Marinacci, F., Vogelsberger, M., Pakmor, R., et al. 2018, *MNRAS*, 480, 5113
- Marini, I., Borgani, S., Saro, A., et al. 2022, *MNRAS*, 514, 3082
- McNeil, E. K., Arnaboldi, M., Freeman, K. C., et al. 2010, *A&A*, 518, A44
- Mehrgan, K., Thomas, J., Saglia, R., et al. 2019, *ApJ*, 887, 195
- Mei, S., Blakeslee, J. P., Côté, P., et al. 2007, *ApJ*, 655, 144
- Merritt, D. 1985, *AJ*, 90, 1027
- Mieske, S., Hilker, M., Bomans, D. J., et al. 2008, *A&A*, 489, 1023
- Mieske, S., Hilker, M., & Infante, L. 2002, *A&A*, 383, 823
- Mieske, S., Jordán, A., Côté, P., et al. 2010, *ApJ*, 710, 1672
- Mihos, J. C., Harding, P., Feldmeier, J., & Morrison, H. 2005, *The Astrophysical Journal*, 631, L41

References

- Mo, H., van den Bosch, F. C., & White, S. 2010, *Galaxy Formation and Evolution*
- Montes, M. 2022, The faint light in groups and clusters of galaxies, arXiv:2203.06199 [astro-ph]
- Montes, M. & Trujillo, I. 2014, *ApJ*, 794, 137
- Montes, M. & Trujillo, I. 2018, *Monthly Notices of the Royal Astronomical Society*, 474, 917
- Montes, M. & Trujillo, I. 2019, *Monthly Notices of the Royal Astronomical Society*, 482, 2838
- Muñoz, R. P., Eigenthaler, P., Puzia, T. H., et al. 2015, *ApJ*, 813, L15
- Naiman, J. P., Pillepich, A., Springel, V., et al. 2018, *MNRAS*, 477, 1206
- Napolitano, N. R., Arnaboldi, M., & Capaccioli, M. 2002, *Astronomy and Astrophysics*, 383, 791
- Napolitano, N. R., Gatto, M., Spiniello, C., et al. 2022, *A&A*, 657, A94
- Napolitano, N. R., Gatto, M., Spiniello, C., et al. 2021, arXiv e-prints, arXiv:2109.08695
- Napolitano, N. R., Pota, V., Romanowsky, A. J., et al. 2014, *Monthly Notices of the Royal Astronomical Society*, 439, 659
- Napolitano, N. R., Romanowsky, A. J., Capaccioli, M., et al. 2011, *Monthly Notices of the Royal Astronomical Society*, 411, 2035
- Napolitano, N. R., Romanowsky, A. J., Coccato, L., et al. 2009, *Monthly Notices of the Royal Astronomical Society*, 393, 329
- Napolitano, N. R., Romanowsky, A. J., & Tortora, C. 2010, *Monthly Notices of the Royal Astronomical Society*, no
- Navarro, J. F., Frenk, C. S., & White, S. D. M. 1996, *ApJ*, 462, 563
- Navarro, J. F., Frenk, C. S., & White, S. D. M. 1997, *ApJ*, 490, 493
- Nelson, D., Pillepich, A., Springel, V., et al. 2018, *MNRAS*, 475, 624
- Nelson, D., Sharma, P., Pillepich, A., et al. 2020, *Monthly Notices of the Royal Astronomical Society*, 498, 2391
- Nelson, D., Springel, V., Pillepich, A., et al. 2019, *Computational Astrophysics and Cosmology*, 6, 2
- Newman, A. B., Treu, T., Ellis, R. S., & Sand, D. J. 2013, *ApJ*, 765, 25
- Oemler, Augustus, J. 1974, *ApJ*, 194, 1
- Old, L., Wojtak, R., Pearce, F. R., et al. 2017, *Monthly Notices of the Royal Astronomical Society*, 475, 853
- Oser, L., Ostriker, J. P., Naab, T., Johansson, P. H., & Burkert, A. 2010, *ApJ*, 725, 2312
- Osipkov, L. P. 1979, *Soviet Astronomy Letters*, 5, 42
- Ostriker, J. P., Peebles, P. J. E., & Yahil, A. 1974, *The Astrophysical Journal*, 193, L1
- Ostrov, P., Geisler, D., & Forte, J. C. 1993, *AJ*, 105, 1762

- Paolillo, M., Fabbiano, G., Peres, G., & Kim, D. W. 2002, *ApJ*, 565, 883
- Peacock, J. A. 1983, *MNRAS*, 202, 615
- Pedregosa, F., Varoquaux, G., Gramfort, A., et al. 2012, arXiv e-prints, arXiv:1201.0490
- Pedregosa, F., Varoquaux, G., Gramfort, A., et al. 2011, *Journal of Machine Learning Research*, 12, 2825
- Peirani, S., Dubois, Y., Volonteri, M., et al. 2017, *MNRAS*, 472, 2153
- Peng, E. W., Ferguson, H. C., Goudfrooij, P., et al. 2011, *The Astrophysical Journal*, 730, 23
- Peng, E. W., Jordán, A., Côté, P., et al. 2006, *ApJ*, 639, 95
- Peng, E. W., Jordán, A., Côté, P., et al. 2008, *ApJ*, 681, 197
- Pillepich, A., Madau, P., & Mayer, L. 2015, *The Astrophysical Journal*, 799, 184
- Pillepich, A., Nelson, D., Springel, V., et al. 2019, *Monthly Notices of the Royal Astronomical Society*, 490, 3196
- Pillepich, A., Springel, V., Nelson, D., et al. 2018, *MNRAS*, 473, 4077
- Planck Collaboration, Ade, P. A. R., Aghanim, N., et al. 2014, *A&A*, 571, A16
- Planck Collaboration, Ade, P. A. R., Aghanim, N., et al. 2016, *Astronomy & Astrophysics*, 594, A13
- Poggianti, B. M., Moretti, A., Gullieuszik, M., et al. 2017, *ApJ*, 844, 48
- Popping, G., Pillepich, A., Somerville, R. S., et al. 2019, *The Astrophysical Journal*, 882, 137
- Pota, V., Napolitano, N. R., Hilker, M., et al. 2018, *MNRAS*, 481, 1744
- Pota, V., Romanowsky, A. J., Brodie, J. P., et al. 2015, *MNRAS*, 450, 3345
- Pratt, G. W., Arnaud, M., Biviano, A., et al. 2019, *Space Sci. Rev.*, 215, 25
- Press, W. H. & Schechter, P. 1974, *ApJ*, 187, 425
- Puzia, T. H., Paolillo, M., Goudfrooij, P., et al. 2014, *ApJ*, 786, 78
- Rahmati, A., Schaye, J., Bower, R. G., et al. 2015, *Monthly Notices of the Royal Astronomical Society*, 452, 2034, arXiv: 1503.05553
- Ramos-Almendares, F., Abadi, M., Muriel, H., & Coenda, V. 2018, *ApJ*, 853, 91
- Remus, R.-S. & Forbes, D. A. 2022, *ApJ*, 935, 37
- Richardson, T. & Fairbairn, M. 2013, *MNRAS*, 432, 3361
- Richtler, T., Dirsch, B., Gebhardt, K., et al. 2004, *AJ*, 127, 2094
- Richtler, T., Schuberth, Y., Hilker, M., et al. 2008, *A&A*, 478, L23
- Rubin, V. C., Ford, W. K., J., & Thonnard, N. 1978, *ApJ*, 225, L107
- Rubin, V. C., Ford, W. K., J., & Thonnard, N. 1980, *ApJ*, 238, 471
- Rubin, V. C. & Ford, Jr., W. K. 1970, *ApJ*, 159, 379

References

- Saglia, R. P., Kronawitter, A., Gerhard, O., & Bender, R. 2000, *AJ*, 119, 153
- Samurović, S. 2016, *Ap&SS*, 361, 199
- Sand, D. J., Treu, T., Ellis, R. S., Smith, G. P., & Kneib, J.-P. 2008, *ApJ*, 674, 711
- Sand, D. J., Treu, T., Smith, G. P., & Ellis, R. S. 2004, *ApJ*, 604, 88
- Sarzi, M., Iodice, E., Coccato, L., et al. 2018, *A&A*, 616, A121
- Schaller, M., Frenk, C. S., Bower, R. G., et al. 2015, *MNRAS*, 451, 1247
- Schaye, J., Crain, R. A., Bower, R. G., et al. 2015, *MNRAS*, 446, 521
- Schuberth, Y., Richtler, T., Bassino, L., & Hilker, M. 2008, *A&A*, 477, L9
- Schuberth, Y., Richtler, T., Hilker, M., et al. 2010, *A&A*, 513, A52
- Serra, P., de Blok, W. J. G., Bryan, G. L., et al. 2016, in *MeerKAT Science: On the Pathway to the SKA*, 8
- Serra, P., Koribalski, B., Duc, P.-A., et al. 2013a, *Monthly Notices of the Royal Astronomical Society*, 428, 370
- Serra, P., Koribalski, B., Popping, A., et al. 2013b, ATNF Proposal, C2894, aDS Bibcode: 2013atnf.prop.5810S
- Serra, P., Maccagni, F. M., Kleiner, D., et al. 2019, *Astronomy & Astrophysics*, 628, A122
- Serra, P., Oosterloo, T., Morganti, R., et al. 2012, *Monthly Notices of the Royal Astronomical Society*, 422, 1835
- Sérsic, J. L. 1963, *Boletín de la Asociación Argentina de Astronomía La Plata Argentina*, 6, 41
- Sheardown, A., Roediger, E., Su, Y., et al. 2018, *ApJ*, 865, 118
- Spiniello, C., Napolitano, N. R., Arnaboldi, M., et al. 2018, *MNRAS*, 477, 1880
- Springel, V. 2010, *Monthly Notices of the Royal Astronomical Society*, 401, 791
- Springel, V., Pakmor, R., Pillepich, A., et al. 2018, *MNRAS*, 475, 676
- Su, Y., Nulsen, P. E. J., Kraft, R. P., et al. 2017, *ApJ*, 851, 69
- Syer, D. & Tremaine, S. 1996, *MNRAS*, 281, 925
- Syer, D. & White, S. D. M. 1998, *MNRAS*, 293, 337
- Thomas, J., Saglia, R. P., Bender, R., et al. 2005, *MNRAS*, 360, 1355
- Tonini, C. 2013, *ApJ*, 762, 39
- Tonnesen, S., Bryan, G. L., & van Gorkom, J. H. 2007, *ApJ*, 671, 1434
- Tonry, J. L., Dressler, A., Blakeslee, J. P., et al. 2001, *The Astrophysical Journal*, 546, 681
- Tucker, E., Walker, M. G., Mateo, M., et al. 2020, *The Astrophysical Journal*, 888, 106
- Tumlinson, J., Peebles, M. S., & Werk, J. K. 2017, *Annual Review of Astronomy and Astrophysics*, 55, 389, arXiv:1709.09180 [astro-ph]
- van de Voort, F., Springel, V., Mandelker, N., van den Bosch, F. C., & Pakmor, R. 2019, *Monthly Notices of the Royal Astronomical Society: Letters*, 482, L85

- van Dokkum, P. G. & Conroy, C. 2010, *Nature*, 468, 940
- Vazdekis, A., Koleva, M., Ricciardelli, E., Röck, B., & Falcón-Barroso, J. 2016, *MNRAS*, 463, 3409
- Vazdekis, A., Sánchez-Blázquez, P., Falcón-Barroso, J., et al. 2010, *MNRAS*, 404, 1639
- Veljanoski, J. & Helmi, A. 2016, *A&A*, 592, A55
- Venhola, A., Peletier, R., Laurikainen, E., et al. 2020, *A&A*, 633, C2
- Vogelsberger, M., Genel, S., Springel, V., et al. 2014, *MNRAS*, 444, 1518
- Watkins, L. L., van de Ven, G., den Brok, M., & van den Bosch, R. C. E. 2013, *MNRAS*, 436, 2598
- West, M. J., Cote, P., Jones, C., Forman, W., & Marzke, R. O. 1995, *ApJ*, 453, L77
- White, Raymond E., I. 1987, *MNRAS*, 227, 185
- White, S. D. M. & Rees, M. J. 1978, *MNRAS*, 183, 341
- Williams, B. F., Ciardullo, R., Durrell, P. R., et al. 2007, *ApJ*, 654, 835
- Yahagi, H. & Bekki, K. 2005, *MNRAS*, 364, L86
- Young, L. M., Scott, N., Serra, P., et al. 2014, *Monthly Notices of the Royal Astronomical Society*, 444, 3408
- Yun, K., Pillepich, A., Zinger, E., et al. 2019, *MNRAS*, 483, 1042
- Zahedy, F. S., Chen, H.-W., Johnson, S. D., et al. 2019, *Monthly Notices of the Royal Astronomical Society*, 484, 2257
- Zeldovich, Y. B. & Sunyaev, R. A. 1969, *Ap&SS*, 4, 301
- Zhu, G., Ménard, B., Bizyaev, D., et al. 2014, *Monthly Notices of the Royal Astronomical Society*, 439, 3139
- Zhu, L., Romanowsky, A. J., van de Ven, G., et al. 2016a, *MNRAS*, 462, 4001
- Zhu, L., van de Ven, G., Watkins, L. L., & Posti, L. 2016b, *MNRAS*, 463, 1117
- Zwicky, F. 1933, *Helvetica Physica Acta*, 6, 110

Acknowledgements

To this end of my PhD journey, I have countless people to whom I would like to express my gratitude for their encouragement and guidance.

My deepest gratitude first goes to my advisor Michael Hilker who expertly guided me throughout. Your generosity helped me to make my time at ESO more discoverable as you allowed me to develop my collaboration and project ideas; the finest example is the Flatiron project. Thanks for your valuable suggestions, encouragement and inspiring thoughts. With your support, I achieved many things during my PhD life that helped me develop myself as a researcher. I was fortunate enough to have you as my supervisor.

Thanks also go to ESO and its scientific community. I will forever cherish my time at ESO, science life at ESO helped me develop as a better person and researcher. Nelma, thank you for your help and support organizing my travel trips. Many thanks to Giacomo for your regular concern and support during my postdoc applications.

I would also like to thank Glenn for his ideas, support, and suggestions during my PhD time. Mariya, your help and guidance is much appreciated. I value the help of my LMU supervisor Prof. Dr Andreas Burkert, for reviewing my thesis progress and igniting new thoughts and ideas.

My appreciation also extends to Stephanie Tonnessen and Greg Bryan, who gave me an excellent opportunity to carry out the project at CCA, Flatiron. It was a great privilege to be a part of this project, where I explored something new during my PhD. Many thanks to Gergo Popping, who helped me several times. I would also like to thank people who directly or indirectly contributed to my research. Thanks to Eric Emsellem, Harald Kuntschner, and Marina Rejkuba for your positive opinion and guidance.

Anna Pala, my ESO fellow mentor, acted like a local guardian to me who stood out throughout every stage of my PhD, thanks a bunch for your help. Thank you to Marianne for your constant interest, advice, and invaluable suggestions during my PhD journey. I value the support which Katja Fahrion has extended to me. Thanks for all the proofreading hours you gave for my thesis. Without you, it would be tough to imagine my postdoc applications. You are just amazing and super helpful. Many thanks to Sabine for providing input and suggesting me in developing my science projects. Thanks to Tadeja for sharing the scripts and fixing my code bugs.

I want to convey my sincere gratitude to Dr Alka Misra. Your encouragement, support and guidance helped me to pursue my research dreams. I shall be forever indebted for your

References

help and advice.

Thank goes to my friends here and overseas for the kind of help they have extended to me. Thank you, Roland, Aishwarya, Jianhang, Dominika, Francesco, Pierrick, Pierre and Abhijeet, who helped me to make my time at ESO enjoyable and memorable. I also extend my appreciation to Shreyas, Paramanand, Madhuri, Saurabh, and Ashish for all your motivation and trust in me.

Thanks to my family for the endless support and love. I am incredibly grateful to my mother for her love, prayers and sacrifices she made for me. I am obliged to my sister and brother for their constant support and love. A special note of thanks to Apu, my partner, for her unfailing support and continuous encouragement. Thank you for always being there with me. I am blessed to have you in my life.

A heartfelt gratitude to all.